Basic Approaches to the Simulation of Recrystallization and Grain Growth

D. Raabe
Max-Planck-Institut
für Eisenforschung
Germany

A. D. Rollett
Carnegie Mellon University
USA

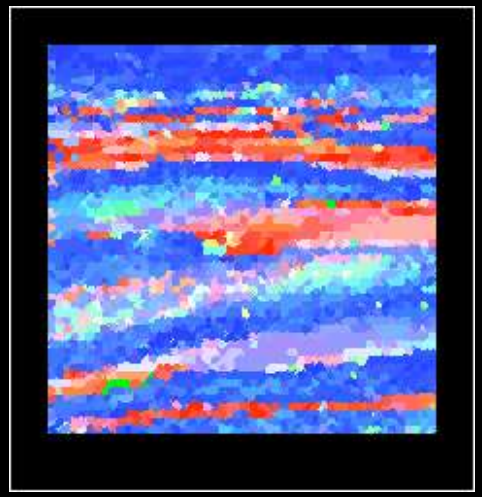

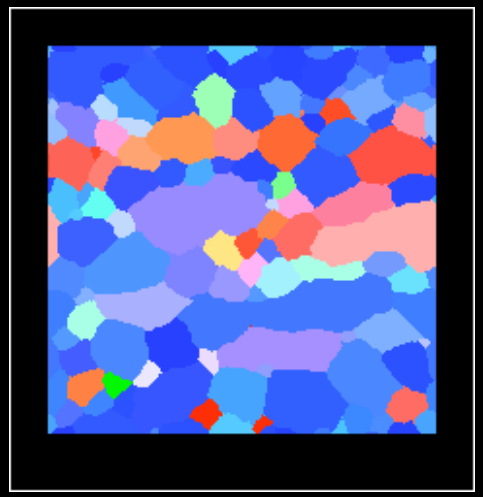

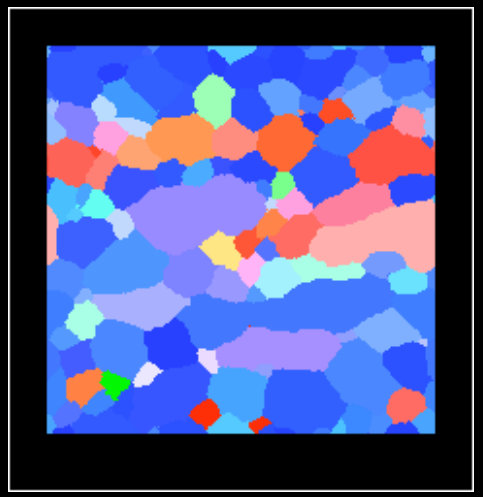

Outline *)

- **Simulations: why ? how?**
- **Discrete simulation methods**
- **Examples**
- **Conclusions**

*) *soft magnetic steels*

Outline

- **Simulations: why ? how?**
- **Discrete simulation methods**
- **Examples**
- **Conclusions**

Simulations: why ?

- Understanding (prerequisite to optimization)
- Models available
- (Some) material data available

- Investment ratio: experiments/computers: factor 100

  (Cost reduction via computational materials design)

Simulations: how ? (continuum / atomic)

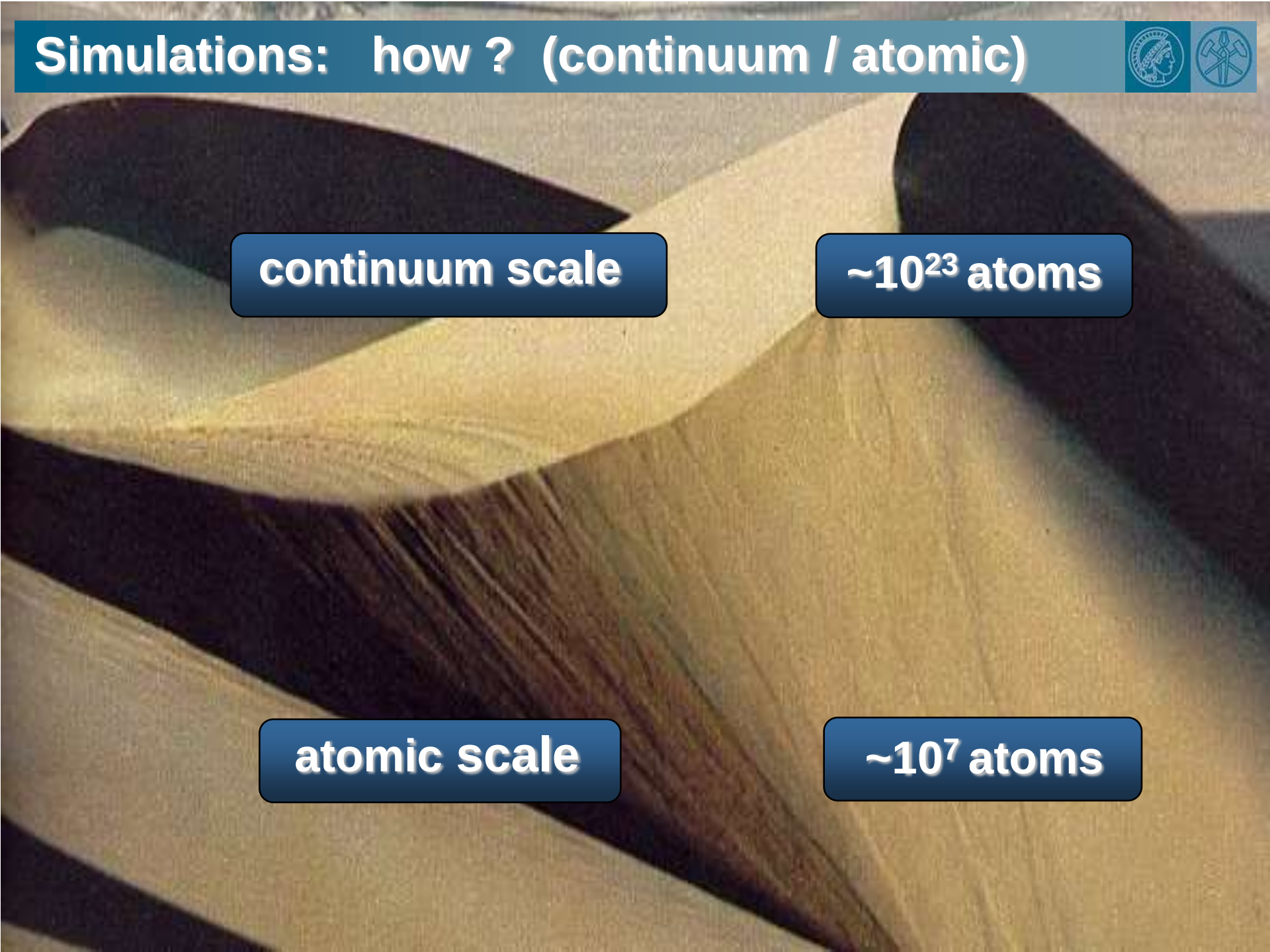

Simulations: how ? (global conditions)

some steps are not well defined

Simulations: how ? (local conditions)

color code: total v. Mises strain

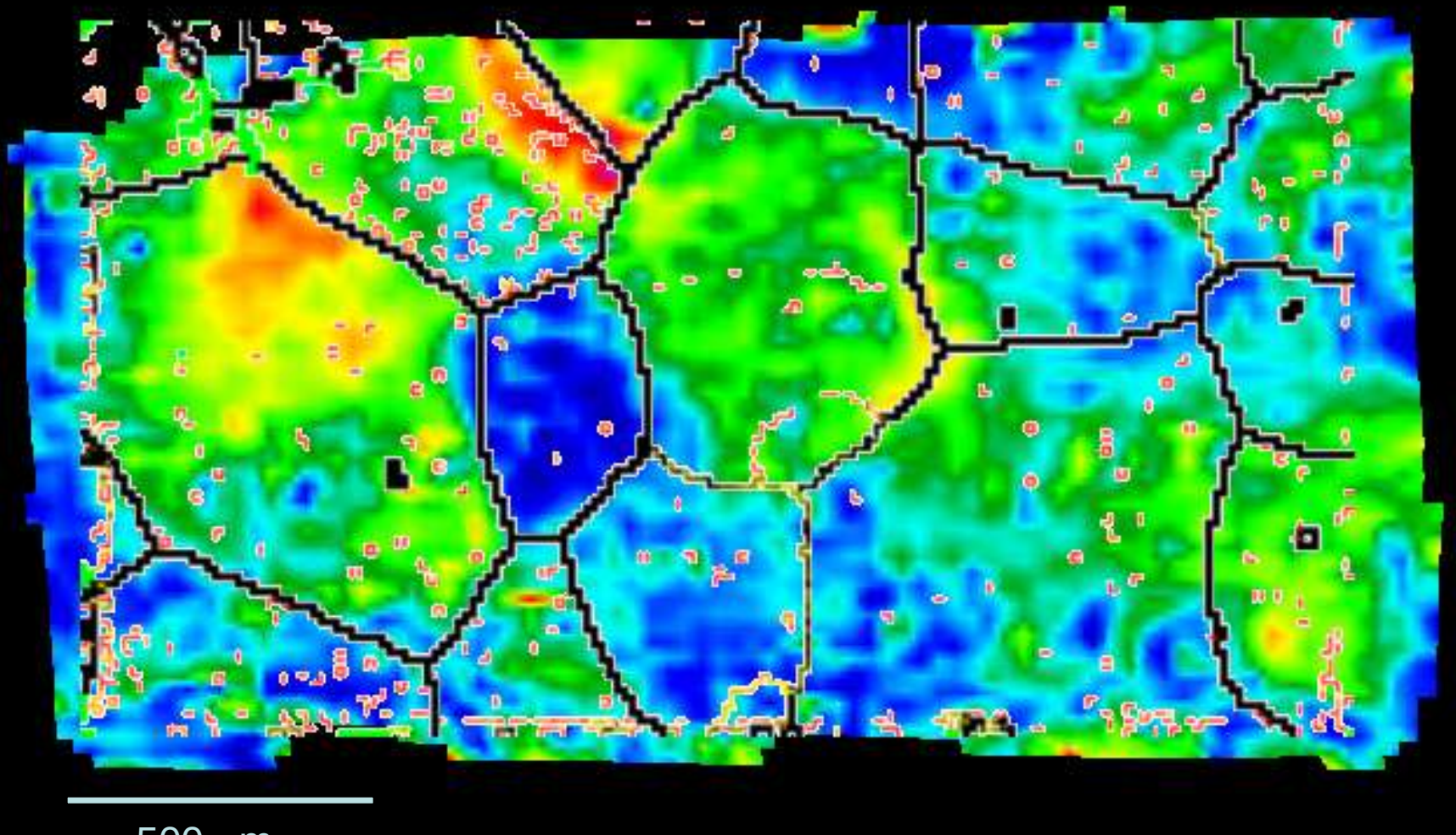

Simulations: how ? (inheritance)

materials have a history

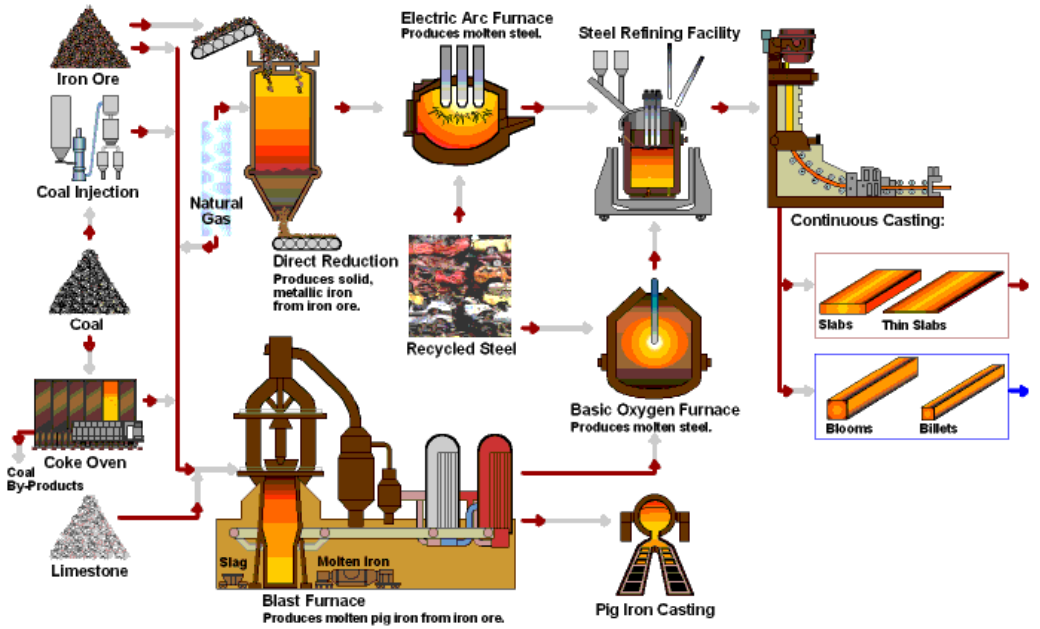

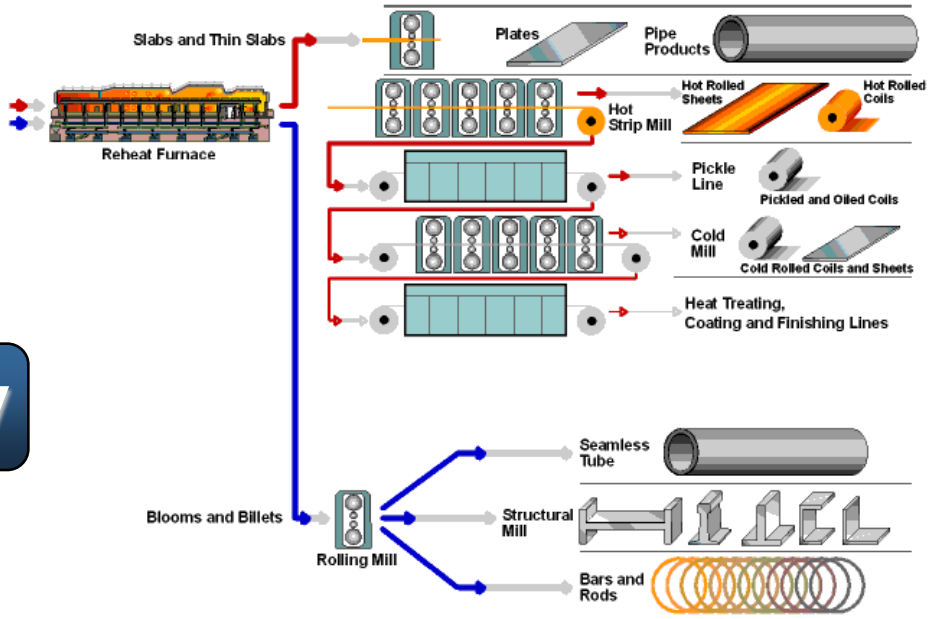

Neuronal simulation methods

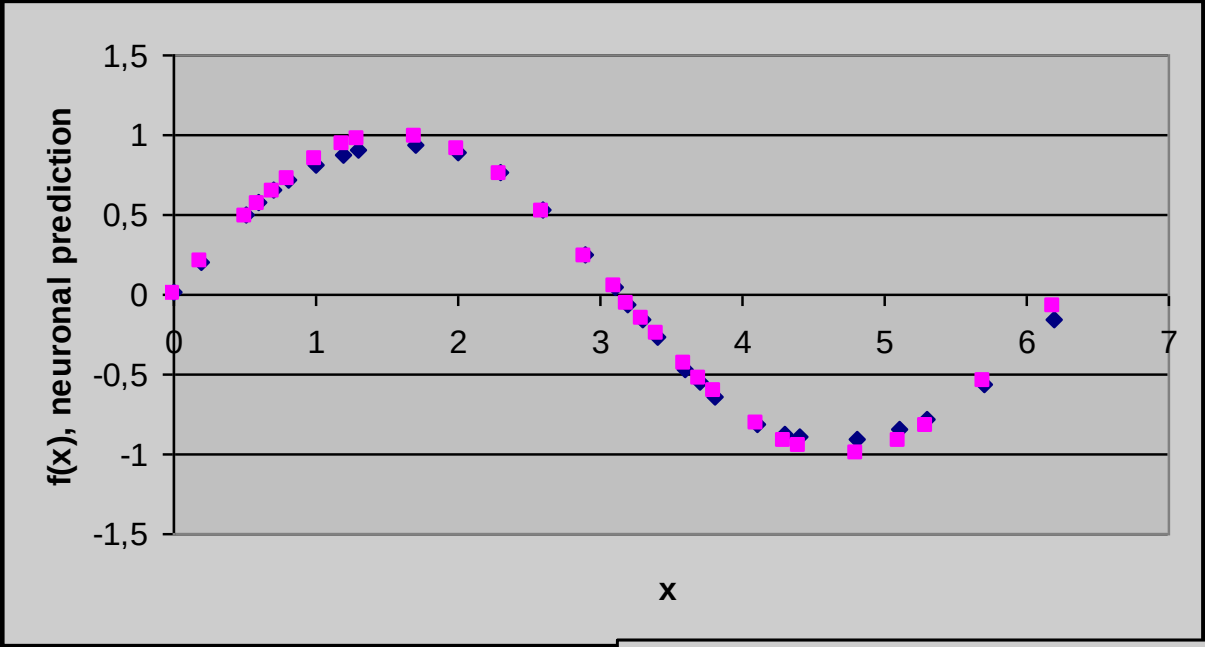

Training up to 2π

data fit: OK

Application beyond 2π

prediction: not OK

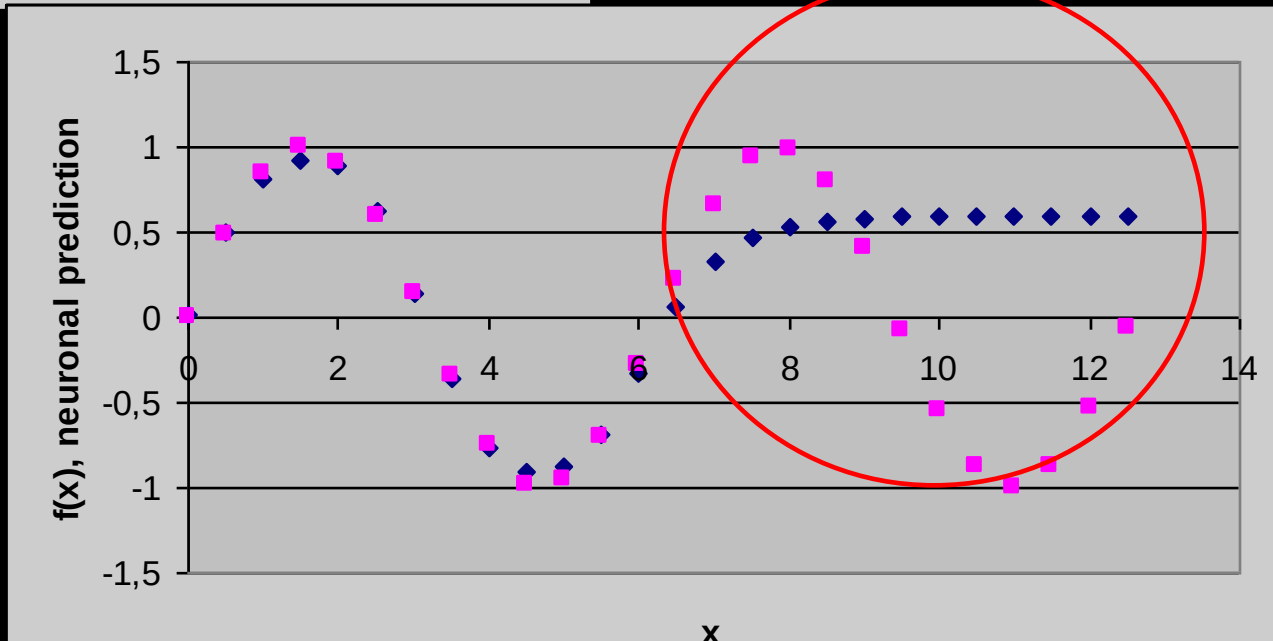

Simulations: how ? (mechanisms)

large data sets

($10^4 \cdot 10^3$)

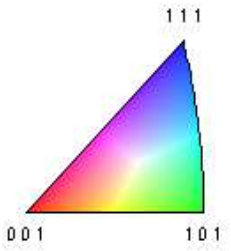

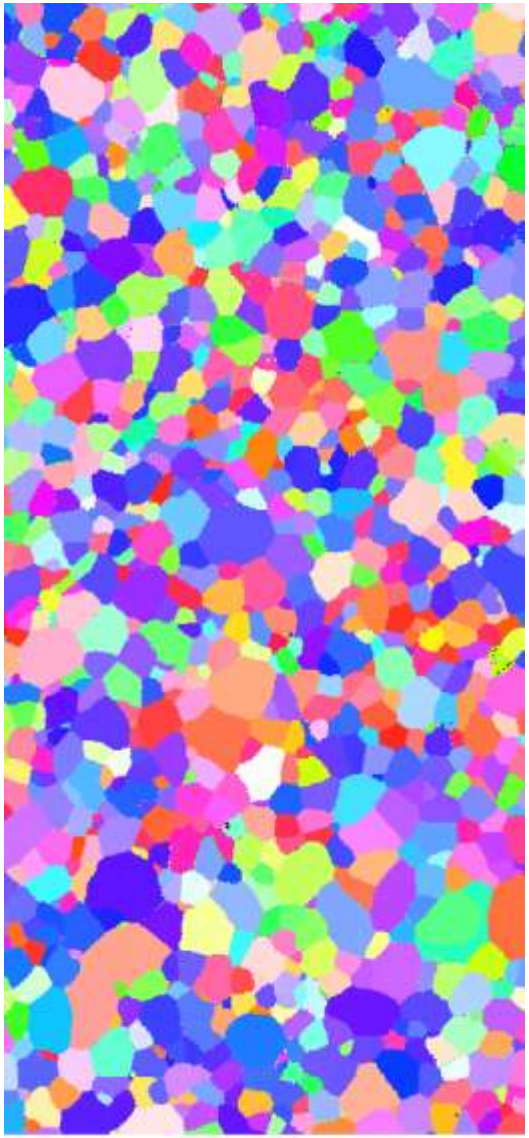

70.00 µm = 70 steps

Simulations: how ? (summary)

- Continuum scale
- Large data sets
- Complex boundary conditions
- Integrated modeling (microstructure inheritance)
- Input data available?
- Quantitative?

Outline

- Simulations: why ? how?
- Discrete simulation methods
- Examples
- Conclusions

Discrete simulation methods

Potts

- o Monte Carlo (probabilistic), local thermodynamics, kinetics of transients
- \+ simple codes (available), flexible, data input simple
- \- no real kinetics, lattice based

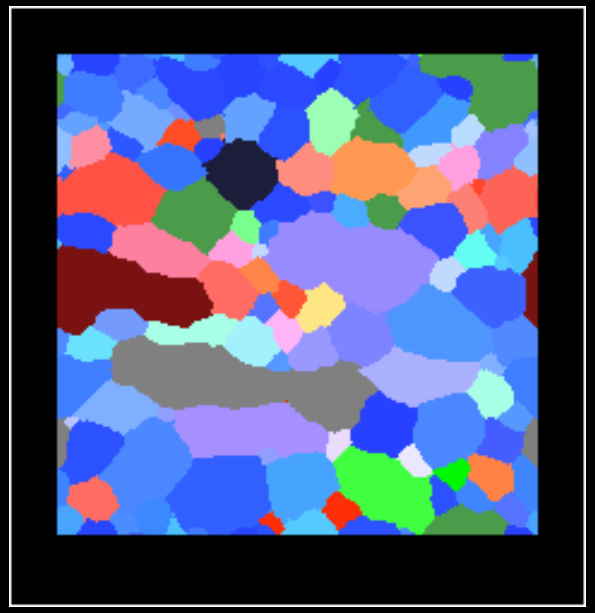

N. Chen (Max-Planck-Institut für Eisenforschung)

Discrete simulation methods

D. Raabe (Max-Planck-Institut für Eisenforschung)

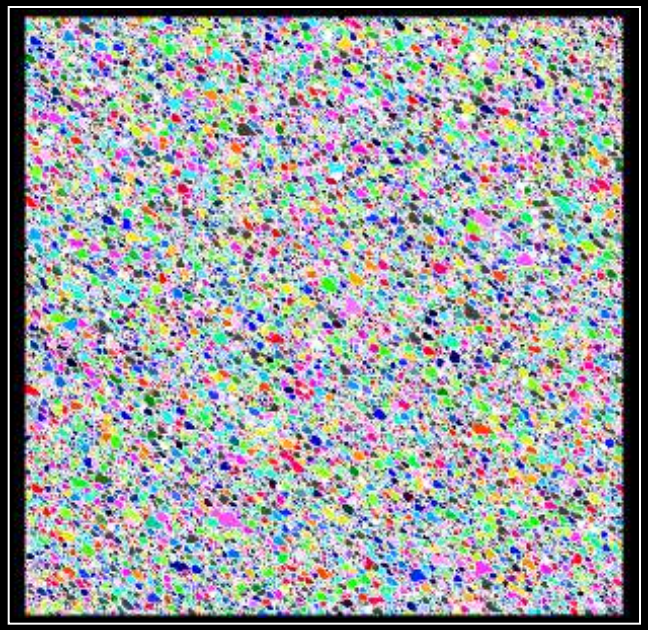

Cellular automata

- o deterministic, synchronous update
- \+ simple codes (available), flexible, real kinetics, data input simple
- \- lattice based

Discrete simulation methods

Vertex models

- o front tracking, deterministic, synchronous update
- \+ not lattice based, codes available, real kinetics
- \- difficult code (3D), no grain interiors

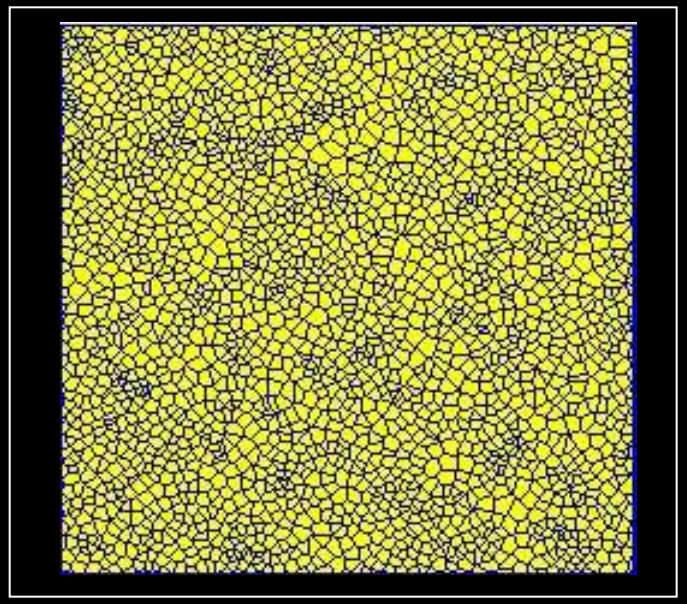

Navy Laboratories

Discrete simulation methods

Phase field

- o deterministic, synchronous update
- \+ includes diffusion, 2nd phase
- \- difficult codes (available), slow

S. Saito (Waseda University)

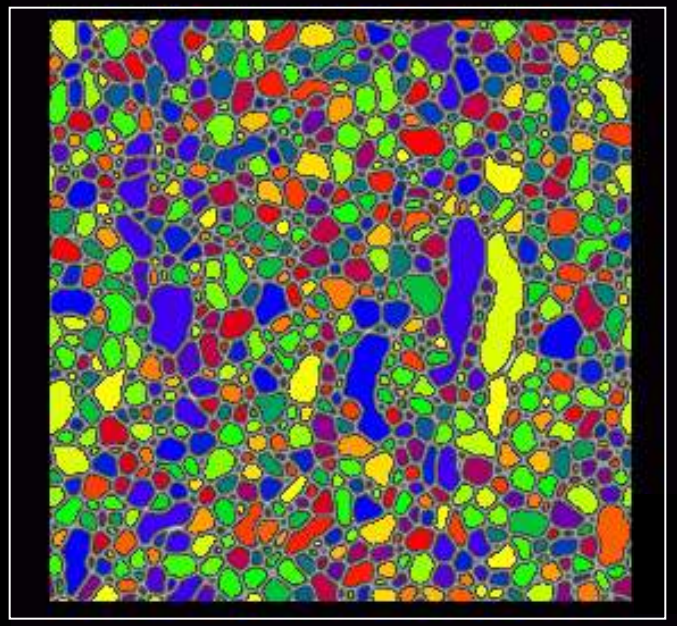

Discrete simulation methods

Dislocation dynamics

- o deterministic, synchronous update
- \+ dynamics of small angle boundaries
- \- difficult codes (3D), slow, small scale

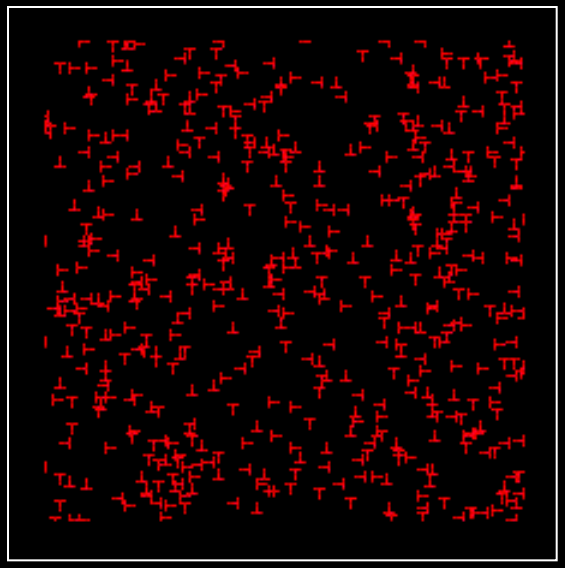

F. Roters (Max-Planck-Institut für Eisenforschung)

Discrete simulation methods

Finite Element Method

- o deterministic, synchronous update
- \+ robust
- \- difficult codes, slow, integration point based

T. Gammel (Los Alamos)

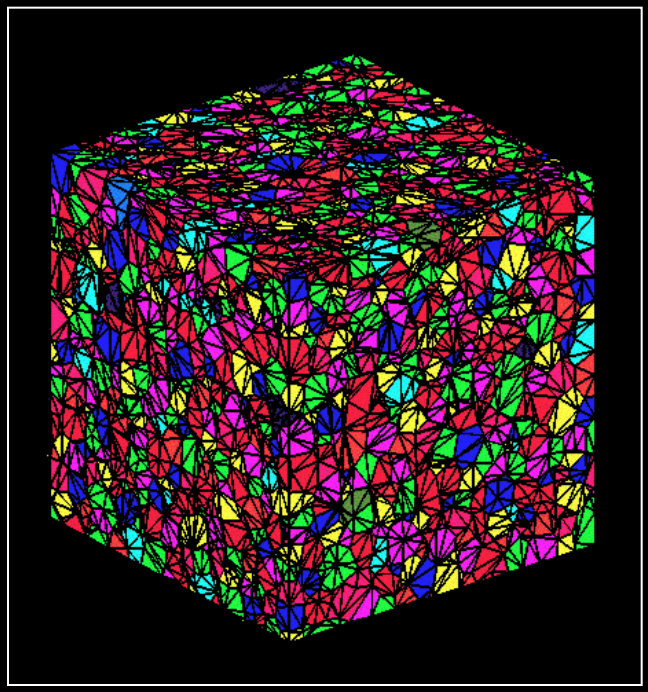

Outline

- Simulations: why ? how?
- Discrete simulation methods
- Examples
- Conclusions

Example #1: FEM + CA

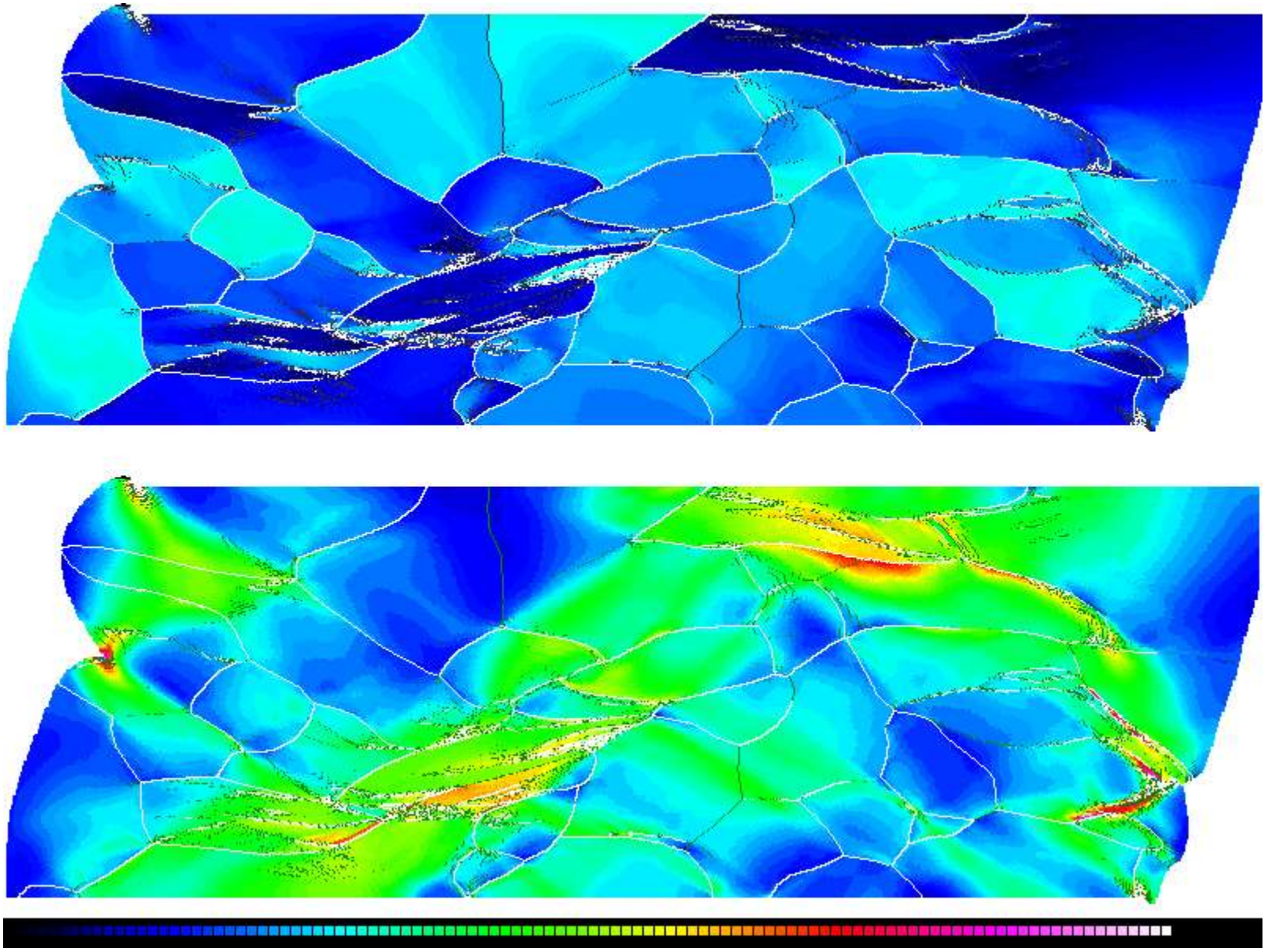

Example #2: EBSD + Potts - start data

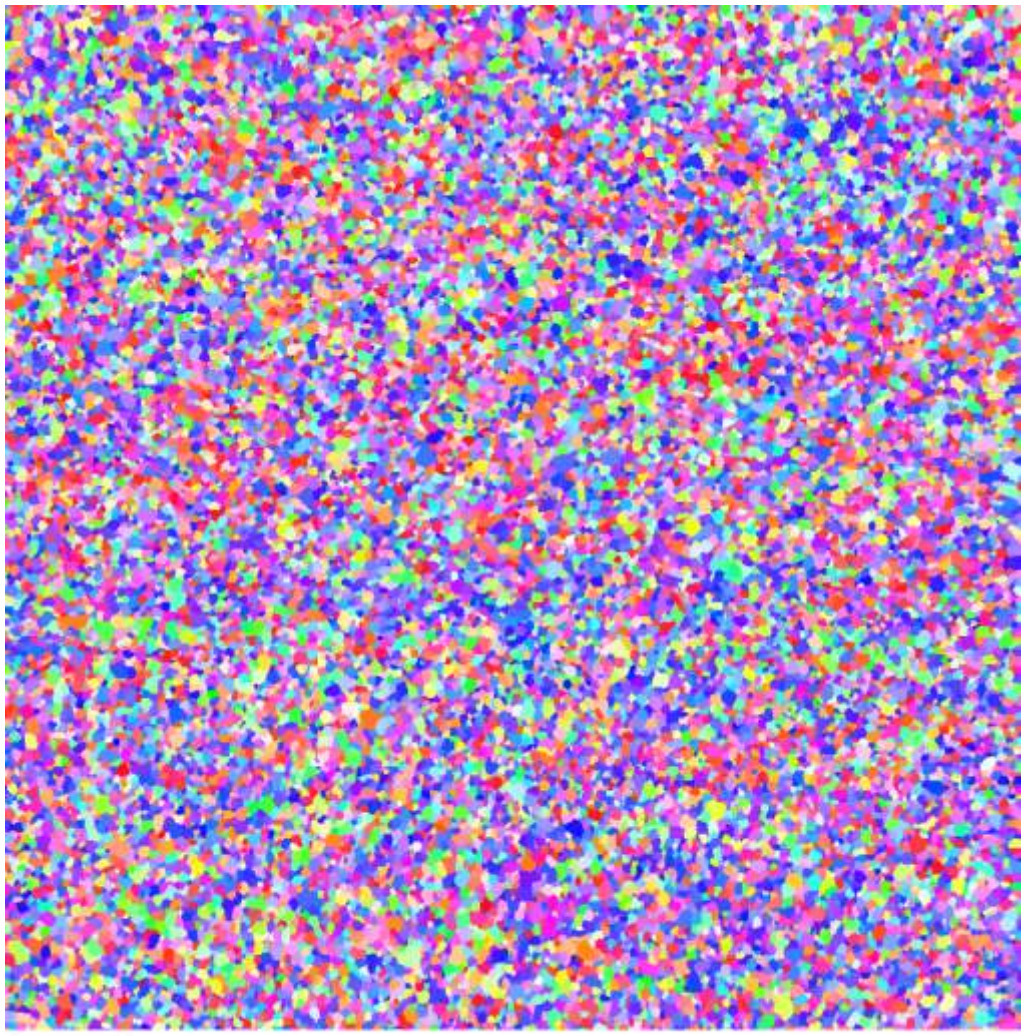

200.0 µm = 100 steps IPF [001]

experimental map (after RX)

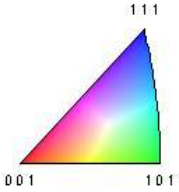

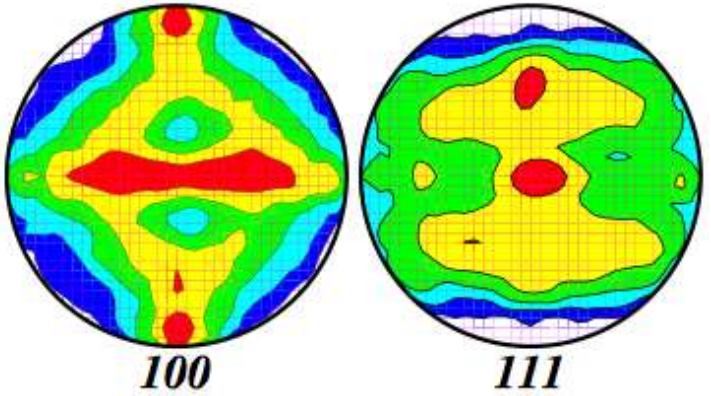

experimental

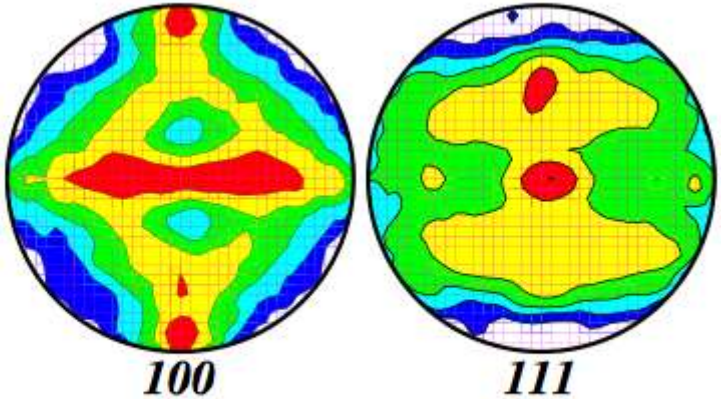

result of texture fit

Example #2: EBSD + Potts - basics

System Energy :

$$E = \frac{1}{2}\sum_{j}^{N}\sum_{i}^{n}\gamma(S_i, S_j)\left(1-\delta_{S_i S_j}\right)$$

Reorientation Probability :

$$P = \begin{cases} \dfrac{\gamma(S_i, S_j)}{J_{\max.}}\dfrac{M(S_i, S_j)}{M_{\max.}} \times 1 & \Delta E \le 0 \\ \dfrac{\gamma(S_i, S_j)}{J_{\max.}}\dfrac{M(S_i, S_j)}{M_{\max.}} \times \exp\left(\dfrac{-\Delta E}{JT}\right) & \Delta E > 0 \end{cases}$$

Example #2: EBSD + Potts - parameters

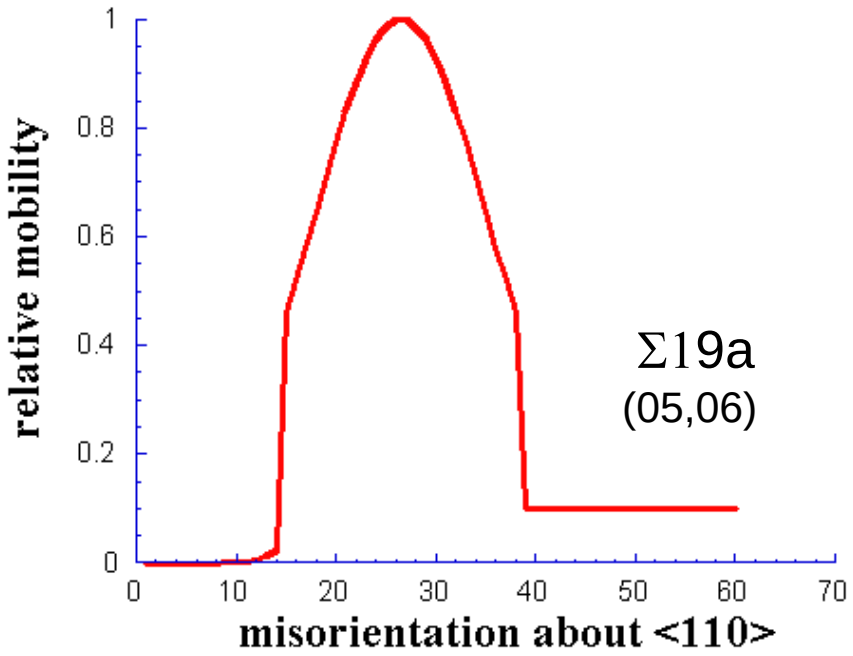

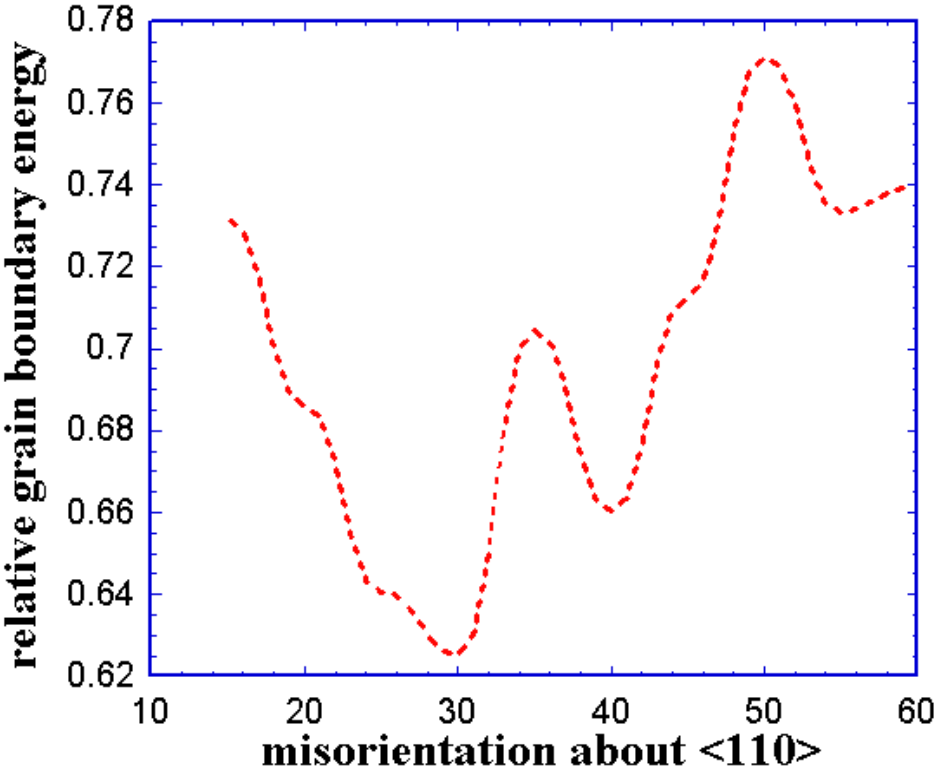

06,07

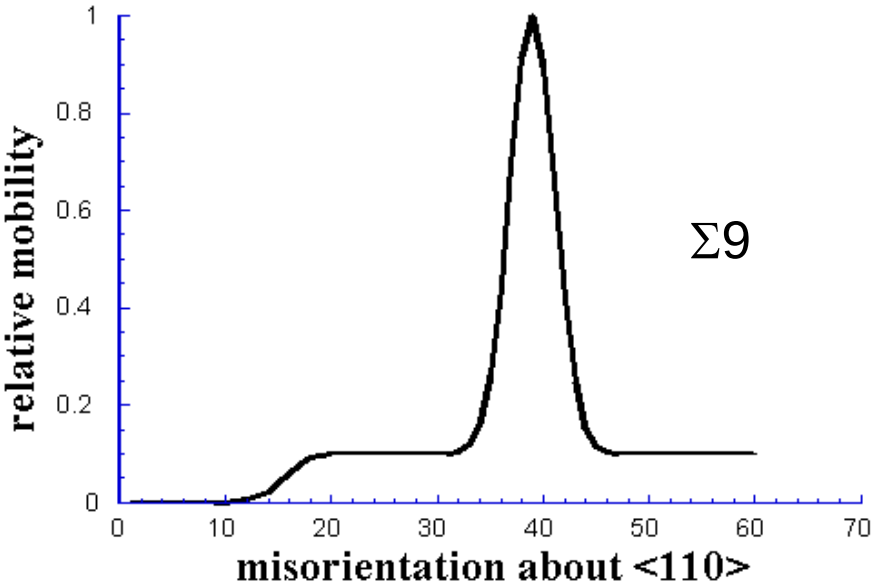

07

Example #2: EBSD + Potts - results grains

	10^7 MCS	10^8 MCS	10^9 MCS
Broad mobility peak at 27°<110>	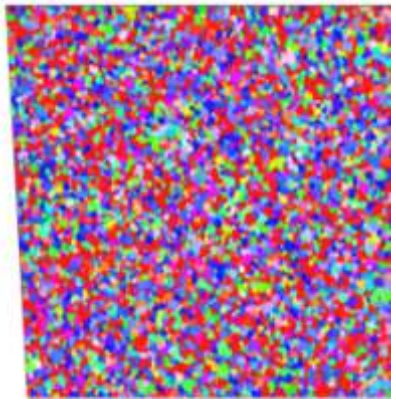	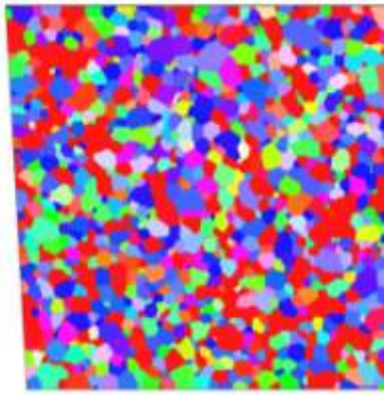	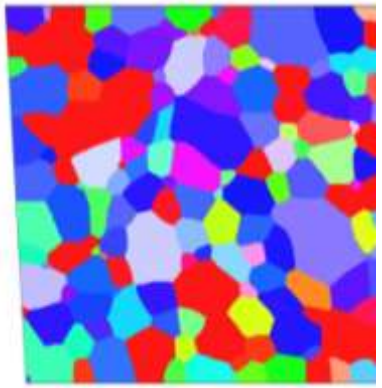
27°<110> with energy anisotropy	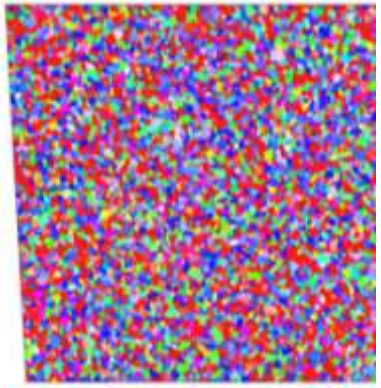	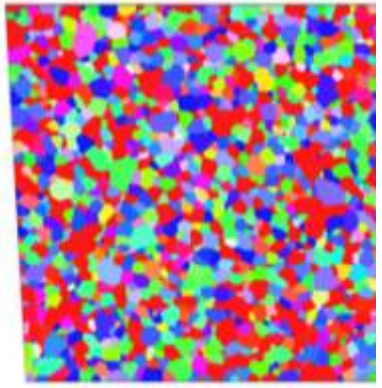	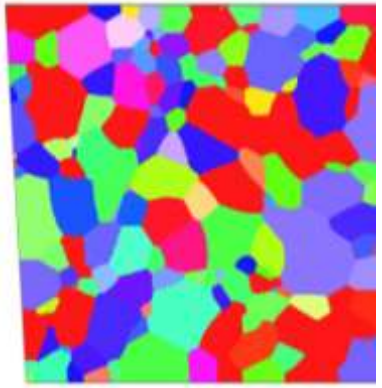
Sharp Σ9 mobility peak, with energy anisotropy	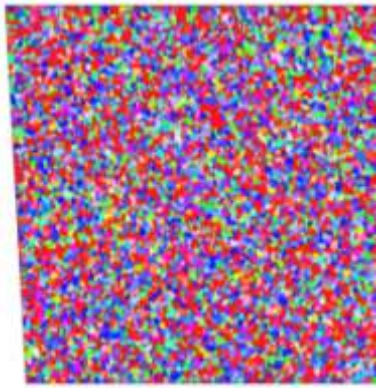	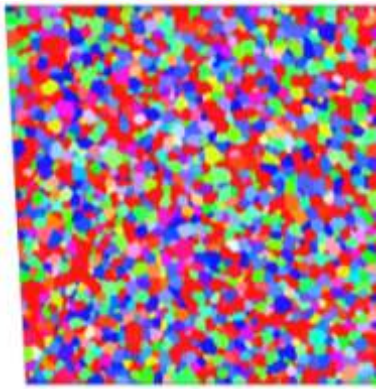	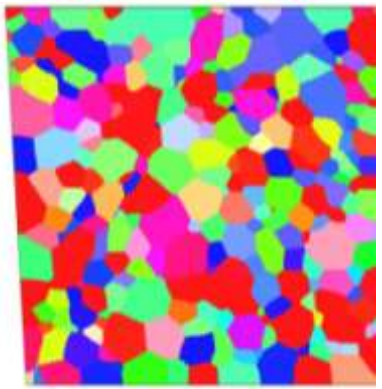

Example #2: EBSD + Potts - results texture

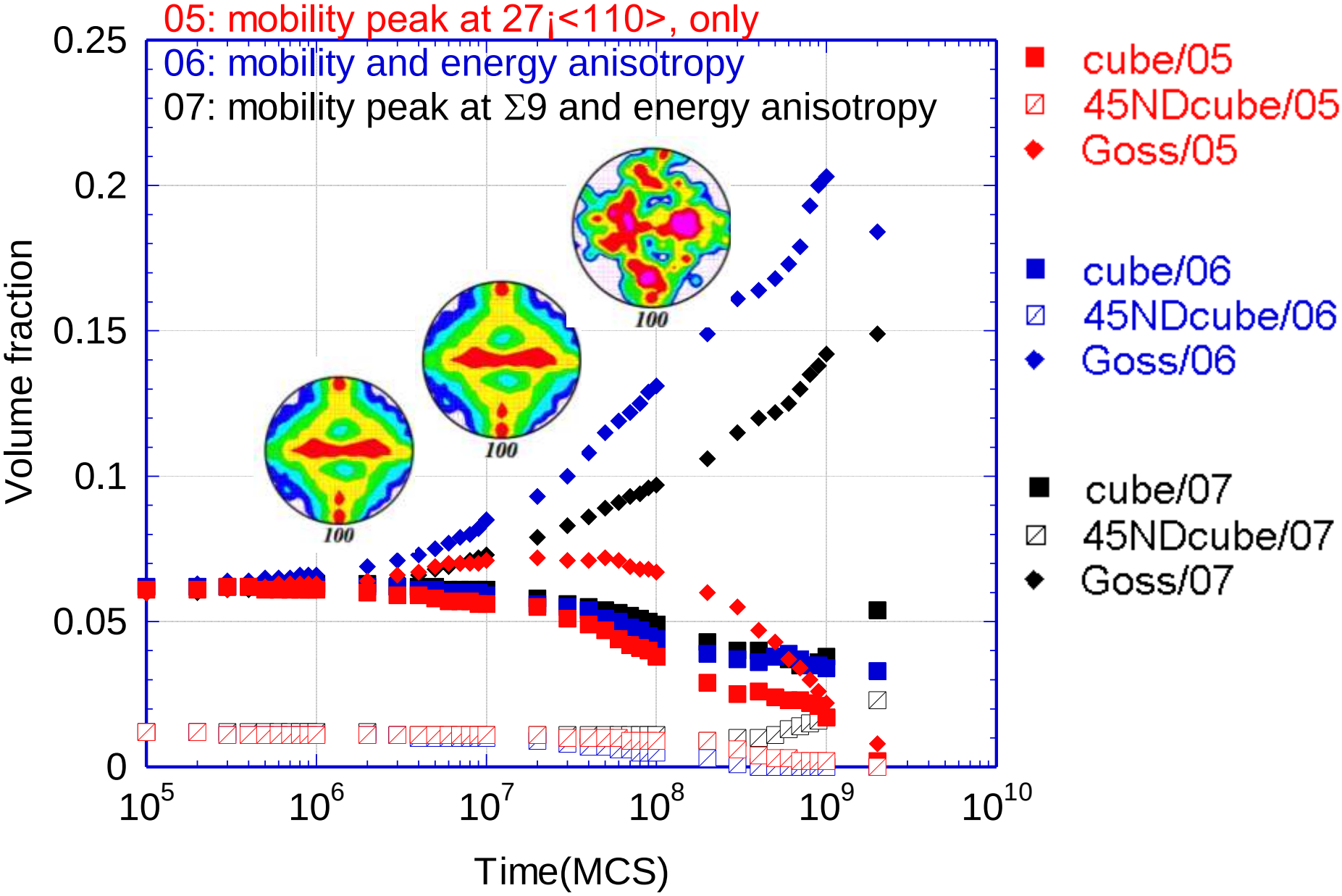

Outline

- Simulations: why ? how?
- Discrete simulation methods
- Examples
- Conclusions

Conclusions

Simulation methods (general thoughts)

- Potts / CA: robust, flexible, 3D, codes available
- Vertex: pure front tracking, difficult for 3D
- phase field: 2nd phase, impurities, 3D

Examples

- Potts: Goss growths for mobility+energy effect
  what about particles ?
  not abnormal
- CA+FEM: example for integrated modeling

Some References

PERGAMON

Acta mater. 48 (2000) 1617–1628

Acta MATERIALIA

www.elsevier.com/locate/actamat

SCALING MONTE CARLO KINETICS OF THE POTTS MODEL USING RATE THEORY

D. RAABE

Max-Planck-Institut für Eisenforschung, Max-Planck-Straße 1, 40237 Düsseldorf, Germany

(Received 16 March 1999; accepted 7 November 1999)

Abstract—A method is introduced for scaling Monte Carlo kinetics of the Potts model using rate theory. The method is particularly designed for the kinetic and spatial scaling of multistate kinetic Potts models using one or more sets of non-conserved structural or orientational state variables S_i each of which can assume a number of Q_i degenerate ground states (Q or multistate Potts models) as commonly employed for simulating recrystallization and curvature driven grain growth phenomena. The approach is based on the equivalence of single-site state switches in the Potts model and grain boundary motion as described by Turnbull's classical rate theory mapped on a simulation lattice. According to this approach the switching probabilities can be scaled by the ratio of the local and the maximum occurring values of the grain boundary mobility and by the ratio of the local and the maximum occurring values of configurational and scalar contributions to the driving force. The real time step elapsing during one Monte Carlo time step is scaled by the maximum occurring grain boundary mobility, the maximum occurring driving force, and the lattice parameter of the simulation grid.

Keywords: Computer simulation; Microstructure; Recrystallization & recovery; Grain growth; Theory & modeling

1. INTRODUCTION

Computer simulations which use time and space as independent variables are useful tools for investigating recrystallization and grain growth phenomena.

Applying them to spatially homogeneous starting microstructures allows one to examine analytical approaches and complement them with respect to topological aspects. Applying them to spatially non-homogeneous starting microstructures allows one to identify critical conditions and mechanisms that entail kinetic and topological deviations from analytical predictions. The latter aspect is of particular importance because non-homogeneous microstructures are the rule and not the exception in real materials.

Monte Carlo simulations based on the multistate kinetic Potts model have dominated the field of discrete recrystallization and grain growth predictions since their first introduction into physical metallurgy 15 years ago. Applications were devoted to normal grain growth [1–8], nucleation and static primary recrystallization [5–13], dynamic recrystallization [14, 15], abnormal grain growth [6–8, 16, 17], and growth processes under the influence of particle pinning [18–20].

The success of the Potts model can be attributed to its enormous flexibility, its computational simplicity, and the comparably short calculation times. An important shortcoming of the Potts model is the absence of intrinsic microstructural scaling measures.

The introduction of spatial and kinetic scaling into the Potts model offers two major advantages. First, it allows one to quantify space and time. This aspect is of relevance when aiming at the simulation of industrial processes, i.e. at the use of realistic boundary conditions. Second, the quantitative incorporation of a wide spectrum of realistic or experimental microstructure data, such as stored energy or grain boundary mobility and energy data, can only be realized on the basis of a *common* time and space scale. For instance, the presence of grain boundaries with different mobility but identical driving force should lead to different switching rates in the Potts model without spoiling the overall time scale of the simulation. This aspect is of relevance since experimental grain boundary mobility and energy data are increasingly available [21–24].

The introduction of scaling into mesoscale Monte Carlo simulations requires the combination of the underlying Potts lattice model with some adequate physical model of the situation to be investigated.

1359-6454/00/$20.00
PII: S1359-6454(99)00451-6

This paper suggests a method to scale Monte Carlo kinetics of the Potts model using rate theory. The scaling method is based on the equivalence of single-site state switches in the Potts model and grain boundary motion as described by classical rate theory mapped on a simulation lattice. The method is particularly designed for Potts models using a non-conserved structural state variable S (e.g. crystal orientation) which can assume a discrete number of Q degenerate ground states (Q or multistate Potts model). The method enables one to scale the switching probabilities by the ratio of the local and the maximum occurring values of the grain boundary mobility and by the ratio of the local and the maximum occurring values of configurational and scalar contributions to the driving force. The real time step elapsing during one Monte Carlo time step is scaled by the maximum occurring grain boundary mobility, the maximum occurring driving force, and the lattice parameter of the simulation lattice.

The plan of the paper is as follows. Section 2 is devoted to classical Monte Carlo kinetics of the multistate Potts model, reviewing in particular the energy operator, the Monte Carlo algorithm, classical Monte Carlo kinetics, and previous scaling approaches. Section 3 deals with classical rate theory of grain boundary motion. These two ingredients are used in Section 4 to derive the scaling method by formulating the equivalence of switches in the Potts model and grain boundary motion as quantified by rate theory.

2. MONTE CARLO KINETICS OF THE MULTISTATE POTTS MODEL

2.1. The energy operator

The Hamiltonian commonly used in Potts models [25] for simulating recrystallization and curvature driven grain growth typically quantifies the interfacial energy between dissimilar neighbor sites and the stored elastic energy [6–8, 11]

$$E = E_{gg} + E_{el} = \sum_{i=1}^{N}\left\{\frac{J}{2}\sum_{j=1}^{nnn}(1-\delta_{S_iS_j}) + H_{el}f(Q_u - S_i)\right\} \quad (1)$$

where E_{gg} is the energy proportional to the total grain boundary energy in the system, E_{el} the energy proportional to the total elastic energy due to stored dislocations in the system, N the number of lattice sites, nnn the geometrically weighted number of neighbor sites in the first, second, and third neighbor shell, S the orientational state variable, $\delta_{S_iS_j}$ the Kronecker symbol which assumes a value of one if $S_i = S_j$ and a value of zero if $S_i \neq S_j$, J an energy proportional to the grain boundary energy, and H_{el} an energy proportional to the stored elastic energy. J and H_{el} are positive. Their respective proportionality factors relating them to realistic energies scale the simulation with respect to thermal fluctuations. The ratio between the two proportionality factors determines the balance between curvature driven grain growth and recrystallization [11]. The function $f(Q_u - S_i)$ describes whether a site is recrystallized or not. Further details about the operator are given in Ref. [11].

The use of a spectrum of orientational states, each representing a discrete crystallographic orientation, allows one to map domains as regions of identical state, i.e. as crystal grains or subgrains. Equation (1) distinguishes configurational contributions to the energy, which are calculated as a sum over the immediate neighborhood nnn, from scalar contributions to the energy. This difference in the calculation of the system energy is of importance for the equivalence scaling procedure discussed later in this article.

2.2. Monte Carlo algorithm

The basic setup of a Monte Carlo model for simulating recrystallization and curvature driven grain coarsening consists of a spatial grid where the state of each lattice point is described in terms of a value of the orientational state variable (generalized spin) and a value of the scalar energy stored with this point (e.g. elastic energy due to stored dislocations). The configurational energy change is calculated during a trial flip of the orientational state variable by summing overall bonds between dissimilar neighbor points before and after the switch.

After mapping some initial configuration of these two state variables on a discrete spatial grid the Monte Carlo algorithm works according to the following rules. In the first step, a lattice coordinate is selected at random. In the second step, the values of the two state variables at this site are switched. In the third step, the total change in system energy associated with this switch is calculated applying equation (1) before and after the flip. In the fourth step, the probability that the chosen spin will switch is calculated using the Glauber transition function [26] or the Metropolis transition function [27]. The heat-bath method suggested by Glauber dynamics uses

$$W_{Gl} = \left(1 + \exp\left\{-\frac{\Delta E}{k_B T}\right\}\right)^{-1} \quad (2)$$

with $\Delta E = E_n - E_o$, where E_n is the new total energy of the spin configuration after the trial switch, E_o the old total energy of the current spin configuration before the trial switch, W_{Gl} the Glauber switching probability, k_B the Boltzmann constant, and T the absolute temperature (Fig. 1). The Metropolis method (Fig. 2) uses a switching probability W_M according to

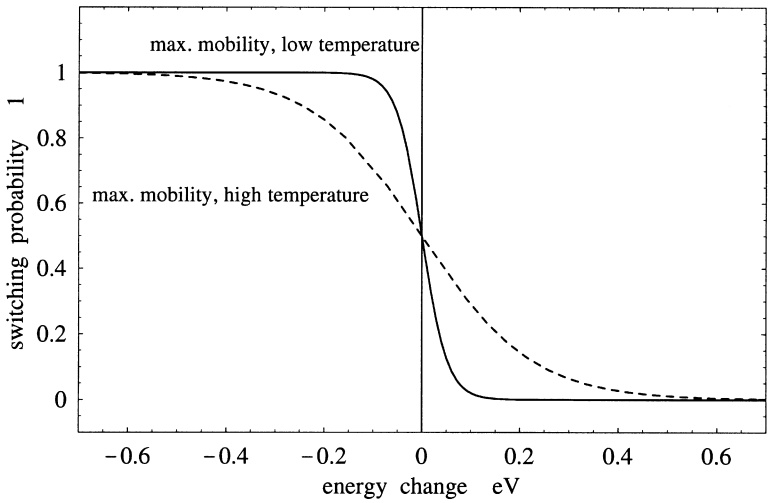

Fig. 1. Single-site Glauber transition function. The dashed line indicates high temperature and the solid line low temperature, equation (2).

$$W_{\mathrm{M}} = \begin{cases} \exp\left\{ -\dfrac{\Delta E}{k_{\mathrm{B}} T} \right\} & \text{if } \Delta E > 0 \\ 1 & \text{if } \Delta E \leq 0 \end{cases} \tag{3}$$

where $\Delta E = E_{\mathrm{n}} - E_{\mathrm{o}}$. In the fifth step, a random number ξ is generated in the interval $0 \leq \xi < 1$. In the sixth step, the switching decision is made, i.e. the flip is accepted if ξ is equal or below the calculated Glauber or Metropolis switching probability. Otherwise the switch is rejected and the initial spin configuration remains unchanged. Further details about the Monte Carlo rules are given in the papers cited in Section 1.

2.3. Classical Monte Carlo kinetics

Monte Carlo kinetics are commonly quantified by defining N trial flips, where N is the number of lattice sites, as one Monte Carlo step, i.e.

$$\Delta t_{\mathrm{MC}} = \frac{n}{N} \tag{4}$$

where Δt_{MC} is the Monte Carlo time step and n the number of trial switches. It is worth noting that this measure does not have the unit of time [s] but the unit of Monte Carlo steps [MCS].

At low temperatures, high degeneracy (high number of discrete possible states Q), and large average grain sizes (measured in units of lattice points), the probability of successfully switching an arbitrary site to a new orientation is very small and the Metropolis method becomes ineffective. For this reason Sahni *et al.* [28] and later Hassold and Holm [29] modified the continuous time method intro-

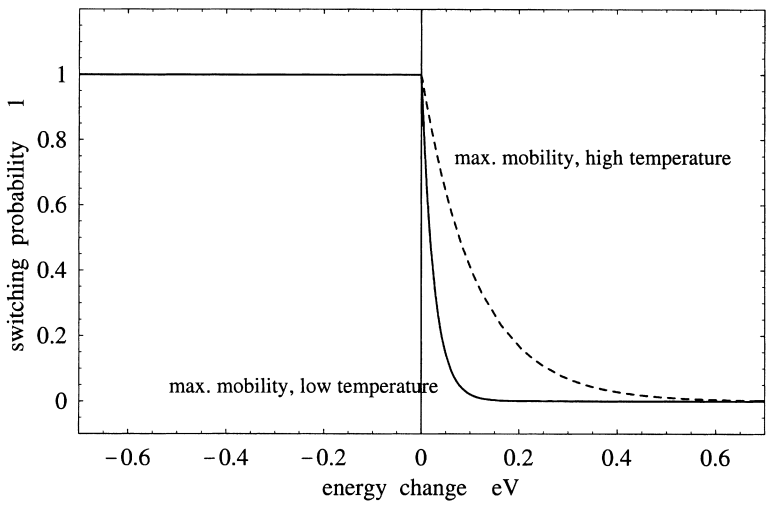

Fig. 2. Single-site Metropolis transition function. The dashed line indicates high temperature and the solid line low temperature, equation (3).

duced earlier for the Ising model [30] for the Potts model

$$\Delta t_{\mathrm{MC}}^{\mathrm{C}} = -\frac{(Q-1)\tau}{A}\ln(R) \tag{5}$$

where $\Delta t_{\mathrm{MC}}^{\mathrm{C}}$ is the Monte Carlo time step in the continuous time approach, Q the maximum number of discrete orientational states (spins), τ the average time between succeeding attempted state flips on the same lattice point (τ is usually regarded as the elementary Monte Carlo time unit), R a random number between zero and one, and A the total system activity which is defined by

$$A = \sum_{i=1}^{N}\Pi_i = \sum_{j=1}^{Q}\sum_{i=1}^{N}\pi_{ij} \tag{6}$$

where Π_i is the activity of lattice site i, and π_{ij} the probability of successfully flipping lattice site i to a new orientation S_j.

Further progress along this line was recently made by Mehnert and Klimanek [31] who derived a state-normalized version of the continuous time simulation method which allows one to reformulate Monte Carlo kinetics with a weaker dependence on the total number of possible orientational states

$$\Delta \hat{t}_{\mathrm{MC}}^{\mathrm{C}} = \frac{\Delta t_{\mathrm{MC}}^{\mathrm{C}}}{(Q-1)} = -\frac{\tau}{A}\ln(R) \tag{7}$$

where $\Delta \hat{t}_{\mathrm{MC}}^{\mathrm{C}}$ is the state-normalized Monte Carlo time step in the continuous time approach.

2.4. Previous scaling approaches

The major question in this paper is whether and how the above Monte Carlo time units [MCS] can be related to the real time [s]. In this context Safran *et al.* [32] suggested for atomic scale simulations to set the time scale by multiplying the transition probability with a basic attempt frequency $\Gamma = \tau_{\mathrm{a}}^{-1}$. The authors assumed this attack frequency to have an Arrhenius-type temperature dependence†, i.e.

$$\Gamma = \frac{1}{\tau_{\mathrm{a}}} = \exp\left\{-\frac{Q_{\mathrm{a}}}{k_{\mathrm{B}}T}\right\} \tag{8}$$

where Q_{a} is the activation energy associated with a single atomic jump event coupling the simulation to temperature. The Glauber transition probability according to Safran *et al.* then amounts to

$$W_{\mathrm{Gl}}^{\mathrm{S}} = \Gamma\left(1+\exp\left\{-\frac{\Delta E}{k_{\mathrm{B}}T}\right\}\right)^{-1}. \tag{9}$$

† Note that the original paper contains a misprint on p. 2695 concerning the sign of the argument of the exponential.

The Metropolis transition probability according to Safran *et al.* is

$$W_{\mathrm{M}}^{\mathrm{S}} = \begin{cases} \Gamma\exp\left\{-\dfrac{\Delta E}{k_{\mathrm{B}}T}\right\} & \text{if } \Delta E > 0 \\ \Gamma & \text{if } \Delta E \leq 0. \end{cases} \tag{10}$$

Concerning mesoscale simulations of recrystallization and curvature driven grain coarsening Anderson *et al.* [1] and Srolovitz *et al.* [2] pointed out that the boundary velocity determined by tracking successive spin flips in the Potts model yields kinetics that are formally equivalent to the classical rate theory of boundary motion. Following the suggestion of Safran *et al.* [32], equation (8), the authors state that the conversion of Monte Carlo steps to real time has an implicit activation energy factor, $\exp\{-W_{\mathrm{a}}/(k_{\mathrm{B}}T)\}$, which corresponds to the atomic jump frequency.

Mehnert and Klimanek [31] recently suggested in their paper on the state-normalization of the continuous time method that a conversion of Monte Carlo time steps to real time should be feasible using

$$\Delta \hat{t}_{\mathrm{MC}}^{\mathrm{C}} = \theta\,\Delta t\,\nu_{\mathrm{D}}\exp\left\{-\frac{W_{\mathrm{gb}}}{k_{\mathrm{B}}T}\right\} \tag{11}$$

where $\Delta \hat{t}_{\mathrm{MC}}^{\mathrm{C}}$ is the state-normalized Monte Carlo time step, Δt the real time step, ν_{D} the Debye frequency, θ a factor which correlates the physical to the model length scale, and W_{gb} the energy of activation for atom jumps from one grain surface through the boundary to the surface of the neighboring grain. This energy is usually termed the activation energy of grain boundary mobility.

Equations (5) and (7), discussed in the previous section, can also be regarded as scaling approaches. Though not generating a real time scale they introduce different Monte Carlo time weighting for sites with different switching probability. This means that a flip of a site with a small switching probability contributes a large portion to the Monte Carlo time step and vice versa.

A qualitative step forward in differentiating between switches associated with different mobilities of the grain boundaries involved was made by Holm *et al.* [33] [equation (8) in their paper]. For considering the influence of grain boundary mobility on the switching probability Holm *et al.* used a rule of the form

$$W_{\mathrm{M}}^{\mathrm{H}} = \begin{cases} 0 & \text{if } \Delta E > 0 \\ m & \text{if } \Delta E \leq 0 \end{cases} \tag{12}$$

where m is the mobility assigned to the switched site. It is important to note that this method introduces a relative switching rate of different sites provided different mobilities were assigned to them, rendering m into m_i. In their paper Holm *et al.* used

different spatial mobility functions in order to simulate microstructures with gradients in the resulting grain shape and size. A similar scaling method based on mobility was earlier used by Rollett *et al.* for the simulation of abnormal grain growth [17] [equation (4) in their paper].

3. PHENOMENOLOGICAL RATE THEORY OF GRAIN BOUNDARY MOTION

Turnbull formulated a phenomenological rate equation, which describes the motion of large angle grain boundaries in terms of isotropic single-atom diffusion processes perpendicular to a homogeneous planar grain boundary segment under the influence of free energy gradients

$$\dot{\mathbf{x}} = \mathbf{n}\nu_{\mathrm{D}}\lambda_{\mathrm{gb}}c\left(\exp\left\{-\frac{\Delta G-\Delta G_{\mathrm{t}}/2}{k_{\mathrm{B}}T}\right\} - \exp\left\{-\frac{\Delta G+\Delta G_{\mathrm{t}}/2}{k_{\mathrm{B}}T}\right\}\right) \tag{13}$$

where $\dot{\mathbf{x}}$ is the interface velocity, ν_{D} the Debye frequency, λ_{gb} the jump width through the interface, c the intrinsic concentration of in-plane self-diffusion carrier defects (e.g. grain boundary vacancies or shuffle sources), $\mathbf{n}$ the normal to the grain boundary segment, ΔG the Gibbs enthalpy of motion through the interface, ΔG_{t} the Gibbs enthalpy associated with the transformation, k_{B} the Boltzmann constant, and T the absolute temperature [34].

Bold symbols indicate vector quantities. The Debye frequency is of the order of 10^{13}–10^{14}/s and the jump width of the order of the magnitude of the Burgers vector.

Replacing the Gibbs enthalpy of motion by the corresponding enthalpy and entropy, expressing the concentration of the in-plane defects in terms of their thermal density, and expressing the Gibbs enthalpy associated with the transformation by the driving force and the activation volume leads to

$$\dot{\mathbf{x}} = \mathbf{n}\nu_{\mathrm{D}}\lambda_{\mathrm{gb}}\exp\left\{\frac{\Delta S_{\mathrm{f}}}{k_{\mathrm{B}}}\right\}\exp\left\{-\frac{\Delta H_{\mathrm{f}}}{k_{\mathrm{B}}T}\right\} \times\left(\exp\left\{-\frac{\Delta H_{\mathrm{m}}-T\Delta S_{\mathrm{m}}-(p\Omega/2)}{k_{\mathrm{B}}T}\right\} - \exp\left\{-\frac{\Delta H_{\mathrm{m}}-T\Delta S_{\mathrm{m}}+(p\Omega/2)}{k_{\mathrm{B}}T}\right\}\right) \tag{14}$$

where p is the negative change in Gibbs enthalpy per volume unit across the interface (driving force), Ω the atomic volume, ΔS_{f} the entropy of formation, ΔH_{f} the enthalpy of formation, ΔS_{m} the entropy of motion, and ΔH_{m} the enthalpy of motion. The atomic volume is of the order of b^3, where b is the magnitude of the Burgers vector.

While ΔS_{f} mainly quantifies the vibrational entropy, ΔS_{m} contains configurational and vibrational portions. Summarizing these terms leads to

$$\dot{\mathbf{x}} = \mathbf{n}\nu_{\mathrm{D}}b\exp\left\{\frac{\Delta S_{\mathrm{f}}+\Delta S_{\mathrm{m}}}{k_{\mathrm{B}}}\right\}\sinh\left(\frac{p\Omega}{k_{\mathrm{B}}T}\right) \times\exp\left\{-\frac{\Delta H_{\mathrm{f}}+\Delta H_{\mathrm{m}}}{k_{\mathrm{B}}T}\right\}. \tag{15}$$

Due to the small argument in the sinh, equation (15) can be linearized

$$\dot{\mathbf{x}} \approx \mathbf{n}\nu_{\mathrm{D}}b\exp\left\{\frac{\Delta S_{\mathrm{f}}+\Delta S_{\mathrm{m}}}{k_{\mathrm{B}}}\right\}\left(\frac{p\Omega}{k_{\mathrm{B}}T}\right) \times\exp\left\{-\frac{\Delta H_{\mathrm{f}}+\Delta H_{\mathrm{m}}}{k_{\mathrm{B}}T}\right\}. \tag{16}$$

This approximation reproduces the well-known phenomenological Turnbull expression

$$\dot{\mathbf{x}} = \mathbf{n}\,mp = \mathbf{n}\,m_0\ \times\exp\left\{-\frac{Q_{\mathrm{gb}}}{k_{\mathrm{B}}T}\right\}p \tag{17}$$

where m is the mobility, m_0 the pre-exponential factor, and Q_{gb} the activation energy of grain boundary mobility.

Comparing the coefficients in equations (16) and (17) yields

$$m_0 = \frac{\nu_{\mathrm{D}}b\Omega}{k_{\mathrm{B}}T}\exp\left\{\frac{\Delta S_{\mathrm{f}}+\Delta S_{\mathrm{m}}}{k_{\mathrm{B}}}\right\}$$

$$Q_{\mathrm{gb}} = \Delta H_{\mathrm{f}}+\Delta H_{\mathrm{m}}. \tag{18}$$

Equations (13)–(18) provide a phenomenological kinetic picture of grain boundary motion, where the atomic processes associated with a particular grain boundary are statistically described in terms of $m = m_0(\Delta\mathbf{g}, \mathbf{n})$ and $Q_{\mathrm{gb}} = Q_{\mathrm{gb}}(\Delta\mathbf{g}, \mathbf{n})$, where $\mathbf{g}$ is the rotation matrix quantifying the misorientation across the grain boundary and $\mathbf{n}$ the normal of the grain boundary segment.

Considering the misorientation and the boundary normal of each grain boundary segment occurring in a microstructure simulation is of importance because of the strong dependence of the grain boundary mobility on these parameters. Since it is difficult to quantify some of the physical parameters in equation (18), particularly with respect to their dependence on the misorientation, it is preferable to use experimental rather than theoretical mobility data wherever possible [21–24].

4. SCALING BY EQUIVALENCE

4.1. General formulation

The lattice site flips occurring in a Potts model based on a Hamiltonian of the type shown in equation (1) for curvature driven grain growth and recrystallization implicitly mimic the motion of

grain boundary segments. This means that the classical linearized symmetric rate theory for thermally activated grain boundary motion under the influence of free energy gradients as outlined above, equation (17), is an appropriate kinetic model for expressing the equivalence of spin flips in the Potts model and real grain boundary motion. Formally, the equivalence can be expressed by

$$\dot{\mathbf{x}}_{\mathrm{P}} = \dot{\mathbf{x}}_{\mathrm{rate}}$$

$$\mathbf{n}\frac{\lambda_{\mathrm{P}}}{\Delta t_{\mathrm{MC}}\Delta t_{\mathrm{real}}} = \mathbf{n}m(p_{\mathrm{c}} + p_{\mathrm{s}})$$

$$\frac{\lambda_{\mathrm{P}}}{\Delta t_{\mathrm{MC}}\Delta t_{\mathrm{real}}} = m_0 \exp\left\{-\frac{Q_{\mathrm{gb}}}{k_{\mathrm{B}}T}\right\}(p_{\mathrm{c}} + p_{\mathrm{s}}) \qquad (19)$$

where $\dot{\mathbf{x}}_{\mathrm{P}}$ is the boundary velocity in the Potts model, $\dot{\mathbf{x}}_{\mathrm{rate}}$ the boundary velocity according to rate theory as given by equation (17), $\mathbf{n}$ the normal of the grain boundary segment, p_{c} configurational contributions to the driving force (e.g. through boundary curvature), p_{s} scalar contributions to the driving force (e.g. through the elastic energy associated with stored dislocations or through an applied magnetic field), Δt_{MC} the kinetic Monte Carlo measure in units of [MCS] as given by equation (4), λ_{P} the jump width or lattice parameter of the Potts model in units of [m], and Δt_{real} the real time step in units of [s/MCS].

The separation of the configurational from the scalar contributions to the total driving force is necessary since the scaling introduced by equation (19) must be formulated for a single-site switching function of the type given by equation (2) or equation (3) rather than for a coupled set of differential equations of motion.

Reformulating equation (19) leads to an expression for the real time elapsing during a number of Δt_{MC} kinetic Monte Carlo time steps

$$\Delta t_{\mathrm{real}} = \frac{\lambda_{\mathrm{P}}}{\Delta t_{\mathrm{MC}} m p} = \frac{\lambda_{\mathrm{P}}}{\Delta t_{\mathrm{MC}} m_0 (p_{\mathrm{c}} + p_{\mathrm{s}})}\exp\left\{+\frac{Q_{\mathrm{gb}}}{k_{\mathrm{B}}T}\right\}. \qquad (20)$$

This equation shows that the real time step can only be expressed in units of [s/MCS]. For one single Monte Carlo time step ($\Delta t_{\mathrm{MC}} = 1$ MCS) the real time step amounts to

$$\Delta t_{\mathrm{real}} = \frac{\lambda_{\mathrm{P}}}{mp} \quad \left[\frac{\mathrm{s}}{\mathrm{MCS}}\right]. \qquad (21)$$

This simple preliminary result is physically plausible because it is obvious that a large prescribed lattice spacing λ_{P} requires a large time step to be swept by a moving grain boundary while a fast boundary needs a small time unit to sweep a given length λ_{P}. The inverse of this elementary time step can be regarded as an attack frequency $\Gamma_{\mathrm{real}} = 1/\Delta t_{\mathrm{real}}$ which is for a given lattice with parameter λ_{P} characteristic of a particular grain boundary.

Since the time scale introduced in equation (21) is thus dependent on the *local* grain boundary velocity at lattice point i, i.e.

$$\Delta t^{i}_{\mathrm{real}} = \frac{\lambda_{\mathrm{P}}}{m^i p^i} \quad \left[\frac{\mathrm{s}}{\mathrm{MCS}}\right] \qquad (22)$$

where $m = m^i$ is the local grain boundary mobility at lattice point i and $p = p^i$ the local driving force at lattice point i, equations (20) and (21) are only applicable to situations in which the driving force and the mobility are the same everywhere in the system. Such a restriction does only apply for a very limited number of highly idealized cases, for instance for primary static recrystallization in a perfect homogeneous single crystal with equal driving force (neglecting the influence of curvature) and equal grain boundary mobility throughout the entire specimen.

In a heterogeneous material, equation (21) would thus give a different characteristic time scale at different lattice points. Such a non-normalized scaling rule would be of no use. In order to adapt this scaling method to systems with a non-homogeneous distribution of driving force and mobility it is thus useful to normalize the system to a *common* time scale $\Delta t^{\min}_{\mathrm{real}}$.

Such a common time scale is identical to the minimum time scale occurring in the system. It is determined by the fastest moving grain boundary in the array. According to equation (17) the fastest possible grain boundary is characterized by maximum mobility $m^{\max}$ and maximum driving force $p^{\max}$, changing equation (21) into

$$\Delta t^{\min}_{\mathrm{real}} = \frac{\lambda_{\mathrm{P}}}{m^{\max}p^{\max}} = \frac{\lambda_{\mathrm{P}}}{m_0^{\max}(p_{\mathrm{c}}^{\max} + p_{\mathrm{s}}^{\max})} \times \exp\left\{\frac{Q^{\min}_{\mathrm{gb}}}{k_{\mathrm{B}}T}\right\} \quad \left[\frac{\mathrm{s}}{\mathrm{MCS}}\right] \qquad (23)$$

where $m_0^{\max}$ is the pre-exponential factor and $Q^{\min}_{\mathrm{gb}}$ the activation energy associated with the grain boundary with the highest mobility in the system. Δt_{MC} was here set to one Monte Carlo time step.

Before using this minimum occurring time step as a common time basis for *all* possible cell flips the corresponding single-site transition functions, equations (2) and (3), must be normalized in accord with this measure. This means that they must be scaled by the ratio of the local and the maximum occurring values of the grain boundary mobility and driving force. The Glauber transition function then changes to

$$\hat{W}_{\mathrm{Gl}} = \left(\frac{m^i}{m^{\max}}\right)\left(\frac{p_c^{\max}+p_s^i}{p_c^{\max}+p_s^{\max}}\right)\left(1+\exp\left\{\frac{\Delta E}{k_B T}\right\}\right)^{-1} \tag{24}$$

where ΔE is $E_n - E_o$, equation (2), $p_c^{\max}$ the maximum configurational driving force, $p_s^{\max}$ the maximum scalar (i.e. magnetic or elastic) driving force, and p_s^i the *local* scalar driving force at lattice point i.

It is important to note in equation (24) that the mobility ratio ($m^i/m^{\max}$) equally influences the forward and the backward motion of a grain boundary that may occur due to thermal fluctuation. This is plausible since for instance a twin boundary with a very small mobility can neither easily move according to the driving force nor fluctuate against it. In other words, the drag effect caused by low mobility principally acts in both directions. The effect of a mobility change according to equation (24) is shown in Fig. 3 for the Glauber function. Correspondingly, the Metropolis transition function changes to

$$\hat{W}_{\mathrm{M}} = \begin{cases} \left(\frac{m^i}{m^{\max}}\right)\left(\frac{p_c^{\max}+p_s^i}{p_c^{\max}+p_s^{\max}}\right)\exp\left\{-\frac{\Delta E}{k_B T}\right\} & \text{if } \Delta E > 0 \\ \left(\frac{m^i}{m^{\max}}\right)\left(\frac{p_c^{\max}+p_s^i}{p_c^{\max}+p_s^{\max}}\right) & \text{if } \Delta E \leq 0. \end{cases} \tag{25}$$

The effect of a mobility change according to equation (25) is shown in Fig. 4 for the Metropolis function.

Both scaled single-site transition functions predict a non-vanishing switching probability, $(m^i p_c^{\max})/(m^{\max}[p_c^{\max}+p_s^{\max}])$, for cases where the scalar driving forces are zero which is due to the ubiquitous presence of configurational driving forces.

Since the driving force term in equations (24) and (25) has the constant maximum configurational driving force and the local scalar driving force in the numerator and the constant maximum total (scalar and configurational) driving force in the denominator the maximum possible transition probability is exactly equal to one provided the local mobility is equal to the maximum mobility. The only situation where the transition probability at a lattice point is zero occurs when the local grain boundary mobility m^i is zero.

A comment must be made at this point about the relation between the energy change ΔE associated with each trial switch, equation (1), and the real driving forces that occur in the modified transition functions, equations (24) and (25). Energy changes given by the operator in equation (1) are not equivalent but only proportional to the negative driving forces (multiplied by the transformed volume unit). This means that the energy term ΔE in the transition functions serves exclusively to quantify the sensitivity of the system with respect to thermal fluctuations. The use of a Boltzmann-type penalty term for the evaluation of fluctuations can be regarded as a mathematical method to overcome

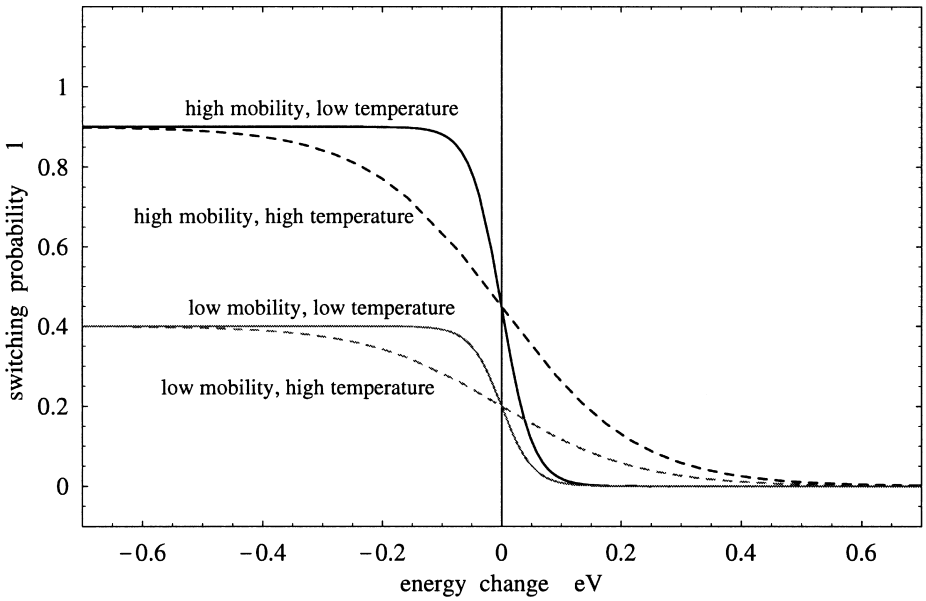

Fig. 3. Scaled single-site Glauber-type transition function for two different temperatures and grain boundary mobilities. The dashed lines indicate high temperature and the solid lines low temperature. The black lines indicate high mobility and the gray lines low mobility. The driving forces were constant, equation (24).

local energy minima that occur in Metropolis-type Monte Carlo simulations. True thermal fluctuations occur at an atomic scale. In the here suggested new concept they are already included in Turnbull's rate formulation of grain boundary motion, equation (13), which balances forward and backward jumps of the atoms through the boundary. This means that the true temperature dependence of recrystallization and grain growth dynamics lies in this framework in the temperature dependence of grain boundary motion which is fully accounted for by the activation energy of grain boundary mobility, equation (17).

Except for the use of thermal fluctuations, which are a typical feature of all Metropolis-type Monte Carlo methods, equations (19)–(25) reveal formal correspondence to the time scale and the transition functions derived for a probabilistic cellular automaton which is based on directly mapping rate theory on a simulation lattice [35].

4.2. Formulation for recrystallization and curvature driven grain growth

It is conceivable that various contributions $p^i_{j,\mathrm{s}}$ may add to the total local scalar driving force on a grain boundary at lattice point i, i.e. $p^i_{\mathrm{s}} = \sum_j p^i_{j,\mathrm{s}}$. When using such different scalar driving forces in the scaled Monte Carlo algorithm, qualitative differences between them must be considered. While magnetic driving forces can occur on either side of a fluctuating grain boundary, the use of a scalar driving force arising from elastic lattice distortions caused by stored dislocations ($p^i_{\mathrm{s}} = p^i_{\rho,\mathrm{s}}$) is not admissible for the quantification of thermal fluctuations since they may act *against* the sign of that force. The reason for this asymmetry is that it would violate the second law of thermodynamics if the stored internal energy would increase through the spontaneous accumulation of dislocations. In other words, stored dislocations are removed by a moving grain boundary but they cannot be formed by a fluctuating interface, i.e. by a trial flip. In contrast, magnetic energy terms must be considered both in the case of an energy increase and in the case of an energy decrease.

For simulations of recrystallization and curvature driven grain growth the Glauber switching function, therefore, is

$$\tilde{W}_{\mathrm{Gl}} = \begin{cases} \left(\dfrac{m^i}{m^{\max}}\right)\left(\dfrac{p_{\mathrm{c}}^{\max}}{p_{\mathrm{c}}^{\max}+p_{\mathrm{s}}^{\max}}\right)\left(1+\exp\left\{\dfrac{\Delta E}{k_{\mathrm{B}}T}\right\}\right)^{-1} \\ \qquad \text{if } \Delta E > 0 \\ \left(\dfrac{m^i}{m^{\max}}\right)\left(\dfrac{p_{\mathrm{c}}^{\max}+p^i_{\rho,\mathrm{s}}}{p_{\mathrm{c}}^{\max}+p_{\mathrm{s}}^{\max}}\right)\left(1+\exp\left\{\dfrac{\Delta E}{k_{\mathrm{B}}T}\right\}\right)^{-1} \\ \qquad \text{if } \Delta E \le 0. \end{cases} \tag{26}$$

The Metropolis transition function for this case is

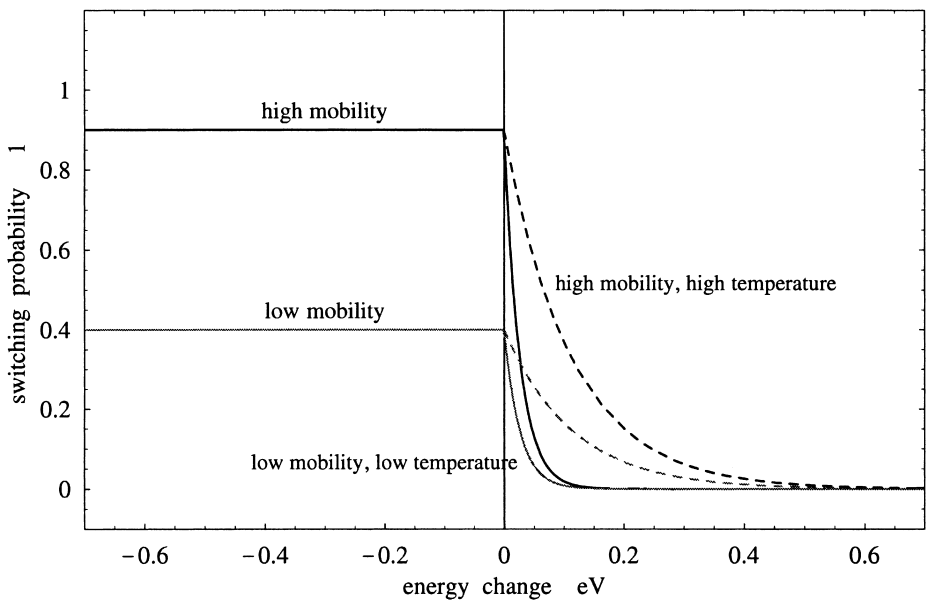

Fig. 4. Scaled single-site Metropolis-type transition function for two different temperatures and grain boundary mobilities. The dashed lines indicate high temperature and the solid lines low temperature. The black lines indicate high mobility and the gray lines low mobility. The driving forces were constant, equation (25).

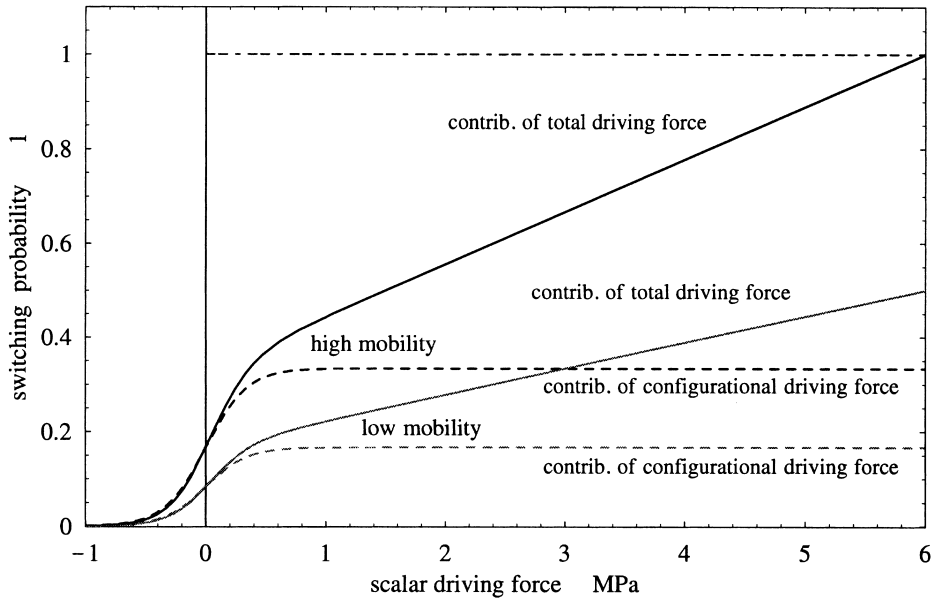

Fig. 5. Scaled single-site Glauber-type switching probability as a function of the scalar driving force for two different grain boundary mobilities. The dashed lines show the transition probability for configurational driving forces and the solid lines for the total driving force. The black lines indicate high mobility and the gray lines low mobility. The temperature was constant. The dashed line at $W = 1$ represents the maximum possible switching probability for cases with maximum grain boundary mobility and maximum scalar driving force ($p_s^{max} = 6$ MPa), equation (26).

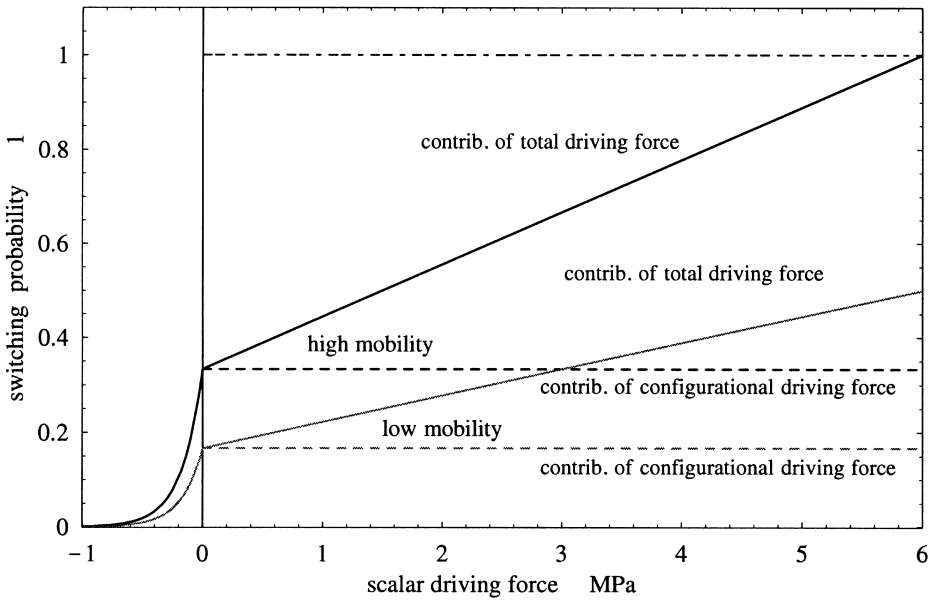

Fig. 6. Scaled single-site Metropolis-type switching probability as a function of the scalar driving force for two different grain boundary mobilities. The dashed lines show the transition probability for configurational driving forces and the solid lines for the total driving force. The black lines indicate high mobility and the gray lines low mobility. The temperature was constant. The dashed line at $W = 1$ represents the maximum possible switching probability for cases with maximum grain boundary mobility and maximum scalar driving force ($p_s^{max} = 6$ MPa), equation (27).

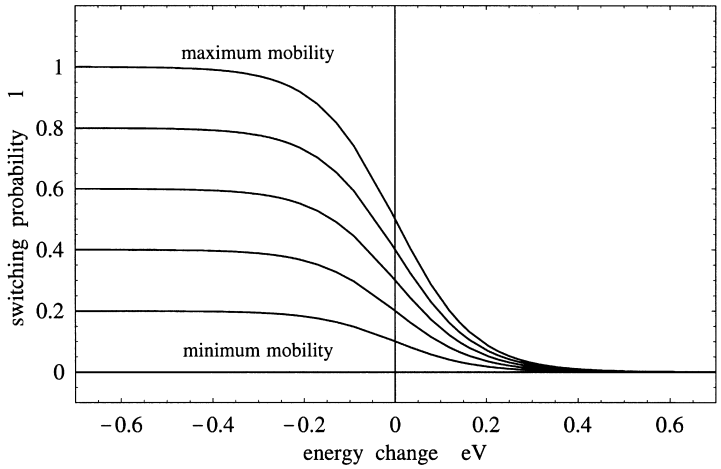

Fig. 7. Scaled single-site Glauber-type transition function for pure curvature driven grain growth at constant temperature for grain boundaries of different mobility. The transition probabilities are independent of the driving force, equation (28).

$$\tilde{W}_{\mathrm{M}} = \begin{cases} \left(\dfrac{m^i}{m^{\max}}\right)\left(\dfrac{p_{\mathrm{c}}^{\max}}{p_{\mathrm{c}}^{\max}+p_{\mathrm{s}}^{\max}}\right)\exp\left\{-\dfrac{\Delta E}{k_{\mathrm{B}}T}\right\} & \text{if } \Delta E > 0 \\ \left(\dfrac{m^i}{m^{\max}}\right)\left(\dfrac{p_{\mathrm{c}}^{\max}+p_{\rho,\mathrm{s}}^{i}}{p_{\mathrm{c}}^{\max}+p_{\mathrm{s}}^{\max}}\right) & \text{if } \Delta E \leq 0. \end{cases} \tag{27}$$

These modified single-site transition functions predict a switching probability different from zero even if all non-configurational local driving forces are absent. The transition probability is then exclusively due to configurational contributions. The driving force term in equations (26) and (27) has the constant maximum configurational driving force both in the numerator and in the denominator. For the case of energy decrease the driving force term additionally contains the local scalar driving force in the numerator and the maximum scalar driving force in the denominator. This means that the maximum possible transition probability in the direction of the driving force is exactly equal to one if the local mobility is equal to the maximum mobility ($m^i = m^{\max}$) and if at the same time the local scalar portion of the driving force is equal to its maximum possible value ($p_{\rho,\mathrm{s}}^i = p_{\mathrm{s}}^{\max}$).

The only situation where the transition probability becomes equal to zero occurs for a local grain boundary which has zero mobility ($m^i = 0$). This is conceivable for small angle boundaries and certain twin boundaries. Figures 5 and 6 show the switching probability as a function of the local scalar driving force stemming from stored dislocations

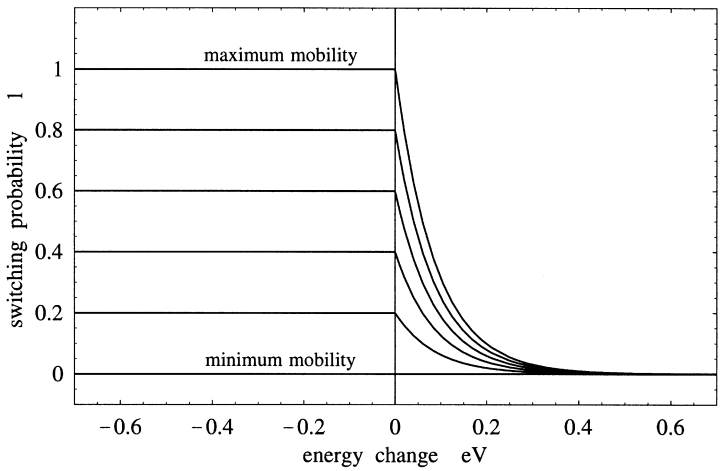

Fig. 8. Scaled single-site Metropolis-type transition function for pure curvature driven grain growth at constant temperature for grain boundaries of different mobility. The transition probabilities are independent of the driving force, equation (29).

$p^i_{\rho,s}$ for the scaled Glauber transition function and for the scaled Metropolis transition function according to equations (26) and (27).

4.3. Formulation for pure curvature driven grain growth

This section presents scaled versions of the above introduced switching probability functions for pure curvature driven grain growth simulations where no scalar contributions to the driving force occur.

The corresponding single-site switching functions can be derived from equations (26) and (27) by simply dropping the terms for the scalar driving force (Figs 7 and 8). The Glauber function then reduces to

$$\check{W}_{Gl} = \left(\frac{m^i}{m^{max}}\right)\left(1 + \exp\left\{\frac{\Delta E}{k_B T}\right\}\right)^{-1}. \quad (28)$$

The Metropolis transition function for this case reduces to

$$\check{W}_M = \begin{cases} \left(\frac{m^i}{m^{max}}\right)\exp\left\{-\frac{\Delta E}{k_B T}\right\} & \text{if } \Delta E > 0 \\ \left(\frac{m^i}{m^{max}}\right) & \text{if } \Delta E \leq 0. \end{cases} \quad (29)$$

Equations (28) and (29) show that scaling for pure grain growth simulations can be obtained by simply multiplying the original single-site switching functions, equations (2) and (3), by the ratio of the local and the maximum values of the grain boundary mobility.

Monte Carlo simulations on the basis of the scaled Metropolis transition function for curvature driven grain growth, equation (29), have recently been conducted by Rollett [36, 37].

5. CONCLUSIONS

The paper introduced a method for scaling Monte Carlo kinetics of the Potts model using Turnbull's rate theory of grain boundary motion. The method is designed for the kinetic and spatial scaling of multistate Potts models using one or more sets of non-conserved discrete structural or orientational state variables as employed for simulating recrystallization and curvature driven grain growth phenomena.

The scaling is based on the equivalence of single-site state switches in the Potts model and grain boundary motion as described by rate theory mapped on a simulation lattice.

According to this method the switching probabilities can be scaled by the ratio of the local and the maximum occurring values of the grain boundary mobility and by the ratio of the local and the maximum occurring values of configurational and scalar contributions to the driving force. The real time step elapsing during one Monte Carlo time step is scaled by the maximum occurring grain boundary mobility, the maximum occurring driving force, and the lattice parameter of the simulation grid.

Various scaled Glauber- and Metropolis-type transition functions were derived and discussed with respect to applications in the fields of recrystallization and grain growth Monte Carlo simulations.

Acknowledgements—The author gratefully acknowledges valuable discussions with A. D. Rollett and the financial support by the Deutsche Forschungsgemeinschaft through the Heisenberg program.

REFERENCES

1. Anderson, M. P., Srolovitz, D. J., Grest, G. S. and Sahni, P. S., *Acta metall.*, 1984, **32**, 783.
2. Srolovitz, D. J., Anderson, M. P., Sahni, P. S. and Grest, G. S., *Acta metall.*, 1984, **32**, 793.
3. Glazier, J. A., Anderson, M. P. and Grest, G. S., *Phil. Mag. B*, 1990, **62**, 615.
4. Mehnert, K. and Klimanek, P., *Comput. Mater. Sci.*, 1997, **9**, 261.
5. Mehnert, K. and Klimanek, P., in *Texture and Anisotropy of Polycrystals*, ed. R. Schwarzer. Trans Tech Publications, Switzerland, 1998, p. 425.
6. Srolovitz, D. J., *Computer Simulation of Microstructural Evolution*. The Metallurgical Society of AIME, Warrendale, PA, 1986.
7. Anderson, M. P. and Rollett, A. D., *Simulation and Theory of Evolving Microstructures*. The Minerals, Metals and Materials Society, TMS Publication, Warrendale, PA, 1990.
8. Holm, E. A., Rollett, A. D. and Srolovitz, D. J., in *Proceedings of NATO ASI on Computer Simulation in Materials Science*, ed. H. O. Kirchner, L. P. Kubin and V. Pontikis, *NATO Advanced Science Institutes Series, Series E, Applied Sciences*, Vol. 308. Kluwer Academic, Dordrecht, in cooperation with NATO Science Division, 1996, p. 373.
9. Tavernier, P. and Szpunar, J. A., *Acta metall.*, 1991, **39**, 549.
10. Tavernier, P. and Szpunar, J. A., *Acta metall.*, 1991, **39**, 557.
11. Srolovitz, D. J., Grest, G. S. and Anderson, M. P., *Acta metall.*, 1986, **34**, 1833.
12. Srolovitz, D. J., Grest, G. S., Anderson, M. P. and Rollett, A. D., *Acta metall.*, 1988, **36**, 2115.
13. Rollett, A. D., Srolovitz, D. J., Doherty, R. D. and Anderson, M. P., *Acta metall.*, 1989, **37**, 627.
14. Rollett, A. D., Luton, M. J. and Srolovitz, D. J., *Acta metall.*, 1992, **40**, 43.
15. Peczak, P., *Acta metall.*, 1995, **43**, 1297.
16. Srolovitz, D. J., Grest, G. S. and Anderson, M. P., *Acta metall.*, 1985, **33**, 2233.
17. Rollett, A. D., Srolovitz, D. J. and Anderson, M. P., *Acta metall.*, 1989, **37**, 1227.
18. Doherty, R. D., Li, K., Anderson, M. P., Rollett, A. D. and Srolovitz, D. J., in *Proceedings of the International Conference on Recrystallization in Metallic Materials, Recrystallization 1990*, ed. T. Chandra. The Minerals, Metals and Materials Society, TMS Publication, Warrendale, PA, 1990, p. 129.
19. Miodownik, M. A., in *Proceedings of the Third International Conference on Grain Growth, 1998*, ed.

H. Weiland. The Minerals, Metals and Materials Society, TMS Publication, Warrendale, PA, 1998.
20. Miodownik, M. A., Martin, J. W. and Cerezo, A., *Phil. Mag*., 1999, **79**, 203.
21. Gottstein, G., Molodov, D. A., Czubayko, U. and Shvindlerman, L. S., *J. Physique IV, colloque C3, supplément au J. Physique III*, 1995, **5**, 9.
22. Shvindlerman, L. S., Czubayko, U., Gottstein, G. and Molodov, D. A., in *Proceedings 16th RISØ International Symposium on Materials Science: Microstructural and Crystallographic Aspects of Recrystallization*, ed. N. Hansen, D. Juul Jensen, Y. L. Liu and B. Ralph. RISØ National Laboratory, Roskilde, Denmark, 1995, p. 545.
23. Gottstein, G., Shvindlerman, L. S., Molodov, D. A. and Czubayko, U., in *Dynamics of Crystal Surfaces and Interfaces*, ed. P. M. Duxbury and T. J. Pence. Plenum Press, New York, 1997, p. 109.
24. Gottstein, G., Molodov, D. A. and Shvindlerman, L. S., *Interface Sci*., 1998, **6**, 7.
25. Potts, R. B., *Proc. Camb. phil. Soc*., 1952, **48**, 106.
26. Glauber, R. J., *J. Math. Phys*., 1963, **4**, 294.
27. Metropolis, N., Rosenbluth, A. W., Rosenbluth, M. N., Teller, A. T. and Teller, E., *J. chem. Phys*., 1953, **21**, 1087.
28. Sahni, P. S., Srolovitz, D. J., Grest, G. S., Anderson, M. P. and Safran, B. A., *Phys. Rev*., 1983, **B28**, 2705.
29. Hassold, G. N. and Holm, E. H., *Comp. Phys*., 1993, **7**, 7.
30. Bortz, A. B., Kalos, M. H. and Lebowitz, J. L., *J. Comput. Phys*., 1975, **17**, 10.
31. Mehnert, K. and Klimanek, P., in *Proceedings of the 8th Joint EPS/APS International Conference on Physics Computing*, ed. P. Borcherds, M. Bubak and A. Maksymowicz. Academic Computer Centre, Cyfronet-Krakow, Poland, 1996, p. 57.
32. Safran, B. A., Sahni, P. S. and Grest, G. S., *Phys. Rev*., 1983, **B28**, 2693.
33. Holm, E. A., Zacharopoulos, N. and Srolovitz, D. J., *Acta mater*., 1998, **46**, 953.
34. Turnbull, D., *AIME*, 1951, **191**, 661.
35. Raabe, D., *Phil. Mag. A*, 1999, **79**, 2339.
36. Rollett, A. D., in *Proceedings of the Third International Conference on Grain Growth, 1998*, ed. H. Weiland. The Minerals, Metals and Materials Society, TMS Publication, Warrendale, PA, 1998.
37. Rollett, A. D. and Raabe, D., in *The Fourth International Conference on Recrystallization and Related Phenomena, 1999*, ed. T. Sakai and H. G. Suzuki. The Japan Institute of Metals, Sendai, 1999, p. 625.

ELSEVIER

Computational Materials Science 21 (2001) 69–78

COMPUTATIONAL MATERIALS SCIENCE

www.elsevier.com/locate/commatsci

A hybrid model for mesoscopic simulation of recrystallization

A.D. Rollett [a,*], D. Raabe [b]

[a] *Department of Materials Science and Engineering, Wean Hall 4315, Carnegie Mellon University, 5000 Forbes Avenue, Pittsburgh, PA 15213-2890, USA*

[b] *Max-Planck-Institut für Eisenforschung Max-Planck-Str. 1, 40237 Duesseldorf, Germany*

Received 17 November 1999; received in revised form 24 August 2000; accepted 10 October 2000

Abstract

A brief summary of simulation techniques for recrystallization is given. The limitations of the Potts model and the cellular automaton model as used in their standard forms for grain growth and recrystallization are noted. A new approach based on a hybrid of the Potts model (MC) and the cellular automaton (CA) model is proposed in order to obtain the desired limiting behavior for both curvature-driven and stored energy-driven grain boundary migration.

Keywords: Recrystallization; Modeling; Simulation; Monte Carlo; Potts model; Cellular automaton

1. Introduction

This paper gives a brief summary of mesoscopic methods for simulation of recrystallization and introduces a new approach for modeling the effects curvature-driven and stored energy-driven migration of boundaries. The standard form of the Monte Carlo (MC) model does not result in a linear relationship between migration rate and stored energy. On the other hand, the standard form of the cellular automaton (CA) model used for recrystallization does not allow for curvature as a driving force for migration. The basis for the new approach is the use of two different methods for determining orientation changes at each site in a lattice. The choice of which method to apply at any point in time is governed by weighting the probabilities for each type or reorientation attempt according to the desired balance in driving forces.

2. Summary of simulation methods

The need for computer simulation of recrystallization is driven by two different considerations. One is the need to be able to make quantitative predictions of the microstructure and properties of materials as affected by annealing. Simulation can be used to predict the average texture and grain size which strongly affect mechanical behavior. An equally important motivation for simulation, however, is the need for improved understanding of the recrystallization phenomenon that is highly complex from a microstructural point of view. The development of strong cube textures in fcc metals or the Goss texture in silicon steels, neither of

* Corresponding author. Tel.: +1-412-268-3177; fax: +1-412-268-1513.

E-mail address: rollett@andrew.cmu.edu (A.D. Rollett).

0927-0256/01/$ - see front matter
PII: S0927-0256(00)00216-0

which is fully understood, illustrates the importance of being able to model the recrystallization process in considerable detail. Indeed, since the microstructural evolution process inherent in recrystallization depends on the grain boundary properties which are sensitive to their crystallographic character then the importance of simulation techniques that can model the full range of boundary behavior is apparent.

Computer simulation of grain growth and recrystallization was strongly stimulated in the early 1980s by the realization that MC models could be applied to problems of grain structure evolution. By extension of the Ising model for domain modeling of magnetic domains to the Potts model, it was then possible to represent grains (domains) by regions of similarly oriented (lattice) points [1]. The models have been used, for example, to investigate texture evolution during grain growth and recrystallization, reinforced by parallel work on analytical models [2,3]. A critical issue addressed by Humphreys and others [4–8] extension of grain growth theory is that of coarsening of subgrain networks in order to clarify under what circumstances one expects to observe nucleation of recrystallization. This view of nucleation as simply non-uniform coarsening (i.e., abnormal subgrain growth) is significant for its blurring of the distinction between continuous and discontinuous recrystallization, at least for pure metals in which recovery is rapid.

There are a number of current methods of mesoscopic simulation for recrystallization. The geometrical, method addresses primarily the final microstructural state; it can be used to investigate microstructural evolution, provided that one is not concerned the effect of grain growth occurring in parallel. Such models of recrystallization were first elaborated by Mahin and Hanson [9] and then, developed further by Frost and Thompson [10]. Furu [11] and Juul Jensen [12] have recently extended these models to predict grain size and texture development during recrystallization.

The second method, based on network models, is an efficient way to represent microstructural evolution in discretized form [13–15]. These models are efficient because they abstract a key feature of the grain structure, i.e., the vertices or triple junctions between grain boundaries, and are therefore, efficient because only the vertex motion need be calculated, provided that local equilibrium can be assumed at triple junctions. They have some limitations when second phases must be considered, however, see also the work of Frost [16]. Humphreys [13] has applied the network model to the nucleation process in recrystallization by considering coarsening processes in subgrain networks and also in cases where second phase particles are present [17].

The CA and MC methods discretize the microstructure on a regular grid. Both methods have been successfully applied to recrystallization and solidification. The CA method uses physically based rules to determine the propagation rate of a transformation (e.g., recrystallization, solidification) from one cell to a neighbor [18–21]. The MC method as derived from the Potts model (i.e., a multistate Ising model), has been applied to a wide variety of problems in recrystallization [22–24]. The kinetic MC model simulates boundary motion via an energy minimization procedure for determining a reorientation probability at each step. Other methods that are suitable for recrystallization simulation include the phase-field model [25] and the finite element method [20,21].

3. Current status: limitations of the MC and CA models

Neither the MC model nor the CA model in their standard form is entirely satisfactory for studying boundary migration under the combined influence of two different driving forces. In grain growth, the driving force derives from the curvature of a boundary, [26] for which the MC model is satisfactory. In primary recrystallization, the driving force is the removal of stored dislocations by the migration of the recrystallization front, for which the CA model is satisfactory. In both cases, we expect to find a linear relationship between driving force and migration rate (velocity). The actual behavior of the MC model does not give this for stored energy as a driving force (except for low driving force, see below), however, and the CA

model does not allow for boundary curvature as a driving force.

In the case of the grain growth model implemented in the MC model, one writes a Hamiltonian for the system energy, E,

$$E = \frac{1}{2}\sum_{i}^{n}\sum_{j}^{\mathrm{NN}} J(S_i S_j)(1-\delta_{S_i S_j}), \tag{1}$$

where the inner sum is taken over the NN nearest neighbors of site i (typically first and second nearest neighbors), δ is the Kronecker delta function, and J is the energy of a unit of boundary between elements of indices S_i and S_j. To evolve the structure, a site and a new index are chosen at random. The element is reoriented to the new index with probability, P_{MC}, dependent on the change in energy, ΔE, and the local properties of the boundary.

$$P_{\mathrm{MC}}(S_i, S_j, \Delta E, T) = \begin{cases} \dfrac{J(S_i,S_j)}{J_{\max}}\dfrac{M(S_i,S_j)}{M_{\max}}, & \Delta E \leqslant 0, \\ \dfrac{J(S_i,S_j)}{J_{\max}}\dfrac{M(S_i,S_j)}{M_{\max}}\exp(-\Delta E/kT), & \Delta E > 0, \end{cases} \tag{2}$$

where ΔE is the energy change for the reorientation attempt, including both configurational and stored energy contributions (see Eq. (3), below), M is the boundary mobility between elements of indices S_i and S_j, $J_{\max}$ and $M_{\max}$ are the maximum boundary energy and mobility, respectively, k is the Boltzmann constant, and T is the lattice temperature. After each reorientation attempt, the time is incremented by $1/n$ Monte Carlo Steps (MCS), and a new reorientation is attempted. For a material with uniform boundary energy, the unit boundary energy plays no role in determining the transition probability. Only if a range of boundary energies and/or mobilities is present in the system is the transition probability decreased from the reference value.

It is instructive to plot the transition probabilities at zero temperature, Fig. 1, to illustrate that the transition probability remains at one for zero energy change. Discrete values of the energy change are shown, based on a triangular lattice

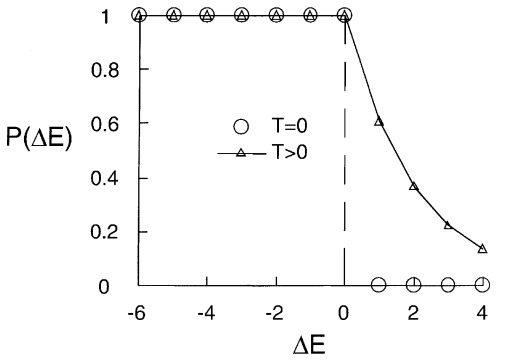

Fig. 1. Plot of transition probabilities for the Potts model as a function of the energy change: note the unit probability for zero energy change. The energy axis is in units of the interaction strength (J) nominally for a triangular lattice in which the maximum change is $\pm 6J$.

and $J = 1$. This feature is critical to the grain growth model because it means that kinks or steps on the boundaries can execute random walks along the boundaries. This, in effect, allows changes in curvature to be communicated along a boundary [27]. Modification of the transition probability from the reference condition decreases the probability linearly with either boundary energy and/or mobility [5].

The MC model has been used extensively to model recrystallization in which case a stored energy term, H_i, is added to the Hamiltonian.

$$E = \frac{1}{2}\sum_{i}^{n}\sum_{j}^{\mathrm{NN}} J(S_i S_j)(1-\delta_{S_i S_j}) + \sum_{i} H_i. \tag{3}$$

At low stored energies, $H < J$, and finite lattice temperature, a linear relationship between migration rate and driving force is recovered. The migration rate of a recrystallization front will be proportional (in the absence of a net curvature) to the difference in forward and backward reorientation rates. That is to say, for sites where the only change in energy is associated with removing or adding stored energy, the migration rate, v, is given by the following, where $J = 1$, $M = 1$, and $H \ll J$.

$$v \propto P_{\mathrm{forward}} - P_{\mathrm{backward}} = 1 - \exp\left\{-\frac{H}{T}\right\} \approx \frac{H}{T}. \tag{4}$$

The structure of a CA model is geometrically very similar with either a triangular or square lattice in two dimensions and either nearest neighbors included in the environment (NN, or von Neumann neighboring), or also next nearest neighbors (NNN, or Moore neighboring). For simulation of recrystallization, the switching rule is simple: any unrecrystallized cell (site) that has a recrystallized neighbor cell will switch to the orientation of that neighbor. Scaling of boundary migration rates is then achieved by relating the ratio of the unit distance (lattice repeat) in the model to the unit time step (maximum velocity in the model) to a maximum migration rate for the specified experiment. Note that the environment of orientations around the site to be reoriented does not affect the outcome of the individual reorientation step. Also if a range of mobilities is present in the system and/or a range of driving forces, then the transition probability is scaled according to a maximum value, following [20,21].

$$P = \frac{M(S_i, S_j)}{M_{\max}} \frac{\Delta H(S_i, S_j)}{\Delta H_{\max}}, \tag{5}$$

where P is the switching probability, M is a mobility that depends on the local boundary character and ΔH is the driving force (spatially variable) which is the difference in stored energy between site i and site j. Raabe also introduces an upper limit on the switching probability that scales with the number of trials such that the smaller the statistical variance desired, the lower the upper limit for the switching probability. The difference between conventional CA and the probabilistic CA models currently used is that in the latter approach: (a) sites are reoriented sequentially; (b) the location of the site to be reoriented is chosen at random; (c) any given reorientation step compares the transition probability to the output of a random number generator (over the interval 0–1) in order to determine whether or not that particular step is successful. Fig. 2 illustrates the variation in probability with magnitude of the change in energy associated with a given change in orientation, with the maximum probability set at unity. This allows for a linear scaling in boundary migration rate with driving force. Note, however, that no reorientation can occur if the energy change is zero or positive in contrast to the MC model.

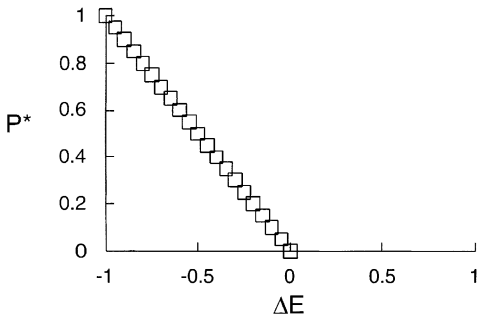

Fig. 2. Plot of the variation in switching probability in the CA model with a range of driving forces or mobilities present, each of which is scaled by a maximum value. Note that the probability goes to zero at zero change in energy.

Again, it is important to note that the framework of the CA model can be adapted to model curvature-driven grain growth provided that a probabilistic local rule is used that reproduces the switching probabilities of the MC model. Even the simultaneous updating of all sites inherent in the CA model can be accommodated by defining sublattices and performing updates on each sublattice in turn (see for example [28, p. 296]). A square lattice requires two sublattices, a triangular lattice requires three, a square lattice with Moore neighboring requires four, and so on. The principle for construction of the sublattices is that, all the neighbors of a site must belong to a different sublattice than that of the site itself. The issue remains of how to write a rule for reorientation that correctly combines both curvature and stored energy as driving forces for boundary motion. This point can be illustrated by attempting to write a switching probability for the combined effect of curvature and stored energy driving forces in order to obtain a linear relationship between migration rate and driving pressure. Based on the particular form presented here, Eq. (6a), the switching probability yields the desired limiting behavior if the grain boundary energy approaches zero, but does not if the stored energy approaches zero because energy neutral switches would have zero probability.

$$P(S_i,S_j,\Delta E,T) = \begin{cases} \left|\frac{\Delta E(S_i,S_j)}{\Delta E_{\max}}\right| \frac{J(S_i,S_j)}{J_{\max}} \frac{M(S_i,S_j)}{M_{\max}}, & \Delta E \leqslant 0, \\ \left|\frac{\Delta E(S_i,S_j)}{\Delta E_{\max}}\right| \frac{J(S_i,S_j)}{J_{\max}} \frac{M(S_i,S_j)}{M_{\max}} \exp(-\Delta E/kT), & \Delta E > 0. \end{cases} \tag{6a}$$

The alternative to this switching probability is to write an additive combination of the curvature and stored energies as follows, where it is understood that ΔE and J are dependent on the local boundary properties and local variations in stored energy.

$$P(S_i,S_j,\Delta E,T) = \begin{cases} \left|\frac{(\Delta E+J)}{(\Delta E+J)_{\max}}\right| \frac{M(S_i,S_j)}{M_{\max}}, & \Delta E \leqslant 0, \\ \left|\frac{(\Delta E+J)}{(\Delta E+J)_{\max}}\right| \frac{M(S_i,S_j)}{M_{\max}} \exp(-\Delta E/kT), & \Delta E > 0. \end{cases} \tag{6b}$$

This approach, however, suffers from the defect that the switching probability is not proportional to the change in stored energy as the latter approaches zero because the prefactor is dominated by the grain boundary energy term (J). In an effort to overcome the difficulties of combining the two types of driving force in a single switching probability model, a different approach has been taken.

4. Hybrid algorithm

The new algorithm described here adopts both types of evolution and combines them in a single *hybrid model*. The essence of the hybrid model is to interleave the two different types of reorientation in time. Each sub-model obeys the appropriate rules so that the correct limiting behavior is obtained in the limit that the frequency of either type approaches zero. Such a combination of switching rules has been used to model, e.g., ferromagnetic fluids [29] where it is useful to use spins can move according to a lattice gas model but spin interactions are governed by an Ising model, see p.293 et seq. [28]. A ratio, Γ, between the frequency of CA and MC reorientation attempts determines the relative magnitudes of the grain boundary energy compared with the stored energy. The MC reorientations are determined only by configurational energy such that only the first term on the RHS of Eq. (1) is used to determine ΔE. The effect of stored energy is incorporated into the CA model. For any given reorientation attempt, the choice of which type to apply is governed by a random number, R on the interval $(0,1)$: if the value of R is less than $\Gamma/1+\Gamma$, a CA reorientation is attempted, otherwise an MC reorientation attempt is made. The crucial advantage of this algorithm is that the motion of kinks on boundaries under energy-neutral changes in orientation is preserved which allows curvature driven motion to be modeled: the proportionality of the migration rate of a boundary to the stored energy difference across the boundary is also correctly modeled. Note that in the conventional MC model applied to recrystallization, [22], any energy change less than zero results in the same uniform switching probability (barring local variations in mobility). Therefore, variations in stored energy do not lead to any appreciable variation in boundary migration rate, although they do affect whether or not nucleation can occur homogeneously or heterogeneously [22,30].

5. Gibbs–Thomson

A useful test of the hybrid model is to investigate the behavior of an isolated (island) grain under the combined effects of curvature and stored energy driving forces. When only curvature is present, the grain will shrink by migration of all boundary segments towards their center(s) of curvature, i.e., the center of the grain. The curvature is inversely proportional to the radius and so the boundary velocity accelerates with time, leading to a characteristic constant rate of decrease of area, A, with time [31]. If the effect of a stored energy difference, ΔH, (higher stored energy outside the grain) is included, then $\mathrm{d}A/\mathrm{d}t$ is as follows, where M is a mobility as before, γ is the grain boundary energy and R is the radius of the 2D island grain.

$$\frac{dA}{dt} = -2\pi M\gamma + 2\pi RM\Delta H. \quad (7)$$

Thus, if the grain boundary energy is small and the stored energy difference is large, the grain will grow. For a linear velocity-force relation, one expects to observe a constant velocity, $v = M\Delta p$, and therefore, an accelerating (parabolic) rate of change of area. Furthermore, there should be a balance between the two forces at a critical size given by $\Delta H = \gamma/R_{\text{crit.}}$ ($\Delta H = \gamma/2R$ in the standard, 3D case).

In this hybrid kinetic MC model, the critical size can be estimated as follows for the smallest possible grain of size equal to a single site. Such a grain is surrounded by neighbors of a different orientation such that a fraction $1/Q$ MC reorientation attempts will result in absorption of the unit-size grain into one of its neighbors. If the grain is strain-free but all its neighbors have stored energy i.e., are unrecrystallized then any CA reorientation attempt will succeed in adding another site to the unit-size grain. Subsequent CA reorientations will continue to add more sites to the grain so that it continues to grow. This suggests that, in the limit where the critical grain size for recrystallization is that of unit-size grains, the reorientation frequency ratio is approximately $\Gamma = 1/Q = 0.01$. At larger sizes, however, the ratio should be larger. The analogous equation to Eq. (7) is therefore, the following, where α is effectively the product of mobility and grain boundary energy (in the MC model), μ is the mobility of a boundary in the CA model and Γ is the reorientation ratio. The mobility, μ, is not a free parameter but is determined by the characteristics of the particular form of MC model and CA model chosen.

$$\frac{dA}{dt} = -2\pi\alpha + 2\pi R\mu\Gamma. \quad (8)$$

Fig. 3 shows the area vs time for a single grain of initial radius $20a$ for various choices of the ratio, Γ, between MC and CA reorientations. The simulations were performed on a 50×50 square lattice with first and second nearest neighbors. Note that for ratios close to the critical value any fluctuation of the size will render the grain either super- or sub-critical leading to either growth or shrinkage. The results show the expected parabolic accelerating growth when stored energy dominates and linear shrinkage when curvature driving force dominates.

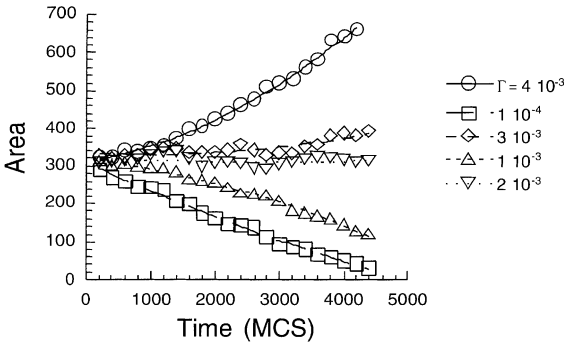

Fig. 3. Plot of area of single grain vs time for various ratios of reorientation frequencies, showing (linear) shrinkage for curvature dominated migration and (parabolic) expansion for stored energy migration. Each set of points has been fitted to a second order polynomial for the purposes of extracting the rate of change of area.

The critical size above which a new grain is stable ($dA/dt > 0$) can be estimated as follows. A single grain shrinking under curvature driven migration does so at a constant rate of change (loss) of area [1]. The magnitude of the rate is dependent on the value of Q because of the definition of the time step in the classical MC scheme. For $Q = 100$ used here and a square lattice, the rate is approximately $-0.1\ a^2\,\text{MCS}^{-1}$, where a is the size of each cell and 1 MCS represents one reorientation step for each cell. Choosing the grain boundary energy to be one sets the mobility, $\alpha = 0.016$. The expected boundary migration rate under stored energy driving force, however, should be approximately one cell per time step, i.e., $\mu = 1$. Therefore, for an isolated grain of size one, the reorientation ratio should be of order $\Gamma = 0.04$ for the curvature and stored energy driving forces to be in equilibrium. Testing the hybrid model at this resolution is impractical of course because statistical fluctuations will obscure the result of interest. Therefore, it is more useful to examine larger initial sizes.

Fig. 3 shows the variation in area with time of an island grain of size $R_0 = 20$ for various stored energies as expressed by the reorientation attempt

ratio. Small values of Γ allow the grain to shrink at a constant rate whereas large values lead to parabolic growth. At intermediate values, the grain is quasi-stationary although any fluctuation away from the zero growth size will lead to either continuing shrinkage or growth. In other words, the zero growth size is a metastable size. For this particular choice of initial grain size, zero growth occurs for $\Gamma \sim 0.002$. By setting $dA/dt = 0$ in Eq. (8), this leads to an estimate of the mobility of $\mu \sim 0.4$, which is not too far from unity, as expected. By differentiating the time dependence of the area one can obtain initial rates of change of area. Fig. 4 plots the slope of the area vs time at zero time for three different initial grain sizes and reorientation ratios between 0 and 0.01 with several trials for each set of parameter values. The results show some scatter in the growth rate but the growth rate appears to be linearly dependent on the reorientation ratio.

The relation for the rate of area change above predicts a linear dependence on initial radius with a constant intercept corresponding to a fixed shrinkage rate under the influence of curvature-driven migration only. Eq. (8) suggests that the contributions to the growth or shrinkage rate should all scale by the initial size (at $t = 0$). Fig. 5 therefore, presents the results of scaling the reorientation ratio, $\Gamma_{\text{scaled}} = \Gamma R_0/20$, for the results

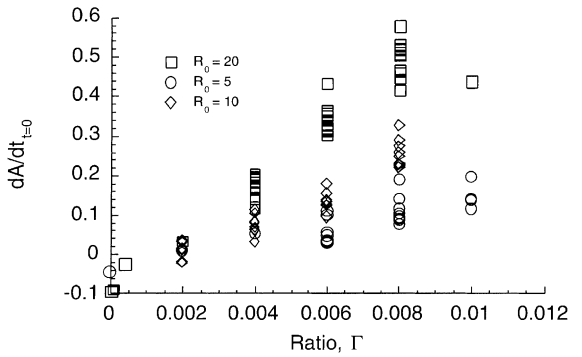

Fig. 4. Plot of initial rate of change of area of an island grain vs the reorientation frequency ratio for three different initials sizes. The larger the initial size of the grain, R_0, the smaller the stored energy required to allow the grain to grow. The predicted variation is approximately linear with stored energy and the ratio (stored energy) corresponding to zero growth is linear in the initial radius.

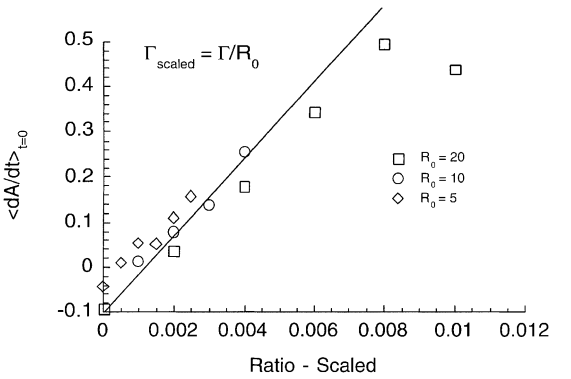

Fig. 5. Initial rate of change of area of an island grain for three different initial sizes, R_0. Each point represents the average for a set of simulations under the same conditions (as shown in Fig. 4). The reorientation ratio has been scaled, $\Gamma' = \Gamma \cdot R_0/20$, in accordance with Eq. (5).

shown in Fig. 4; each point represents an average of the set of trials for a given initial size and reorientation ratio. All the points lie close to a single straight line as expected although the trend is sublinear for large reorientation ratios.

Again, it is important to note that the concept of a critical grain size is not new in this context. Although it is not applicable to the standard form of the CA model as typically used to simulate recrystallization, a critical size can be readily defined in the standard form of the MC model as applied to recrystallization model. Holm [32] has investigated the range of critical sizes for various lattices as follows. Note that the focus is on minimum size required for an embryonic grain to survive and grow into a new grain. Also, certain sizes and shapes of embryonic grains have special properties owing to anisotropy of the lattice. A similar exploration of the behavior standard MC model for recrystallization for critical sizes could be performed. For small values of H/J and with finite lattice temperature, similar results may well be obtained (Table 1).

6. Recrystallization kinetics

In order to verify that the new hybrid model simulates primary recrystallization correctly, the

Table 1
Critical embryo sizes in the standard MC model for recrystallization (Eq. (3)) [32]

Stored energy: boundary energy	Critical size (lattice sites)
2D, triangular lattice	
$H/J < 2$	(very large)
$2 < H/J < 4$	2
$4 < H/J < 6$	1
$H/J > 6$	(any embryo grows)
2D, square lattice, with second nearest neighbors	
$H/J < 1$	(very large)
$1 < H/J < 2$	3
$2 < H/J < 8$	1
$H/J > 8$	(any embryo grows)
3D, simple cubic lattice, with second and third nearest neighbors	
$H/J < 3$	(very large)
$3 < H/J < 5$	5
$5 < H/J < 8$	3
$8 < H/J < 26$	1
$H/J > 26$	(any embryo grows)

behavior of a 2D system was modeled on a 100×100 square lattice with first and second nearest neighbors as before. The reorientation ratio, Γ, was varied and also the number of new grains. The model was operated in normal grain growth until a time of 1000 MCS had been accumulated and then, the recrystallization simulation was started by inserting new grains into the system. The resulting microstructures, Fig. 6, show the anticipated growth of new grains into a polycrystalline matrix that is also undergoing grain growth. The area fraction recrystallized was plotted in the usual double logarithmic plot, Fig. 7, for two values of Γ and three different densities of (site

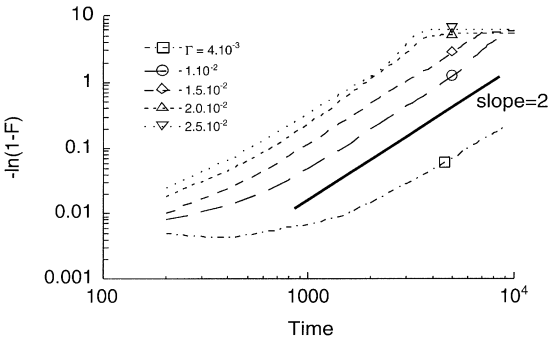

Fig. 7. JMAK plot of fraction recrystallized vs time for site saturated nucleation with 20 embryos and a range of reorientation ratios. Recrystallization proceeds less rapidly for smaller reorientation ratios, i.e., lower stored energy. The slope of the curves approaches two which is the classical value for spatially random, site saturated nucleation and two dimensional growth.

saturated) embryos. The results indicate that the expected Kolmogorov–Johnson–Mehl–Avrami kinetics for 2D growth under site-saturated nucleation conditions are followed, Eq. (9). That is to say, after an initial transient, a slope of two ($=n$) is observed for plots of $\log(\ln(1-F))$ vs log(time). The time for the preliminary grain growth stage has been subtracted from the total time. Since each embryonic grain is inserted into the microstructure with nine sites, i.e., a central site and its nearest neighbors, not all new grains survived. The disappearance of some new grains gives rise to a transient at short times, particularly for the smallest value of Γ. This aspect of the results suggests that the prior grain structure played a role by supporting heterogeneous nucleation [30].

$$1 - F = \exp -\{kt^n\}. \tag{9}$$

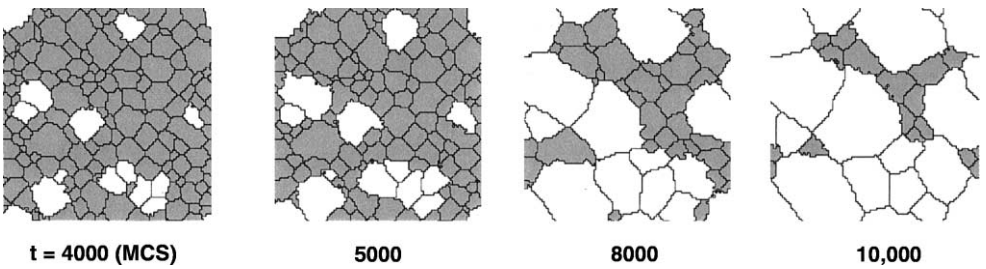

Fig. 6. Microstructural evolution during recrystallization for site saturated nucleation with 20 embryos and $\Gamma = 4 \times 10^{-3}$.

7. Scaling relationships

It is useful to examine scaling relationships between quantities such as time and length in the simulations and their corresponding physical quantities. This is most easily accomplished by considering parallel expressions for the same characteristic quantity. For length, the logical choice is the critical radius at which a nucleus is stable, i.e., $\mathrm{d}A/\mathrm{d}t = 0$ in Eq. (7). The physical critical size is given by:

$$R_{\text{crit.}}^{\text{physical}} = \frac{\gamma}{\Delta H}. \tag{10}$$

The corresponding expression for the critical radius in the simulations in terms of the areal shrinkage rate under curvature driven motion, $-2\pi\alpha$, the mobility in the CA model, μ, and the reorientation ratio, Γ, is given by:

$$R_{\text{crit.}}^{\text{model}} = \frac{\alpha}{\mu\Gamma}. \tag{11}$$

Equating the critical radii yields the following expression for scaling lengths.

$$x^{\text{physical}} = \frac{\gamma}{\Delta H}\frac{\mu\Gamma}{\alpha}x^{\text{model}}. \tag{12}$$

Since the quantities α and μ are intrinsic properties of the Monte Carlo and CA models respectively, the independent variable in the model is the reorientation ratio, Γ. For a given material with grain boundary energy, γ, and stored energy, ΔH, the larger the value chosen for Γ, the larger the effective magnification in the model (because of smaller $R_{\text{crit.}}$ in the model), or, alternatively, the lower the spatial resolution of the model.

For velocity scaling, one can consider the migration rate of a boundary under a difference in stored energy. In the physical case, the migration is given by, where M is the boundary mobility.

$$v^{\text{physical}} = M\Delta H. \tag{13}$$

In the model, the velocity is scaled by the fraction of steps that are governed by the CA rule:

$$v^{\text{model}} = \mu\frac{\Gamma}{1+\Gamma}. \tag{14}$$

Again, we can equate velocities to obtain a scaling relationship.

$$v^{\text{physical}} = \frac{M\Delta H}{\mu}\frac{1+\Gamma}{\Gamma}v^{\text{model}}. \tag{15}$$

Time scaling is then obtained as the length:velocity ratio:

$$t^{\text{physical}} = \frac{\text{length}}{\text{velocity}} = \frac{\gamma}{M(\Delta H)^2}\frac{\Gamma^2}{1+\Gamma}t^{\text{model}}. \tag{16}$$

In order to obtain a scaling relationship for time in the simulated recrystallization process for various values of the reorientation ratio, however, it is helpful to consider the KJMA relationship. Thus, consider the time required for 50% recrystallization in the case of site saturated, 2D growth. Rearrangement of the standard form, Eq. (9) above, where I is the nucleation density and G is the growth rate,

$$F = 1 - \exp\{-IG^2t^2\}$$

gives the following expression for $t_{50\%}$

$$t_{50\%}^2 = \ln 0.5/IG^2. \tag{17}$$

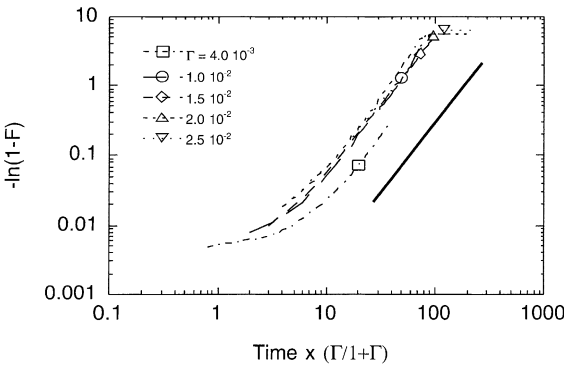

Fig. 8. JMAK plot of the fraction recrystallized vs normalized time according to Eq. (15). All the data follow a master curve describing recrystallization kinetics except for the smallest value of Γ: in this case, the low (effective) stored energy means that a significant fraction of the embryos do not survive to become new grains thereby retarding recrystallization, Eq. (13).

This shows that recrystallization times scale as the boundary velocities, Eq. (15), and not according to the time scaling given in Eq. (16), i.e.,

$$t_{50\%}(\Gamma') = \frac{\Gamma'}{1+\Gamma'}\,\frac{1+\Gamma}{\Gamma}\,t_{50\%}(\Gamma). \tag{18}$$

Fig. 8 shows the same set of data as in Fig. 7 but with the times scaled according to Eq. (18). All the data sets are scaled to the same curve except for the smallest value of Γ, for which not all the embryos survive to become new grains, thereby reducing the effective value of the nucleation density, I, in Eq. (17).

8. Summary

A new approach to mesoscopic simulation of recrystallization has been described that models the Gibbs–Thomson effect correctly. The simulation incorporates two types of reorientation process, one based on curvature-driven migration and one based on stored-energy driving forces. By allowing for two types of reorientation, it is possible to obtain the correct limiting behavior for both types of driving force for migration. The necessity for this arises from the non-local nature of the effect of curvature in the MC model. The kinetics of primary recrystallization for site-saturated conditions are correctly modeled. The hybrid approach can be generalized to three dimensions and should also be applicable to the kinetics and microstructural evolution of phase transformations.

Acknowledgements

Discussions with Professors R. Swendsen, J. Rickman and Drs. E. A. Holm and R. A. LeSar are gratefully acknowledged. This work was supported primarily by the MRSEC Program of the National Science Foundation under Award Number DMR-9632556.

References

[1] M.P. Anderson, D.J. Srolovitz, G.S. Grest, P.S. Sahni, Acta metall. 32 (1984) 783.
[2] G. Abbruzzese, K. Lucke, Acta Met. 34 (1986) 905.
[3] H.J. Bunge, U. Köhler, Scripta metall. et mater. 27 (1992) 1539.
[4] A.D. Rollett, W.W. Mullins, Scripta metall. et mater. 36 (1996) 975.
[5] A.D. Rollett, E.A. Holm, in: T.R. McNelley (Ed.), Proceedings of Recrystallization 96, ReX '96, 1997, p. 31.
[6] F.J. Humphreys, in: T.R. McNelley (Ed.), Proc. Recrystallization-96, ReX'96, 1997, p. 1.
[7] B. Radhakrishnan, G.B. Sarma, T. Zacharia, Scripta mat. 39 (1998) 1639.
[8] F.J. Humphreys, Acta mater. 45 (1997) 4321.
[9] K. Mahin, K. Hanson, J. Morris, Acta Met. 28 (1980) 443.
[10] H. Frost, C. Thompson, Acta Met. 35 (1987) 529.
[11] T. Furu, K. Marthinsen, E. Nes, Mater. Sci. Technol. 6 (1990) 1093.
[12] D. Juul Jensen, Scripta metall. et mater. 27 (1992) 1551.
[13] F.J. Humphreys, Scripta metall. et mater. 27 (1992) 1557.
[14] C. Maurice, F.J. Humphreys, in: H. Weiland, B.L. Adams, A.D. Rollett (Eds.), Proceedings of the Grain Growth in Polycrystalline Materials III, TMS, 1998, p. 81.
[15] V.E. Fradkov, L.S. Shvindlerman, D.G. Udler, Scripta metall. 19 (1985) 1285.
[16] H.J. Frost, C.V. Thompson, D.T. Walton, Acta metall. mater. 40 (1992) 779.
[17] F.J. Humphreys, in: H. Weiland, B.L. Adams, A.D. Rollett (Eds.), Proceedings of the Grain Growth in Polycrystalline Materials III, TMS, 1998, p. 13.
[18] M. Rappaz, C.-A. Gandin, Acta metall. mater. 41 (1993) 345.
[19] H.W. Hesselbarth, I.R. Göbel, Acta metall. 39 (1991) 2135.
[20] D. Raabe, Mater. Sci. Forum 273–275 (1998) 169.
[21] D. Raabe, Phil. Mag. A 79 (1999) 2339.
[22] D.J. Srolovitz, G.S. Grest, M.P. Anderson, Acta metall. 34 (1986) 1833.
[23] A.D. Rollett, D.J. Srolovitz, M.P. Anderson, R.D. Doherty, Acta metall. 40 (1992) 3475.
[24] P. Tavernier, J.A. Szpunar, Acta metall. mater. 39 (1991) 557.
[25] L.-Q. Chen, Scripta metall. et mater. 32 (1995) 115.
[26] C. Herring, Phys. Rev. 82 (1951) 87.
[27] P. Sahni, D. Srolovitz, G. Grest, M. Anderson, S. Safran, Phys. Rev. B 28 (1983) 2705.
[28] B. Chopard, M. Droz, Cellular Automata Modelling of Physical Systems, Cambridge University Press, Cambridge, 1998.
[29] V. Sofonea, Europhys. Lett. 25 (1994) 385.
[30] D.J. Srolovitz, G.S. Grest, M.P. Anderson, A.D. Rollett, Acta metall. 36 (1988) 2115.
[31] W.W. Mullins, J. Appl. Phys. 27 (1956) 900.
[32] E.A. Holm, personal communication, 1996.

Modelling Simul. Mater. Sci. Eng. **8** (2000) 445–462. Printed in the UK PII: S0965-0393(00)11463-9

Coupling of a crystal plasticity finite-element model with a probabilistic cellular automaton for simulating primary static recrystallization in aluminium

Dierk Raabe† and Richard C Becker‡

† Max-Planck-Institut für Eisenforschung, Max-Planck-Str. 1, 40237 Düsseldorf, Germany
‡ Lawrence Livermore National Laboratory, 7000 East Avenue, L-170 Livermore, CA 94550, USA

Received 20 October 1999, accepted for publication 31 January 2000

Abstract. The paper presents a two-dimensional approach for simulating primary static recrystallization, which is based on coupling a viscoplastic crystal plasticity finite-element model with a probabilistic kinetic cellular automaton. The crystal plasticity finite-element model accounts for crystallographic slip and for the rotation of the crystal lattice during plastic deformation. The model uses space and time as independent variables and the crystal orientation and the accumulated slip as dependent variables. The ambiguity in the selection of the active slip systems is avoided by using a viscoplastic formulation that assumes that the slip rate on a slip system is related to the resolved shear stress through a power-law relation. The equations are cast in an updated Lagrangian framework. The model has been implemented as a user subroutine in the commercial finite-element code Abaqus. The cellular automaton uses a switching rule that is formulated as a probabilistic analogue of the linearized symmetric Turnbull kinetic equation for the motion of sharp grain boundaries. The actual decision about a switching event is made using a simple sampling nonMetropolis Monte Carlo step. The automaton uses space and time as independent variables and the crystal orientation and a stored energy measure as dependent variables. The kinetics produced by the switching algorithm are scaled through the mesh size, the grain boundary mobility, and the driving force data. The coupling of the two models is realized by: translating the state variables used in the finite-element plasticity model into state variables used in the cellular automaton; mapping the finite-element integration point locations on the quadratic cellular automaton mesh; using the resulting cell size, maximum driving force, and maximum grain boundary mobility occurring in the region for determining the length scale, time step, and local switching probabilities in the automaton; and identifying an appropriate nucleation criterion. The coupling method is applied to the two-dimensional simulation of texture and microstructure evolution in a heterogeneously deformed, high-purity aluminium polycrystal during static primary recrystallization, considering local grain boundary mobilities and driving forces.

1. Motivation for coupling different spatially discrete microstructure and texture simulation methods

Time- and space-discretized simulation approaches such as the crystal plasticity finite-element method or cellular automata are increasingly gaining momentum as powerful tools for predicting microstructures and textures. The major advantage of such discrete methods is that they consider material heterogeneity as opposed to classical statistical approaches, which are based on the assumption of material homogeneity.

Although the average behaviour of materials during deformation and heat treatment can sometimes be sufficiently well described without considering local effects, prominent

examples exist where substantial progress in understanding and tailoring material response can only be attained by taking material heterogeneity into account. For instance, in the field of plasticity the quantitative investigation of ridging and roping, or related surface defects observed in sheet metals, requires knowledge about local effects such as the grain topology or the form and location of second phases. In the field of heat treatment, the origin of the Goss texture in transformer steels, the incipient stages of cube texture formation during primary recrystallization of aluminium, the reduction of the grain size in microalloyed low-carbon steel sheets, and the development of strong $\{111\}\langle uvw\rangle$ textures in steels can hardly be predicted without incorporating local effects such as the orientation and location of recrystallization nuclei and the character and properties of the grain boundaries surrounding them.

Although spatially discrete microstructure simulations have already profoundly enhanced our understanding of microstructure and texture evolution over the last decade, their potential is sometimes simply limited by an insufficient knowledge about the external boundary conditions that characterize the process and an insufficient knowledge about the internal starting conditions that are, to a large extent, inherited from the preceding process step. It is thus an important goal to improve the incorporation of both types of information into such simulations. External boundary conditions prescribed by real industrial processes are often spatially nonhomogeneous. They can be investigated using experiments or process simulations that consider spatial resolution. Spatial heterogeneities in the internal starting conditions, i.e. in the microstructure and texture, can be obtained from experiments or microstructure simulations that include spatial resolution.

In this paper we use the results obtained from a crystal plasticity finite-element simulation as starting conditions for a discrete recrystallization simulation carried out with a probabilistic cellular automaton. The coupling between both methods consists of: extracting and translating the state variables of the finite-element plasticity model (texture and accumulated shear) into state variables of the cellular automaton model (texture and dislocation density); mapping these data on the cellular automaton grid; scaling the cellular automaton mesh in terms of the derived cell size, maximum occurring driving force and grain boundary mobility; and in establishing an adequate nucleation criterion which makes use of these data.

The plan of the paper is as follows: we will separately present the basic features of both simulation methods in sections 2 and 3, explain the coupling method in section 4, and present the results of the recrystallization simulations in section 5.

2. The crystal plasticity finite-element model

2.1. Crystal constitutive model

The deformation behaviour of the grains is determined by a crystal plasticity model, which accounts for plastic deformation by crystallographic slip and for the rotation of the crystal lattice during deformation. Consequently, the model uses space and time as independent variables and the crystal orientation and the accumulated slip as dependent or state variables†. The crystal kinematics follow those described by Asaro (1983), and the rate-dependent formulation follows that developed by Peirce *et al* (1983). Here, however, the equations are cast in an updated Lagrangian framework rather than the total Lagrangian. The model has been implemented (Smelser and Becker 1989) as a user subroutine in the commercial finite-element code Abaqus and has been used in several studies to simulate deformation in grains and single crystals (Becker 1991, Becker *et al* 1991, 1995).

† The accumulated slip can be regarded as a state variable since it is used for the calculation of the slip system's resistance to shear.

In the crystal model, the velocity gradient, $\boldsymbol{L}$, is decomposed additively into elastic and plastic parts:

$$\boldsymbol{L} = \boldsymbol{L}^* + \boldsymbol{L}^{\mathrm{p}}. \tag{1}$$

Each of these can be further decomposed into its symmetric and antisymmetric parts representing, respectively, the rate of deformation tensor, $\boldsymbol{D}$, and the spin tensor, $\boldsymbol{\Omega}$:

$$\boldsymbol{L}^* = \boldsymbol{D}^* + \boldsymbol{\Omega}^* \tag{2}$$

$$\boldsymbol{L}^{\mathrm{p}} = \boldsymbol{D}^{\mathrm{p}} + \boldsymbol{\Omega}^{\mathrm{p}}. \tag{3}$$

The plastic part of the rate of deformation tensor, $\boldsymbol{D}^{\mathrm{p}}$, and the plastic spin, $\boldsymbol{\Omega}^{\mathrm{p}}$, can be expressed in terms of the slip rates, $\dot{\gamma}^{\alpha}$, along the crystallographic slip directions $\boldsymbol{s}_{\alpha}$ and on crystallographic slip planes with normals $\boldsymbol{m}_{\alpha}$:

$$\boldsymbol{D}^{\mathrm{p}} = \frac{1}{2}\sum_{\alpha=\mathbf{1}}^{N} \dot{\gamma}^{\alpha}(\boldsymbol{s}_{\alpha} \otimes \boldsymbol{m}_{\alpha} + \boldsymbol{m}_{\alpha} \otimes \boldsymbol{s}_{\alpha}) = \sum_{\alpha=\mathbf{1}}^{N} \dot{\gamma}^{\alpha}\boldsymbol{P}_{\alpha} \tag{4}$$

$$\boldsymbol{\Omega}^{\mathrm{p}} = \frac{1}{2}\sum_{\alpha=\mathbf{1}}^{N} \dot{\gamma}^{\alpha}(\boldsymbol{s}_{\alpha} \otimes \boldsymbol{m}_{\alpha} - \boldsymbol{m}_{\alpha} \otimes \boldsymbol{s}_{\alpha}) = \sum_{\alpha=\mathbf{1}}^{N} \dot{\gamma}^{\alpha}\boldsymbol{W}_{\alpha} \tag{5}$$

where $\boldsymbol{s}_{\alpha} \otimes \boldsymbol{m}_{\alpha}$ and $\boldsymbol{m}_{\alpha} \otimes \boldsymbol{s}_{\alpha}$ are the dyadic products of the slip vectors.

For the simulations on aluminium, which has a face-centred cubic (fcc) crystal structure, plastic deformation at low temperatures is typically assumed to occur on the 12 slip systems with $\langle 110 \rangle$ slip directions and $\{111\}$ slip planes, i.e. the slip vectors $\boldsymbol{s}_{\alpha} = \frac{1}{\sqrt{2}}(110)^{\mathrm{T}}$ and $\boldsymbol{m}_{\alpha} = \frac{1}{\sqrt{3}}(111)^{\mathrm{T}}$ are orthonormal.

The elastic stretch and the elastic rotation of the crystal lattice lead to a change of $\boldsymbol{s}_{\alpha}$ and $\boldsymbol{m}_{\alpha}$. This effect is captured by the elastic part of the velocity gradient. The slip vectors evolve during deformation according to

$$\dot{\boldsymbol{s}}_{\alpha} = \boldsymbol{L}^* \cdot \boldsymbol{s}_{\alpha} \tag{6}$$

$$\dot{\boldsymbol{m}}_{\alpha} = -\boldsymbol{m}_{\alpha} \cdot \boldsymbol{L}^*. \tag{7}$$

The slip vectors remain orthogonal so that the plastic portion of the deformation is nondilatant. By assuming a stress potential in which the stress is related to the elastic distortion of the crystal lattice, the rate of the Kirchhoff stress tensor, $\dot{\boldsymbol{\tau}}$, is given by

$$\dot{\boldsymbol{\tau}} = \mathbf{C} : \boldsymbol{D}^* + \boldsymbol{D}^* \cdot \boldsymbol{\tau} + \boldsymbol{\tau} \cdot \boldsymbol{D}^* + \boldsymbol{\Omega}^* \cdot \boldsymbol{\tau} - \boldsymbol{\tau} \cdot \boldsymbol{\Omega}^* \tag{8}$$

where $\mathbf{C}$ is a fourth-order tensor of the elastic moduli and $\boldsymbol{\tau}$ is the Kirchhoff stress tensor. Using the additive decomposition of the rate of deformation tensor and the spin into its elastic and plastic portions, and combining the second and third terms of equation (8) with the modulus to define a new fourth-order tensor, $\mathbf{K}$, the Jaumann rate tensor of the Kirchhoff stress rate can be written

$$\overset{\triangledown}{\boldsymbol{\tau}} = \mathbf{K} : \boldsymbol{D}^* - \mathbf{K} : \boldsymbol{D}^{\mathrm{p}} - \boldsymbol{\Omega}^{\mathrm{p}} \cdot \boldsymbol{\tau} + \boldsymbol{\tau} \cdot \boldsymbol{\Omega}^{\mathrm{p}} = \mathbf{K} : \boldsymbol{D}^* - \sum_{\alpha=\mathbf{1}}^{N} \dot{\gamma}^{\alpha}\boldsymbol{R}_{\alpha}. \tag{9}$$

The last three terms of equation (9) involve plastic deformation. They can be expressed in terms of slip rates as

$$\sum_{\alpha=\mathbf{1}}^{N} \dot{\gamma}^{\alpha}(\mathbf{K} : \boldsymbol{P}_{\alpha} + \boldsymbol{W}_{\alpha} \cdot \boldsymbol{\tau} - \boldsymbol{\tau} \cdot \boldsymbol{W}_{\alpha}) = \sum_{\alpha=\mathbf{1}}^{N} \dot{\gamma}^{\alpha}\boldsymbol{R}_{\alpha} \tag{10}$$

where $\boldsymbol{P}_\alpha$ and $\boldsymbol{W}_\alpha$ are defined in equations (4) and (5). Using equation (10), the Jaumann stress rate is given by

$$\overset{\triangledown}{\tau} = \mathbf{K} : \boldsymbol{D}^* - \sum_{\alpha=1}^{N} \dot{\gamma}^\alpha \boldsymbol{R}_\alpha. \tag{11}$$

The fourth-order modulus tensor, $\mathbf{K}$, is given in terms of the crystal moduli and the current stress state. The tensors $\boldsymbol{R}_\alpha$ are functions of the stress state and of the known crystal geometry.

What remains is to specify the slip rates, $\dot{\gamma}^\alpha$. In the rate-dependent constitutive formulation adopted here, the slip rate on a slip system is assumed to be related to the resolved shear stress on this system, $\tau^\alpha = \boldsymbol{\tau} : \boldsymbol{P}_\alpha$, through a power law relation:

$$\dot{\gamma}^\alpha = \dot{\gamma}_0^\alpha \left(\frac{\tau^\alpha}{\hat{\tau}^\alpha} \right)^{1/m} \tag{12}$$

where the scalar scaling parameter $\hat{\tau}^\alpha$, which has the unit of stress, is a phenomenological measure for the slip system strength or resistance to shear, $m = 0.002$ is the strain rate sensitivity exponent, and $\dot{\gamma}_0^\alpha = 0.03\ \mathrm{s}^{-1}$ is a reference shear rate. The value of the strain rate sensitivity exponent is low and the material response is almost rate-independent.

With the slip rates given as explicit functions of the known resolved shear stresses, the rate-dependent method avoids the ambiguity in the selection of active slip systems, which is encountered in many rate-independent formulations where it must be solved using an additional selection criterion. However, integration of the stress rate, equation (11), with the slip rate defined by equation (12) produces a system of equations which is numerically 'stiff'. The rate tangent modulus method of Peirce *et al* (1983) is used to increase the stable time step size.

For the present simulations, the strengths of all of the slip systems at a material point are taken to be equal, i.e. we adopt the Taylor hardening assumption. The hardening as a function of accumulated slip

$$\gamma = \int_0^t \sum_{\alpha=1}^{N} \dot{\gamma}^\alpha \, \mathrm{d}t' \tag{13}$$

is assumed to follow the macroscopic strain hardening behaviour obtained from a biaxial test by fitting the experimental data to a Voce equation

$$\sigma = 445.21 - 258.0 \exp(-5.1203\varepsilon)\ \mathrm{MPa} \tag{14}$$

where a satisfactory fit was obtained beyond $\varepsilon = 0.08$. The fit was adjusted by the average Taylor factor using an approximate value of three to give the slip system resistance to shear, equation (12), as a function of the accumulated shear:

$$\hat{\tau}^\alpha = 148.4 - 86.13 \exp(-1.0768\gamma)\ \mathrm{MPa}. \tag{15}$$

When applied in a polycrystal simulation of a tensile test, this treatment of the slip system hardening will approximately reproduce the hardening behaviour that was originally measured. The cubic elastic constants used in the simulation are typical for aluminium: $C_{11} = 108$ GPa, $C_{12} = 62$ GPa and $C_{44} = 28.3$ GPa (Smethells 1983).

2.2. *Original specimen and finite-element discretization*

The original specimen approximated here by the two-dimensional finite-element simulation was a quasi two dimensional columnar grain polycrystal of high-purity aluminium created by directional solidification (Becker 1998). The material was subsequently annealed to eliminate small grains and irregularities from the grain boundaries. The resulting grain size was of

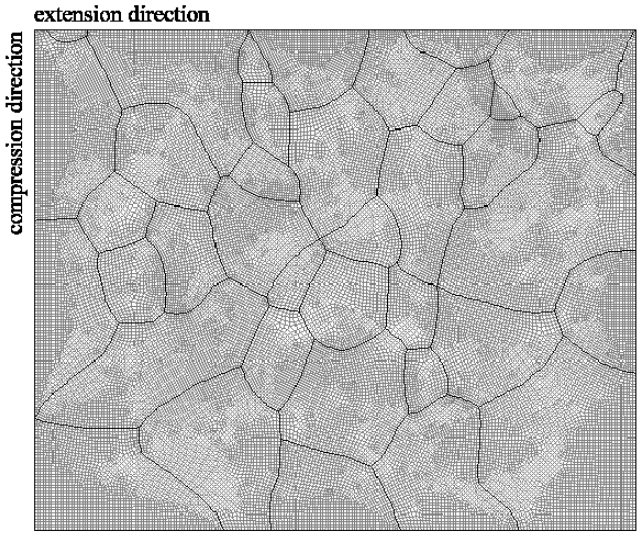

Figure 1. Distribution of the integration point locations in the finite-element mesh before deformation. According to a section of the real specimen, the finite-element sample has a size of 30×25 mm^2. The compression axis is along the 25 mm direction and extension is along the 30 mm direction.

the order of millimetres. A rectangular specimen $30 \times 25 \times 10$ mm^3 was excised for plane strain compression in a channel die. The axis of the columnar grains was aligned with the 10 mm direction of the sample. This was also the constraint direction for the channel die experiments. The compression axis was along the 25 mm direction and extension was along the 30 mm direction. The specimen was etched to reveal the grain structure. The crystal orientations of the 39 grains were determined using the electron backscatter technique in a scanning electron microscope. Both the grain structure and the crystallographic orientations taken from longitudinal sections were provided as input to the two-dimensional finite-element analyses.

Because a fine spatial discretization is desired for coupling the deformation results with the recrystallization model, a two-dimensional finite-element model was constructed. The finite-element mesh was created using the package Maze (1993). This mesh generator uses a paving algorithm in two dimensions to construct a mesh within each individual grain contour. The nodal locations are the same for elements on both sides of a grain boundary. The deformation was modelled as being continuous across grain boundaries. Grain boundary sliding and separation are not permitted. The mesh (figure 1) used 36 977 quadrilateral elements in the model plane.

3. The probabilistic cellular automaton

3.1. Fundamentals

The recrystallization model is designed as a cellular automaton with a probabilistic switching rule (Raabe 1998a,b, 1999). Independent variables are time t and space $x = (x_1, x_2, x_3)$. Space is discretized into an array of equally shaped quadratic cells. Each cell is characterized in terms of the dependent variables. These are scalar (mechanical, electromagnetic) and configurational (interfacial) contributions to the driving force and the crystal orientation $\boldsymbol{g} = \boldsymbol{g}(\varphi_1, \phi, \varphi_2)$,

where $\boldsymbol{g}$ is the rotation matrix and $\varphi_1, \phi, \varphi_2$ the Euler angles. The driving force is the negative change in Gibbs enthalpy G_t per transformed cell. The starting data, i.e. the crystal orientation map and the spatial distribution of the driving force, must be provided by experiment, i.e. orientation imaging microscopy via electron backscatter diffraction or by simulation, for example a crystal plasticity finite-element simulation as in this study. Grains or subgrains are mapped as regions of identical crystal orientation, but the driving force may vary inside these areas.

The kinetics of the automaton result from changes in the state of the cells, which are hereafter referred to as cell switches. They occur in accord with a switching rule, which determines the individual switching probability of each cell as a function of its previous state and the state of its neighbouring cells. The switching rule used in the simulations discussed below is designed for the simulation of primary static recrystallization. It reflects that the state of a nonrecrystallized cell belonging to a deformed grain may change due to the expansion of a recrystallizing neighbour grain, which grows according to the local driving force and boundary mobility. If such an expanding grain sweeps a nonrecrystallized cell the stored dislocation energy of that cell drops to zero and a new orientation is assigned to it, namely that of the growing neighbour grain.

To put this formally, the switching rule is cast in the form of a probabilistic analogue of the linearized symmetric rate equation of Turnbull (1951), which describes grain boundary motion in terms of isotropic single-atom diffusion processes perpendicular through a homogeneous planar grain boundary segment under the influence of a decrease in Gibbs energy:

$$\dot{\boldsymbol{x}} = \boldsymbol{n}\nu_{\mathrm{D}}\lambda_{\mathrm{gb}}c\left\{\exp\left(-\frac{\Delta G + \Delta G_{\mathrm{t}}/2}{k_{\mathrm{B}}T}\right) - \exp\left(-\frac{\Delta G - \Delta G_{\mathrm{t}}/2}{k_{\mathrm{B}}T}\right)\right\} \tag{16}$$

where $\dot{\boldsymbol{x}}$ is the grain boundary velocity, ν_{D} the Debye frequency, λ_{gb} is the jump width through the boundary, c is the intrinsic concentration of grain boundary vacancies or shuffle sources, $\boldsymbol{n}$ is the normal of the grain boundary segment, ΔG is the Gibbs enthalpy of motion through in the interface, ΔG_t is the Gibbs enthalpy associated with the transformation, k_{B} is the Boltzmann constant, and T is the absolute temperature. Replacing the jump width by the burgers vector and the Gibbs enthalpy terms by the total entropy, ΔS, and total enthalpy, ΔH, leads to a linearized form of equation (16):

$$\dot{\boldsymbol{x}} \approx \boldsymbol{n}\nu_{\mathrm{D}}b\exp\left(-\frac{\Delta S}{k_{\mathrm{B}}}\right)\left(\frac{pV}{k_{\mathrm{B}}T}\right)\exp\left(-\frac{\Delta H}{k_{\mathrm{B}}T}\right) \tag{17}$$

where p is the driving force and V is the atomic volume which is of the order of b^3, where b is the magnitude of the Burgers vector. Summarizing these terms reproduces Turnbull's expression

$$\dot{\boldsymbol{x}} = \boldsymbol{n}mp = \boldsymbol{n}m_0\exp\left(-\frac{Q_{\mathrm{gb}}}{k_{\mathrm{B}}T}\right)p \tag{18}$$

where m is the mobility. Equations (16)–(18) provide a well known kinetic picture of grain boundary segment motion, where the atomistic processes† are statistically described in terms of the pre-exponential factor of the mobility $m_0 = m_0(\Delta\boldsymbol{g}, \boldsymbol{n})$ and the activation energy of grain boundary mobility $Q_{\mathrm{gb}} = Q_{\mathrm{gb}}(\Delta\boldsymbol{g}, \boldsymbol{n})$. Both quantities may depend strongly on the misorientation $\Delta\boldsymbol{g}$ across the boundary, the grain boundary normal n, and the impurity content (Gottstein *et al* 1997, 1998, Doherty *et al* 1997, Molodov *et al* 1998).

† It must be emphasized in this context that thermal fluctuations, i.e. random forward and backward jumps of the atoms through the grain boundary are already included in equation (16). It is not required to consider any additional form of thermal fluctuation.

For dealing with competing switches affecting the same cell, the deterministic rate equation, equation (18), can be replaced by a probabilistic analogue that allows one to calculate switching probabilities. First, equation (18) is separated into a deterministic part, $\dot{\boldsymbol{x}}_0$, which depends weakly on temperature, and a probabilistic part, w, which depends strongly on temperature:

$$\dot{\boldsymbol{x}} = \dot{\boldsymbol{x}}_0 w = \boldsymbol{n}\frac{k_\mathrm{B}Tm_0}{V}\frac{pV}{k_\mathrm{B}T}\exp\left(-\frac{Q_\mathrm{gb}}{k_\mathrm{B}T}\right) \qquad \text{with}$$
$$\dot{\boldsymbol{x}}_0 = \boldsymbol{n}\frac{k_\mathrm{B}Tm_0}{V} \qquad w = \frac{pV}{k_\mathrm{B}T}\exp\left(-\frac{Q_\mathrm{gb}}{k_\mathrm{B}T}\right). \tag{19}$$

The probability factor w represents the product of the linearized part $pV/(k_\mathrm{B}T)$ and the nonlinearized part $\exp(-Q_\mathrm{gb}/(k_\mathrm{B}T))$ of the original Boltzmann terms. According to equation (19), nonvanishing switching probabilities occur for cells which reveal neighbours with a different orientation and a driving force which points in their direction. The automaton considers the first-, second- ($2D$), and third- ($3D$) neighbour shells for the calculation of the total driving force acting on a cell. The local value of the switching probability depends on the crystallographic character of the boundary segment between such unlike cells.

3.2. The scaled and normalized switching probability

The cellular automaton is usually applied to starting data that have a spatial resolution far above the atomic scale. This means that the automaton grid may have some mesh size $\lambda_\mathrm{m} \gg \mathrm{b}$. If a moving boundary segment sweeps a cell, the grain thus grows (or shrinks) by λ_m^3 rather than b^3. Since the net velocity of a boundary segment must be independent of the imposed value of λ_m, an increase of the jump width must lead to a corresponding decrease of the grid attack frequency, i.e. to an increase of the characteristic time step, and *vice versa*. For obtaining a scale-independent grain boundary velocity, the grid frequency must be chosen in a way to ensure that the attempted switch of a cell of length λ_m occurs with a frequency much below the atomic attack frequency that attempts to switch a cell of length b. Mapping equation (19) on a grid which is prescribed by an external scaling length λ_m leads to the equation

$$\dot{\boldsymbol{x}} = \dot{\boldsymbol{x}}_0 w = \boldsymbol{n}(\lambda_\mathrm{m}\nu)w \qquad \text{with} \qquad \nu = \frac{k_\mathrm{B}Tm_0}{V\lambda_\mathrm{m}} \tag{20}$$

where ν is the eigenfrequency of the chosen mesh characterized by the scaling length λ_m.

The eigenfrequency given by equation (20) represents the attack frequency for *one* particular grain boundary with constant mobility. In order to use a whole *spectrum* of mobilities and driving forces in one simulation it is necessary to normalize equation (20) by a common grid attack frequency ν_0 rendering it into

$$\dot{\boldsymbol{x}} = \dot{\boldsymbol{x}}_0 w = \boldsymbol{n}\lambda_\mathrm{m}\nu_0\left(\frac{\nu}{\nu_0}\right)w = \hat{\dot{\boldsymbol{x}}}_0\left(\frac{\nu}{\nu_0}\right)w = \hat{\dot{\boldsymbol{x}}}_0\hat{w} \tag{21}$$

where the normalized switching probability amounts to

$$\hat{w} = \left(\frac{\nu}{\nu_0}\right)\frac{pV}{k_\mathrm{B}T}\exp\left(-\frac{Q_\mathrm{gb}}{k_\mathrm{B}T}\right) = \frac{m_0 p}{\lambda_\mathrm{m}\nu_0}\exp\left(-\frac{Q_\mathrm{gb}}{k_\mathrm{B}T}\right). \tag{22}$$

The value of the normalization or grid attack frequency ν_0 can be identified by using the physically plausible assumption that the maximum occurring switching probability cannot be larger than one:

$$\hat{w}^\mathrm{max} = \frac{m_0^\mathrm{max}p^\mathrm{max}}{\lambda_\mathrm{m}\nu_0^\mathrm{min}}\exp\left(-\frac{Q_\mathrm{gb}^\mathrm{min}}{k_\mathrm{B}T}\right) \leqslant 1 \tag{23}$$

where $m_0^{\max}$ is the maximum occurring pre-exponential factor of the mobility, $p^{\max}$ is the maximum possible driving force, $\nu_0^{\min}$ is the minimum allowed grid attack frequency, and $Q_{\mathrm{gb}}^{\min}$ is the minimum occurring activation energy. With $\hat{w}^{\max} = 1$ in equation (23), one obtains the normalization frequency as a function of the upper bound input data:

$$\nu_0^{\min} = \frac{m_0^{\max} p^{\max}}{\lambda_{\mathrm{m}}} \exp\left(- \frac{Q_{\mathrm{gb}}^{\min}}{k_{\mathrm{B}} T} \right). \tag{24}$$

This frequency and the local values of the mobility and the driving force change equation (22) into

$$\begin{aligned} \hat{w}^{\mathrm{local}} &= \frac{m_0^{\mathrm{local}} p^{\mathrm{local}}}{\lambda_m \nu_0^{\min}} \exp\left(- \frac{Q_{\mathrm{gb}}^{\mathrm{local}}}{k_{\mathrm{B}} T} \right) = \left(\frac{m_0^{\mathrm{local}}}{m_0^{\max}} \right) \left(\frac{p^{\mathrm{local}}}{p^{\max}} \right) \exp\left(- \frac{(Q_{\mathrm{gb}}^{\mathrm{local}} - Q_{\mathrm{gb}}^{\min})}{k_{\mathrm{B}} T} \right) \\ &= \left(\frac{m^{\mathrm{local}} p^{\mathrm{local}}}{m^{\max} p^{\max}} \right). \end{aligned} \tag{25}$$

This expression is the central switching equation of the algorithm. It reveals that the local switching probability can be quantified by the ratio of the local and the maximum mobility $m^{\mathrm{local}}/m^{\max}$, which is a function of the grain boundary character and by the ratio of the local and the maximum driving pressure $p^{\mathrm{local}}/p^{\max}$. The probability of the fastest occurring boundary segment (characterized by $m_0^{\mathrm{local}} = m_0^{\max}$, $p^{\mathrm{local}} = p^{\max}$, $Q_{\mathrm{gb}}^{\mathrm{local}} = Q_{\mathrm{gb}}^{\min}$) to realize a cell switch is equal to one. Equation (25) shows that the mesh size does not influence the switching probability but only the time step elapsing during an attempted switch. The characteristic time constant of the simulation Δt is $1/\nu_0^{\min}$, equation (24).

The switching probability expressed by equation (25) can also be formulated in terms of the local time $t = \lambda_{\mathrm{m}}/\dot{x}$ required by a grain boundary with velocity $\dot{x}$ to cross the automaton cell of size λ_{m} (Gottstein 1999):

$$\hat{w}^{\mathrm{local}} = \left(\frac{m^{\mathrm{local}} p^{\mathrm{local}}}{m^{\max} p^{\max}} \right) = \left(\frac{\dot{x}^{\mathrm{local}}}{\dot{x}^{\max}} \right) = \left(\frac{t^{\max}}{t^{\mathrm{local}}} \right). \tag{26}$$

Therefore, the local switching probability can also be regarded as the ratio of the distances that were swept by the local grain boundary and the grain boundary with maximum velocity, or as the number of time steps the local grain boundary needs to wait before crossing the encountered cell. This reformulates the same underlying problem, namely that boundaries with different mobilities and driving forces cannot equally switch the state of the automaton in a given common time step.

There are two ways to cope with the problem. Either the time step is chosen such that the boundary with minimum probability crosses the cell, then the automaton will always switch state and boundaries with larger velocities will effect neighbouring cells. This is the approach Reher (1998) and Marx *et al* (1995, 1997, 1998) have chosen in their modified automaton. The alternative way is to clock the time step such as to have the boundary with the maximum velocity to cross the cell during one time step. In such a case, more slowly moving boundaries will not switch the cell and one would have to install a counter in the cell to account for that delay. The approach used in this paper principally pursues the latter method and solves it by using a stochastic decision rather than a counter to account for the insufficient sweep of the boundary through the cell. Stochastic Markov-type sampling is equivalent to installing a counter, since the probability to switch the automaton is proportional to the velocity ratio given by equations (25) and (26), provided the chosen random number generator is truly stochastic.

3.3. The switching decision

Equations (25) and (26) allow one to calculate the switching *probability* of a cell as a function of its previous state and the state of the neighbouring cells. The actual *decision* about a switching event for each cell is made by a Monte Carlo step. The use of random sampling ensures that all cells are switched according to their proper statistical weight, i.e. according to the local driving force and mobility between cells. The simulation proceeds by calculating the individual local switching probabilities $\hat{w}^{\text{local}}$ according to equation (25) and evaluating them using a nonMetropolis Monte Carlo algorithm. This means that for each cell the calculated switching probability is compared to a randomly generated number r which lies between zero and one. The switch is accepted if the random number is equal or smaller than the calculated switching probability. Otherwise the switch is rejected:

$$\text{random number } r \text{ between zero and one} \begin{cases} \text{accept switch} & \text{if } r \leqslant \left(\dfrac{m^{\text{local}} p^{\text{local}}}{m^{\max} p^{\max}} \right) \\ \text{reject switch} & \text{if } r > \left(\dfrac{m^{\text{local}} p^{\text{local}}}{m^{\max} p^{\max}} \right) \end{cases} . \tag{27}$$

Except for the probabilistic evaluation of the analytically calculated transformation probabilities, the approach is entirely deterministic. Thermal fluctuations other than included through equation (16) are not permitted. The use of realistic or even experimental input data for the grain boundaries (e.g. Gottstein *et al* 1997, 1998, Gottstein and Shvindlerman 1999, Molodov *et al* 1998) enables one to make predictions on a real time and space scale. The switching rule is scalable to any mesh size and to any spectrum of boundary mobility and driving force data. The state update of all cells is made in synchrony.

4. Coupling the crystal plasticity finite-element model with the probabilistic cellular automaton

4.1. Basic considerations about coupling

The coupling between the crystal plasticity finite-element model and the probabilistic cellular automaton was realized in four steps. First, the state variables of the finite-element plasticity model (crystal orientation and accumulated shear) were extracted and translated into state variables of the cellular automaton model (crystal orientation and dislocation density). Second, the integration point locations from the distorted finite-element mesh were mapped on the quadratic mesh of the automaton. Third, the resulting cell size, the maximum occurring driving force, and the maximum occurring grain boundary mobility were extracted from the mapped data for the determination of the length scale λ_{m}, the time step $\Delta t = 1/\nu_0^{\min}$ which elapses during the synchronous state update, equation (24), and the local switching probabilities $\hat{w}^{\text{local}}$, equation (25). Fourth, an appropriate nucleation criterion was defined in order to determine under which kinetic and thermodynamic conditions recrystallization started and which crystal orientations the switched nucleation cells assumed.

4.2. Selection of state variables

The first step in coupling the two methods consists in extracting or, respectively, translating appropriate state variables of the crystal plasticity finite-element model into state variables of the cellular automaton model. The state variables required in the recrystallization model are the crystal orientation and some measure for the stored elastic energy, e.g. the stored dislocation

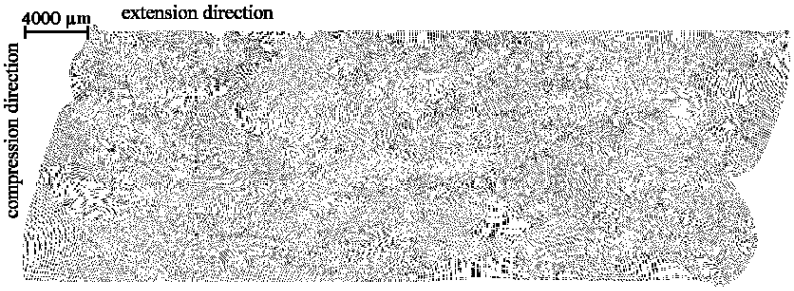

Figure 2. Distribution of the integration point locations in the finite-element mesh at a logarithmic strain of $\varepsilon = -0.434$.

density†. The state variables are given at the spatial coordinates of the integration points of the finite-element mesh.

The crystal orientations at these coordinates, i.e. the microtexture, was not discretized but directly used as calculated by the crystal plasticity finite-element method. Earlier calculations (Raabe 1998a,b) used a discretization method where each orientation is represented by the closest texture component from a set of discrete crystal orientations. The set contained 936 texture components which were equally distributed in orientation space. The use of a continuous instead of a discrete orientation space enhances the calculation speed. However, the required computer memory is enhanced as well.

The second state variable, i.e. the stored dislocation density was linearly related to the value of the accumulated slip known for each nodal point in the finite-element model. It should be noted at this point that recent crystal plasticity polycrystal simulations have not only predicted stored elastic energy arising from the accumulated shear (translated here into some stored dislocation density), but also some local residual elastic stresses which are orientation dependent, although these are not proportional to the shear accumulated during plastic deformation (Dawson *et al* 1999). At large plastic strains this additional elastic incompatibility pressure might not be significant, since the driving forces stemming from stored dislocations typically exceed those stemming from residual elastic stresses by at least an order of magnitude. However, at small strains it could be important to add these elastic stresses to the driving pressure.

4.3. Mapping procedure

The mesh of the finite-element model was aligned with each individual grain contour (figure 1). Since the grains revealed different kinematics and different strain hardening behaviours during deformation the mesh gradually became even more distorted with increasing strain. Figure 2 shows the distribution of the integration points at a logarithmic strain of $\varepsilon = 0.434$. The state variables given at these points had to be mapped on the regular cellular automaton mesh that consisted of quadratic cells.

Spatial compatibility between both types of models can, in principle, be attained by either directly interpolating the finite-element data on a quadratic cellular automaton mesh or by choosing an appropriate mapping procedure. The method we used is a Wigner–Seitz

† Recrystallization models working on a more microscopic scale would also aim at the incorporation of the dislocation cell structure (e.g. Humphreys 1992, 1997, Doherty *et al* 1997). Progress in recrystallization and recovery could then be described by discontinuous (recrystallization) and continuous (recovery) subgrain coarsening. The approach presented here works on a somewhat larger scale where dislocation cell coarsening is not explicitly considered.

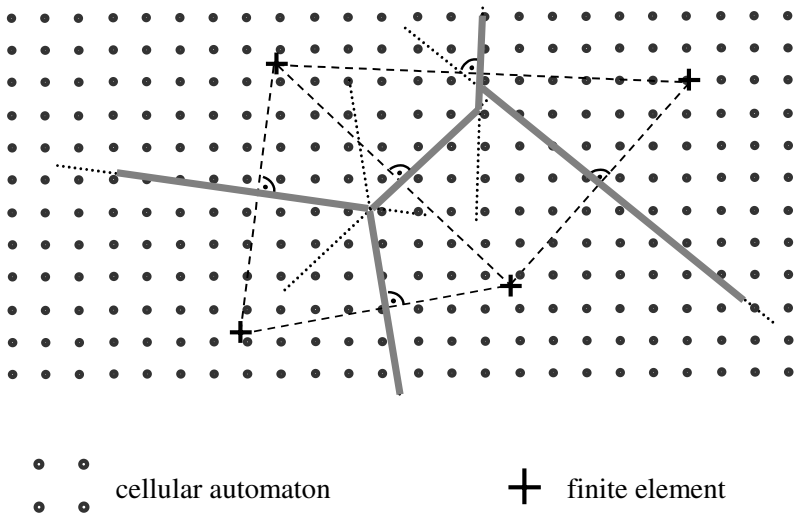

Figure 3. Schematic description of the Wigner–Seitz mapping algorithm. It consists of two steps. First, a fine quadratic grid (circles) is superimposed on the finite-element mesh (crosses). Second, values of the state variables at each of the integration points are assigned to the new grid points that fall within the Wigner–Seitz cell corresponding to that integration point. The Wigner–Seitz cells of the finite-element mesh are constructed from cell walls, which are the perpendicular bisecting planes of all lines connecting neighbouring integration points, i.e. the integration points are in the centres of the Wigner–Seitz cells.

type of mapping algorithm (Raabe 1999). It consisted of two steps. In the first step, a fine quadratic automaton grid was superimposed on the distorted finite-element mesh. The spacing of the points in the new grid was smaller than the spacing of the closest neighbour points in the finite-element mesh. The absolute value of the cell size of the superimposed quadratic cellular automaton mesh was thus determined by the size of the simulated specimen (see section 2.2). It amounted to $\lambda_{\mathrm{m}} = 61.9\ \mu$m. While the original finite-element mesh consisted of 36 977 quadrilateral elements, the cellular automaton mesh consisted of 217 600 cells. In the second step, values of the state variables at each of the integration points were assigned to the new grid points that fell within the Wigner–Seitz cell corresponding to that integration point. The Wigner–Seitz cells of the finite-element mesh were constructed from cell walls, which were the perpendicular bisecting planes of all lines connecting neighbouring integration points (figure 3), i.e. the integration points were in the centres of the Wigner–Seitz cells.

The Wigner–Seitz procedure requires that the cellular automaton grid is finer than the finite-element mesh, i.e. this mapping method produces clusters of cellular automaton sites with identical state variable properties surrounding each finite-element interpolation point. In the model these clusters correspond to regions of the same crystallographic orientation with a uniform nonzero dislocation density. The size of these cellular automaton clusters depends on the ratio between the average finite element point spacing and the cellular automaton site spacing. Since, at a later stage of the simulation (section 4.5), a nucleation criterion must be defined as a function of the local misorientation between neighbouring automaton cells, and since this criterion is only satisfied at the boundaries of the cellular automaton clusters, it is conceivable that the Wigner–Seitz approach might introduce a dependence on the finite-element mesh size.

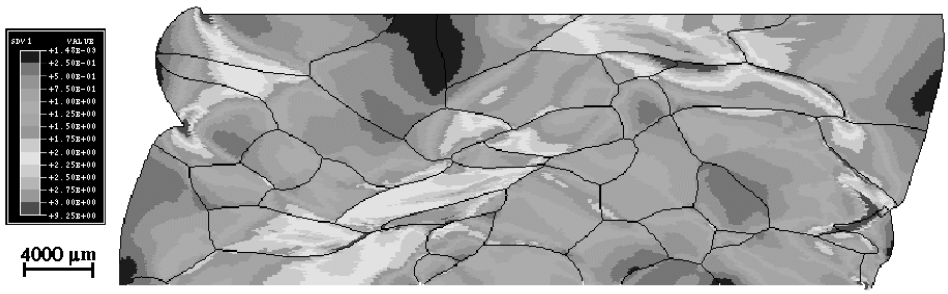

Figure 4. Distribution of the accumulated crystallographic shear strain in the finite-element sample at a logarithmic deformation of $\varepsilon = -0.434$.

4.4. Scaling procedure

The maximum driving force in the region arising from the stored dislocation density amounted to about 1 MPa. The temperature dependence of the shear modulus and of the Burgers vector was considered in the calculation of the driving force. The grain boundary mobility in the region was characterized by an activation energy of the grain boundary mobility of 1.46 eV and a pre-exponential factor of the grain boundary mobility of $m_0 = 8.3 \times 10^{-3}$ m^3 N^{-1} s^{-1}. Together with the scaling length $\lambda_m = 61.9$ μm we used these data for the calculation of the time step $\Delta t = 1/\nu_0^{\min}$, equation (24), and of the local switching probabilities $\hat{w}^{\text{local}}$, equation (25).

4.5. Nucleation criterion for recrystallization

The nucleation process during primary static recrystallization has been explained for pure aluminium in terms of discontinuous subgrain growth (Humphreys 1992, 1997, Doherty *et al* 1997). According to this model nucleation takes place in areas which reveal high misorientations among neighbouring subgrains and a high driving force for curvature-driven subgrain coarsening. The present simulation approach works above the subgrain scale, i.e. it does not explicitly describe cell walls and subgrain coarsening phenomena. Instead, we incorporated nucleation on a more phenomenological basis using the kinetic and thermodynamic instability criteria known from classical recrystallization theory (Himmel 1963, Haessner 1978, Gottstein 1984, Humphreys and Hatherly 1995). The kinetic instability criterion means that a successful nucleation process leads to the formation of a mobile, large-angle grain boundary. The thermodynamic instability criterion means that the stored energy changes across the newly formed large-angle grain boundary providing a net driving force. Nucleation in this simulation is performed in accord with these two aspects, i.e. potential nucleation sites must fulfil both the kinetic and the thermodynamic instability criterion. In the simulations two phenomenological nucleation models were implemented based on these instability criteria.

The first nucleation model is a variant of the subgrain coalescence model and is capable of creating new orientations. At the beginning of the simulation the kinetic conditions for nucleation were checked by calculating the misorientations among all neighbouring cells. If a pair of cells revealed a misorientation above 15°, the thermodynamic criterion, i.e. the local value of the dislocation density was also checked. If the dislocation density was larger than some critical value of its maximum value in the sample (we checked 10%, 30%, 50%, 70%, 80% and 90%), the two cells were recrystallized, i.e. a new orientation midway between the two

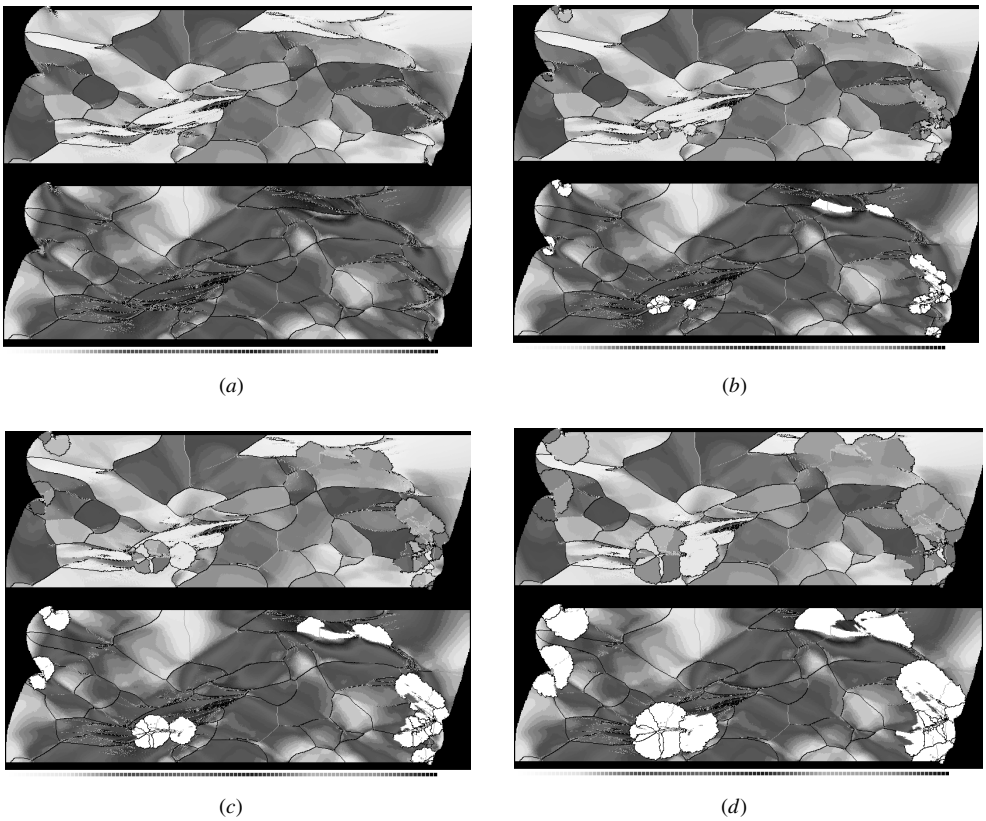

Figure 5. 2D simulations of primary static recrystallization in a deformed aluminium polycrystal on the basis of crystal plasticity finite-element data. The figure shows the change both in microtexture (upper images) and in dislocation density (lower images), which was derived from the value of the accumulated crystallographic shear, as a function of the annealing time during isothermal recrystallization. The white areas in the lower images indicate a stored dislocation density of zero, i.e. they are recrystallized. The black lines in both figures indicate misorientations above 15° and the thin grey lines indicate misorientations between 5° and 15°, irrespective of the rotation axis. The orientation image given in the upper figures represents different crystal orientations by different grey levels. The simulation parameters are: annealing temperature, 800 K; site-saturated nucleation conditions; kinetic instability criterion, misorientation above 15°; thermodynamic instability criterion, dislocation density larger than 70% of the maximum occurring value; maximum occurring driving force, 1 MPa; activation energy of the grain boundary mobility, 1.46 eV; pre-exponential factor of the grain boundary mobility, $m_0 = 8.3 \times 10^{-3}$ m^3 N^{-1} s^{-1} and mesh size of the cellular automaton grid (scaling length), $\lambda_m = 61.9$ μm. The images show a crystal in the following states of recrystallization: (*a*) 0%, (*b*) 3%, (*c*) 13%, (*d*) 22%, (*e*) 32%, (*f*) 48%, (*g*) 82% and (*h*) 93% recrystallized.

original orientations was created and a dislocation density of zero was assigned to them. The generation of the new orientation was based on the idealized picture of subgrain coalescence (Hu 1963). If the two recrystallized cells had a misorientation above 15° with respect to the nonrecrystallized neighbour cells they could grow into the surrounding matrix.

The second nucleation model is even simpler and does not create new orientations. At the beginning of the simulation, the thermodynamic criterion, i.e. the local value of the dislocation density, was first checked for all grid points. If the dislocation density was larger than some critical value of its maximum value in the sample (we checked 10%, 30%, 50%, 70%, 80%

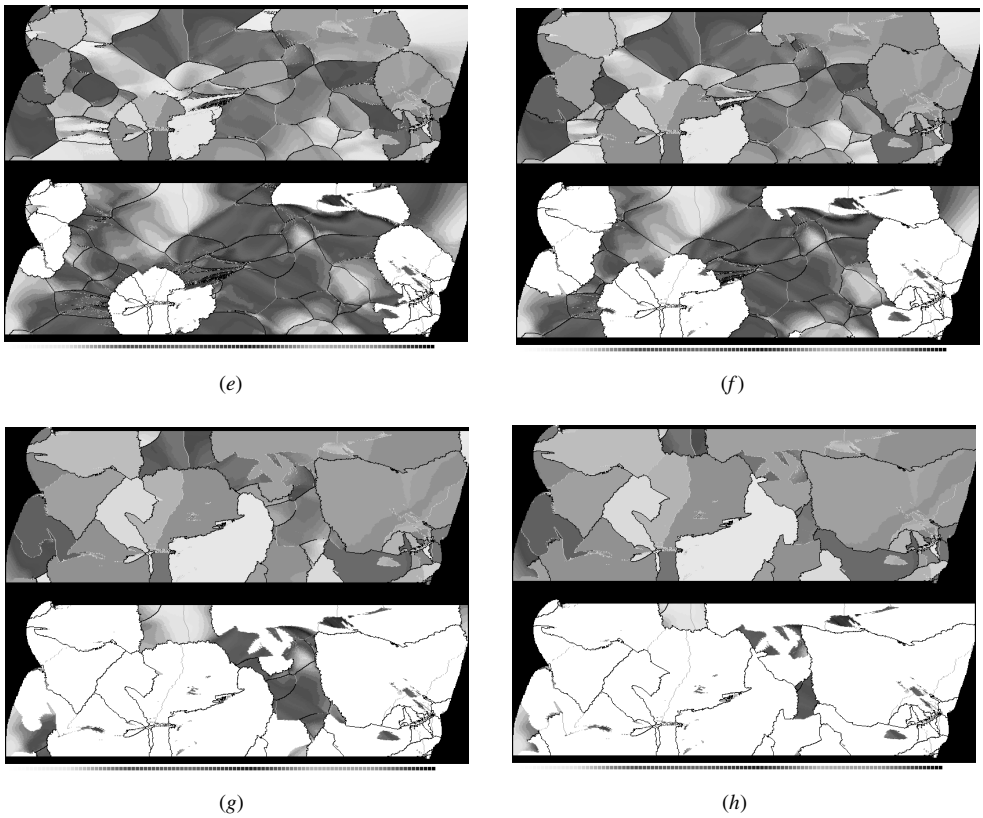

(*e*) (*f*)

(*g*) (*h*)

Figure 5. (Continued)

and 90%), the cell was spontaneously recrystallized without any orientation change, i.e. a dislocation density of zero was assigned to it and the original crystal orientation was preserved. In the next step the ordinary growth algorithm was started according to equations (25)–(27), i.e. the kinetic conditions for nucleation were checked by calculating the misorientations among all spontaneously recrystallized cells (preserving their original crystal orientation) and their immediate neighbourhood considering the first-, the second-, and the third-neighbour shells. If any such pair of cells revealed a misorientation above 15°, the cell flip of the unrecrystallized cell was calculated according to equations (25)–(27). In case of a successful cell flip, the orientation of the first recrystallized neighbour cell was assigned to the flipped cell. All simulation results presented hereafter used the second nucleation model.

5. Simulation of primary static recrystallization

Figure 4 shows the starting conditions prior to the simulated annealing treatment, i.e. the distribution of the accumulated crystallographic shear in the sample after a total logarithmic strain of $\varepsilon = -0.434$. The distribution of the integration points of the finite-element mesh was shown in figure 2. Figure 4 reveals three major areas with large values of the accumulated shear (bright areas). These areas can be referred to as deformation bands.

Figure 5 shows the change both in microtexture and in dislocation density, which was assumed to be proportional to the accumulated crystallographic shear, as a function of the

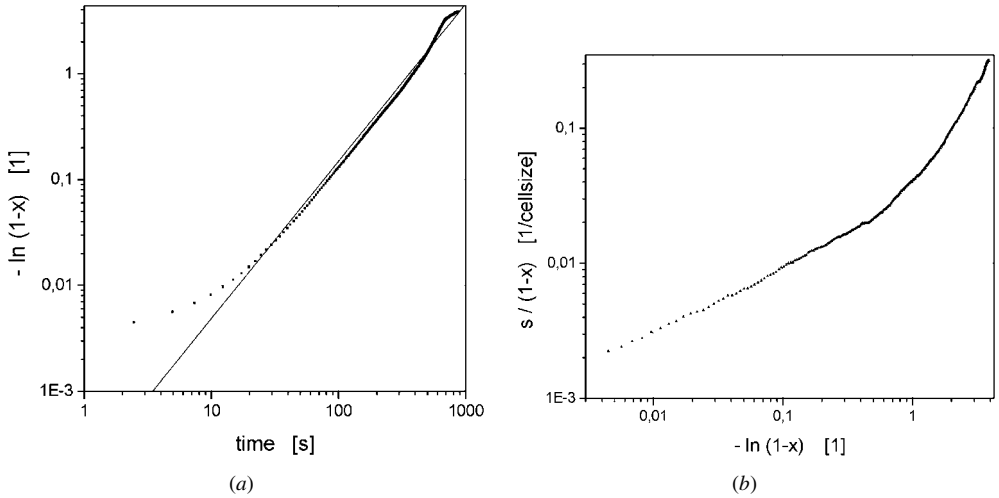

(*a*) (*b*)

Figure 6. Simulated recrystallized volume fraction ((*a*) Avrami diagram) and interface fraction ((*b*) Cahn–Hagel diagram) as functions of the annealing time. The temperature was 800 K.

annealing time during recrystallization. The annealing temperature was 800 K. The simulation assumed site-saturated nucleation conditions using the second nucleation criterion described in the preceding section, i.e. potential nuclei were spontaneously formed at $t = 0$ s in cells with a dislocation density larger than 70% of the maximum value in the sample. These potential nuclei then grew or remained unchanged in accord with equations (25)–(27).

The upper images in figure 5 show the orientation images where each grey level represents a specific crystal orientation. The grey level is calculated as the magnitude of the Rodriguez orientation vector. The cube component serves as a reference orientation. The lower images in figure 5 show the stored dislocation densities. The white areas are recrystallized, i.e. the stored dislocation content of the affected cells was dropped to zero. The black lines in both figures indicate misorientations above 15° irrespective of the rotation axis. The thin grey lines in both figures indicate misorientations above 5° and below 15° irrespective of the rotation axis.

The incipient stages of recrystallization (figures 5(*a*)–(*c*)) reveal that nucleation is concentrated in areas with large accumulated local shear strains and lattice curvatures (figure 4). This means that the spatial distribution of the nuclei is very inhomogeneous. The deformation bands with high localized stored energy and lattice curvature produce clusters of similarly oriented nuclei. Less deformed areas between the bands show a negligible density of nuclei. The following stages of recrystallization (figures 5(*d*)–(*f*)) reveal that the nuclei do not grow freely into the surrounding deformed material as described by Avrami–Johnson–Mehl theory, but impinge upon each other and thus compete, already, at a very early stage of the transformation. The late stages of recrystallization show an incomplete and spatially heterogeneous transformation of the deformed material (figures 5(*g*) and (*h*)).

The observed deviation from Avrami–Johnson–Mehl-type growth, i.e. the early impingement is reflected by the kinetic behaviour which differs from the classical sigmoidal kinetics observed under homogeneous nucleation conditions (figure 6). The kinetics simulated on the basis of the finite-element data in conjunction with the chosen nucleation model reveal an Avrami exponent of about 1.4, which is for below the theoretical value for site-saturated

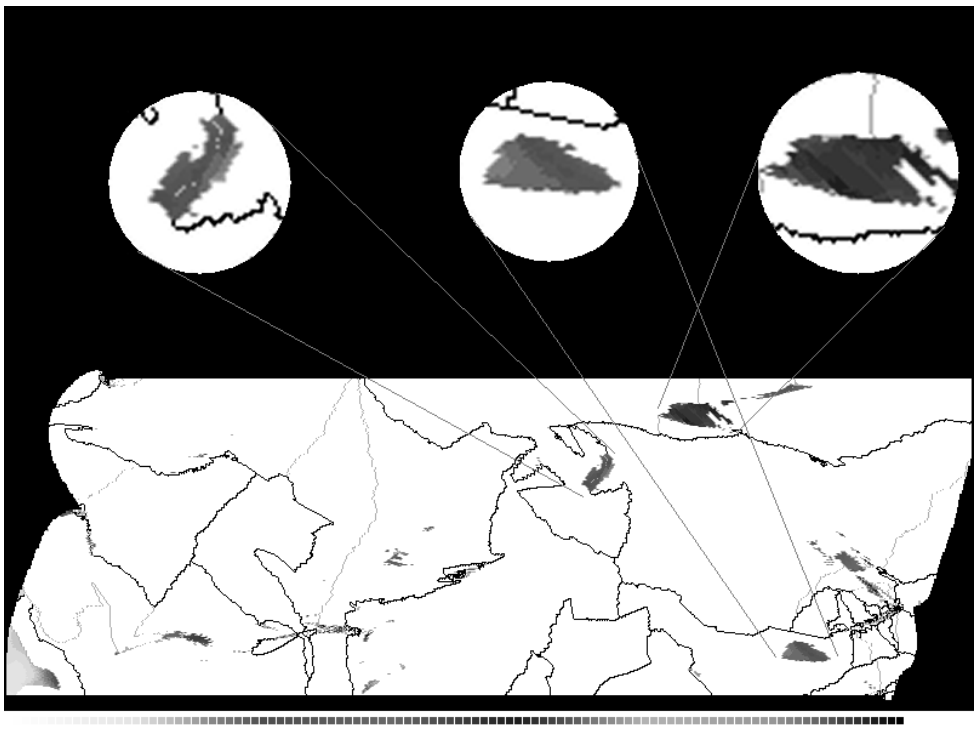

Figure 7. Magnification of three selected areas where moving large-angle grain boundaries did not sweep the deformed material. This pronounced recovery is due to insufficient misorientations between the deformed and the recrystallized areas entailing a drop in grain boundary mobility (orientation pinning).

nucleation conditions in two dimensions of two (figure 6(*a*)). Figure 6(*b*) shows the corresponding Cahn–Hagel plot. A more systematic analysis of such nucleation behaviour, which is characterized by an early growth competition, might help to identify approaches for the optimization and even tailoring of recrystallization kinetics, texture, and grain size.

Another interesting result of the simulation is the partial recovery of deformed material. Figure 7 shows three selected areas where moving large angle-grain boundaries did not sweep the deformed material. An analysis of the state variable values at these coordinates and of the grain boundaries involved substantiates that not insufficient driving forces, but insufficient misorientations between the deformed and the recrystallized areas—entailing a drop in grain boundary mobility—were responsible for this effect. Previous authors referred to this mechanisms as orientation pinning (Juul Jensen 1997).

Figure 8 shows the crystallographic textures of the microstructures presented in figure 5. The orientation distribution functions were calculated by replacing each single orientation by a Gauss-type scattering functions using a scatter width of 3°. The textures are given in Euler space where each coordinate $\varphi_1, \phi, \varphi_2$ represents a certain crystal orientation. In order to emphasize the main texture components in Euler space, only areas with an orientation density above random ($f(g) = 1$) are plotted. The initial texture is characterized by a number of isolated components, some partial texture fibres, and some smeared-out components. During the annealing treatment most of the scattered components vanish and the main texture components are shifted.

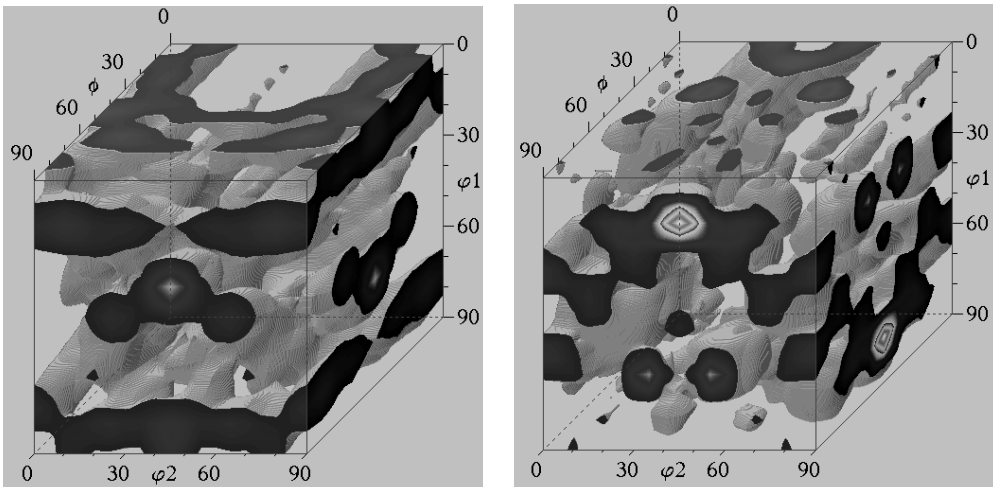

Figure 8. Starting (*a*) and end (*b*) texture of the microstructures shown in figure 5. The orientation distribution functions were calculated by using Gauss-type scattering functions with a scatter width of 3°. The textures are given in Euler space where each coordinate $\varphi_1, \phi, \varphi_2$ represents a certain crystal orientation. In order to emphasize the main texture components, the graphs show only areas in Euler space with an orientation density above random ($f(\boldsymbol{g}) = 1$).

6. Conclusions

We presented an approach for simulating recrystallization by coupling a viscoplastic crystal plasticity finite-element model with a cellular automaton. The coupling between both models consisted of: extracting and translating the microtexture and stored energy data predicted by the finite-element simulation into the cellular automaton model; mapping these data on the quadratic cellular automaton mesh; scaling the cellular automaton in terms of the derived cell size, maximum driving force, and maximum grain boundary mobility occurring in the region; and establishing an adequate nucleation criterion, which makes use of these data. The coupling method was used to simulate the formation of texture and microstructure in a deformed high-purity aluminium polycrystal during static primary recrystallization. It was observed that nucleation was concentrated in areas with a large accumulated shear and large lattice curvature. The spatial distribution of the nuclei was very inhomogeneous. Deformation bands with high stored energy and large curvature showed a high density of nuclei, whilst less deformed areas did not produce nuclei. The clustering of nuclei led to a deviation from Avrami–Johnson–Mehl-type kinetics with a 2D Avrami exponent significantly below two. The observed partial recovery of deformed material was explained in terms of insufficient misorientations between some of the deformed and the recrystallized areas, which entailed a local drop in grain boundary mobility. The initial texture after deformation was changed during the recrystallization treatment.

Acknowledgments

One of the authors (DR) gratefully acknowledges the financial support by the Deutsche Forschungsgemeinschaft through the Heisenberg programme. The authors are grateful to G Gottstein and L S Shvindlerman for stimulating discussions.

References

Abaqus Users' Manual 1994 Hibbitt, Karlsson and Sorensen, Pawtucket, RI

Asaro R J 1983 *Adv. Appl. Mech.* **23** 1–23

Becker R C 1991 *Acta Metall. Mater.* **39** 1211–30

——1998 *Hot Deformation of Aluminum Alloys* vol 2, ed T R Bieler, L A Lalli and S R MacEwen (TMS) pp 255–66

Becker R C, Butler J, Lalli L A and Hu W H 1991 *Metal. Trans.* A **22** 45–58

Becker R C and Panchanadeeswaran S 1995 *Acta Metall. Mater.* **43** 2701–19

Dawson P, Boyce D, MacEwen S and Rogge R *Proc. 12th Int. Conf. on Textures of Materials ICOTOM 12 (Montreal, Canada, August 9–13, 1999)* ed J A Szpunar (Ottawa: NRC Research Press) pp 505–10

Doherty R D, Hughes D A, Humphreys F J, Jonas J J, Juul Jensen D, Kassner M E, King W E, McNelly T R, McQueen H J and Rollett A D 1997 *Mater. Sci. Eng.* A **238** 219–74

Gottstein G 1984 Rekristallisation metallischer Werkstoffe (in German) *DGM Informationsgesellschaft* (Deutsche Gesellschaft für Metallkunde)

——1999 private communication

Gottstein G, Molodov D A and Shvindlerman L S 1998 *Interface Sci.* **6** 7–22

Gottstein G and Shvindlerman L S 1999 *Grain Boundary Migration in Metals—Thermodynamics, Kinetics, Applications* (Boca Raton, FL: CRC Press)

Gottstein G, Shvindlerman L S, Molodov D A and Czubayko U 1997 *Dynamics of Crystal Surfaces and Interfaces* ed P M Duxbury and T J Pence (New York: Plenum) pp 109–123

Haessner F 1978 *Recrystallization of Metallic Materials* (Dr Riederer)

Himmel L 1963 *Recovery and Recrystallization of Metals* (New York: Wiley)

Hu H 1963 *Recovery and Recrystallization of Metals* ed L Himmel (New York: Wiley) p 311

Humphreys J F 1992 *Mater. Sci. Technol.* **8** 135–44

——1997 *Acta Metall.* **45** 4231–53

Humphreys F J and Hatherly M 1995 *Recrystallization and Related Annealing Phenomena* (Oxford: Pergamon)

Juul Jensen D 1997 Orientation aspects of growth during recrystallization *Report* RISØ-R-978 (EN), Materials Research Department, RISØ National Laboratory.

Marx V, Raabe D, Engler O and Gottstein G 1997 *Proc. Symp. Computer Simulation and Modelling in Texture Research (Aachen, October 13–14, 1995)* (*Textures Microstruct.* **28** 211–18 (special edition)) (London: Gordon and Breach) series ed H-J Bunge, volume ed D Raabe and H-J Bunge

Marx V, Raabe D and Gottstein G 1995 Materials: microstructural and crystallographic aspects of recrystallization *Proc. 16th RISØ Int. Symp. on Material Science (RISØ National Laboratory, Roskilde, Denmark)* ed N Hansen, D Juul Jensen, Y L Liu, B Ralph, pp 461–6

Marx V, Reher F R and Gottstein G 1998 *Acta Mater.* **47** 1219–30

Maze Users Manual 1993 *LSTC Report* 1005, Livermore Software Technology Corporation, Livermore, CA

Molodov D A, Czubayko U, Gottstein G and Shvindlerman L S 1998 *Acta Mater.* **46** 553–64

Peirce D, Asaro R J and Needleman A 1983 *Acta Metall.* **31** 1951–76

Raabe D 1998a *Texture and Anisotropy of Polycrystals (Material Science Forum, vol 273–275)* ed R A Schwarzer (Trans Tech) pp 169–74

——1998b *Proc. 3rd Int. Conf. on Grain Growth in Polycrystalline Materials (Carnegie Mellon University, Pittsburgh, 1998)* ed H Weiland, B L Adams and A D Rollett pp 179–85

——1999 *Phil. Mag.* A **79** 2339–58

Reher F 1998 *PhD Dissertation* Rheinisch-Westfälische Technische Hochschule Aachen, Institut für Metallkunde und Metallphysik (in German)

Smelser R E and Becker R C 1989 (*Proc. Abaqus Users' Conf., Strasa, Italy)* (Providence RI: Hibbitt, Karlsson and Sorensen, Inc.) p 207

Smethells Metals Reference Book 1983 6 edn ed E A Brandles (London: Butterworths) p 15

Turnbull D 1951 *Trans. AIME* **191** 661–75

Available online at www.sciencedirect.com
SCIENCE DIRECT®
Computational Materials Science 34 (2005) 299–313
COMPUTATIONAL MATERIALS SCIENCE
www.elsevier.com/locate/commatsci

2D cellular automaton simulation of the recrystallization texture of an IF sheet steel under consideration of Zener pinning

Dierk Raabe [a,*], Luc Hantcherli [b]

[a] Max-Planck-Institut für Eisenforschung, Max-Planck-Strasse 1, 40237 Düsseldorf, Germany
[b] Ecole National Superieur des Mines de Saint-Etienne, 158 Cours Fauriel, 42023 Saint Etienne Cedex 2, France

Received 11 October 2004; received in revised form 25 November 2004; accepted 17 December 2004

Abstract

This is a 2D cellular automaton simulation study on the evolution of the recrystallization texture in a 75% cold rolled interstitial free (IF) sheet steel. The model is applied to experimentally obtained high resolution microtexture EBSD data. The simulation is discrete in time and physical space. Orientation is treated as a continuous variable in Euler space. The dislocation density distribution is approximated from the Kikuchi pattern quality of the experimental EBSD data. It is used for the calculation of the scalar driving force field required for the recrystallization simulation. Different models for nucleation and for the influence of Zener-type particle pinning are presented and tested. Real time and space calibration of the simulation is obtained by using experimental input data for the grain boundary mobility, the driving forces, and the length scale of the deformed microstructure as mapped by the high resolution EBSD experiments. The simulations predict the kinetics and the evolution of microstructure and texture during recrystallization. Depending on the ratio of the precipitated volume fraction and the average radius of the particles the simulations reveal three different regimes for the influence of particle pinning on the resulting microstructures, kinetics and crystallographic textures.

Keywords: Texture; Microtexture; Stored energy; Automotive; EBSD; Nucleation; Grain growth

1. Introduction

The understanding of the recrystallization texture of interstitial free (IF) low carbon steel sheets is important for an improved prediction of the resulting elastic-plastic anisotropy of such steels with respect to their engineering performance

* Corresponding author. Tel.: +49 211 6792278; fax: +49 211 6792333.
E-mail address: raabe@mpie.de (D. Raabe).

0927-0256/$ - see front matter © 2005 Elsevier B.V. All rights reserved.
doi:10.1016/j.commatsci.2004.12.067

during sheet forming in the automotive industry. The main goal in that context is to produce IF steel sheets with a very strong and homogeneous γ-fiber texture ($\{1\,1\,1\}\langle u\,v\,w\rangle$ texture) and a very small orientation density of the 45° ND-rotated cube orientation, $\{0\,0\,1\}\langle 1\,1\,0\rangle$ (ND refers to the sheet normal direction). The beneficial mechanical properties resulting from such textures, namely, a maximum planar Lankfort value together with a minimum variation of the Lankfort value in the sheet plane, define the goal for optimizing corresponding industry-scale continuous annealing procedures for IF steels for better sheet drawability [1–9].

An important microstructural parameter affecting the formation of recrystallization textures in IF steels is the influence of incoherent second phase precipitates which are located on the inherited grain boundaries of the deformed grains (e.g., aluminium-nitrides, titanium-carbides, titanium-sulfides, titanium-carbonitrides). In this study we use a modified 2D cellular automaton approach [10] for the simulation of primary static recrystallization of a cold rolled IF sheet steel (75% engineering thickness reduction). The proposed modification of the automaton consists in the possibility to consider the pinning effect associated with particles at the former grain boundaries according to the Zener or respectively Zener–Friedel models [11]. The automaton is used in a 2D rather than in the standard 3D formulation [10] since in the current study it is applied to experimental 2D EBSD data of the starting microstructure. The motivation for this simulation study is the frequent observation that new grains which grow during primary static recrystallization in such steels do not easily expand across the former grain boundaries of the deformed microstructure [9,12].

Our own TEM-observations have revealed the presence of fine particles (in particular of Ti(C,N)) at the inherited grain boundaries surrounding the deformed grains, so that one possible explanation for the impeded recrystallization may be a strong particle pinning effect (Fig. 1). The goal of this study, hence, is to investigate the influence of such fine grain boundary particles on the recrystallization microstructure and texture with the help of a modified cellular automaton approach.

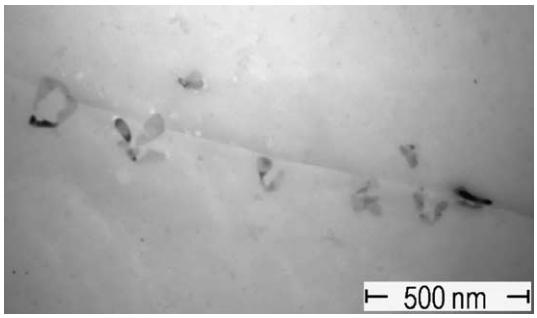

Fig. 1. TEM-carbon-replica of Ti(CN) precipitations on a grain boundary in an IF steel before recrystallization [unpublished results by I. Thomas, MPI].

2. Cellular automaton model

2.1. Basics of cellular automata for recrystallization modeling

Cellular automata are algorithms that describe the discrete spatial and temporal evolution of complex systems by applying local deterministic or probabilistic transformation rules to the cells of a regular (or non-regular) lattice [13–17]. These rules determine the state of a lattice point as a function of its previous state and the state of the neighboring sites. The number, arrangement, and range of the neighbor sites used by the transformation rule for calculating a state switch determines the range of the interaction and the local shape of the areas which evolve. Cellular automata work in discrete time steps. After each time interval the values of the state variables are updated for all lattice points in synchrony mapping the new (or unchanged) values assigned to them through the local transformation rule. Owing to these features, cellular automata provide a discrete method of simulating the evolution of complex dynamical systems which contain large numbers of similar components on the basis of their local interactions. The overall spatial system complexity and transformation kinetics emerge from the repeated and synchronous application of the cellular automaton rules equally to all nodes of the lattice. These local rules can for many cellular automaton models in materials science be derived through finite difference formulations of the underlying differential equa-

tions that govern the system dynamics at a mesoscopic level [15,16]. Cellular automata have been successfully used for a variety of problems in the field of recrystallization [15–30]. The model for the present recrystallization simulation is designed as a cellular automaton with a probabilistic transformation rule. The details of the used transformation rules are given in [10,16,26].

2.2. Particle pinning forces on grain boundaries

Grain boundary pinning forces arise when second phase particles occur on the grain boundary. Their presence reduces the grain boundary area and, hence, the grain boundary energy. This energy saving which must be replenished upon unpinning is referred to as Zener pinning [11,31]. In the following simulations we consider pinning effects imposed by a stable array of incoherent particles which reside on the grain boundaries of the deformed microstructure.

In his first calculation Zener [11] approximated the magnitude of the pinning force by assuming randomly distributed spherical particles. The boundary was assumed to move as a straight interface through the particle array and to experience a resistive force, F, from each particle. With γ the boundary energy (in units of J/m^2), the force F due to one particle is given by $F = \pi r\gamma$, where r is the particle radius. The surface A on which the force is applied amounts to $A = 2\pi r^2/(3f)$, where f is the volume fraction of spherical particles. The Zener pressure then amounts to

$$p_{\mathrm{Z}} = -\frac{3}{2}\gamma\frac{f}{r} \tag{1}$$

A shortcoming of this approach is that a grain boundary cannot be considered as a rigid interface, but it may have some flexible to bow out between particles when a driving force is applied. Diverse modifications have been proposed to correct for this flexibility [31–33]. They give results which are of the same order of magnitude as the original formulation of Zener. Two possible corrections were discussed by Hunderi and co-workers [34,35], p_{HZ}. They introduce a correction factor Φ which depends on the volume fraction of the particles f:

$$p_{\mathrm{HZ}} = -\Phi(f)\frac{3}{4}\gamma\frac{f}{r} \tag{2}$$

When assuming a Friedel-like particle behavior one obtains the following equation for the drag force, p_{FZ},

$$p_{\mathrm{FZ}} = -2.6\gamma\frac{f^{0.92}}{r} \tag{3}$$

When considering a stronger dependence of the corrector factor on the value of f than assumed in the original Friedel model [34–36], one obtains a modified expression for the Zener pressure:

$$p_{\mathrm{LFZ}} = -0.33\gamma\frac{f^{0.87}}{r} \quad \text{for } f < 3\% \tag{4}$$

For a reasonable choice of the grain boundary energy (0.6 J/m^2), the precipitate volume fraction (1%), and the average particle radius (1000 Å) the original Zener pinning force, as calculated according to Eq. (1) amounts to about 0.1 MPa. When considering the corrections discussed, the pinning force rises to about 0.5 MPa according to Eq. (3) and to 0.2 MPa according to Eq. (4). Eqs. (1) and (3) are hereafter used as constitutive laws for the simulations.

2.3. Implementation of Zener-type pinning effects into the cellular automaton

The introduction of a Zener-like pinning effect according to Eqs. (1) and (3) requires the definition of three new state variables in the recrystallization cellular automaton algorithm, namely, the grain boundary energy per area, the volume fraction of incoherent second phase particles, and the average particle size. The actual implementation of these quantities and the calculation of the resulting forces in a cellular automaton approach depends strongly on how the particles are modeled in the algorithm. Two different methods are conceivable to map particles on the inherited grain boundaries in a cellular automaton.

The first model defines a fixed volume fraction of particles as an attribute to each *cell* abutting an existing grain boundary. Since particles which are relevant for pinning effects are small compared to the cell size of the automaton they cannot be mapped in a one-to-one fashion occupying a

complete cell. A specific volume fraction of particles (and also a local value for the particle size) is, instead, associated with each cell abutting a grain boundary. This description has the advantage that it can smoothly enter into the standard automaton algorithm. The concept also allows one to start with a heterogeneous distribution of particles on the grain boundaries. The second model defines the volume fraction of particles as a generic grain boundary parameter and not as a cell variable. This means that the particle volume fraction and average radius is defined together with the type of grain boundary. In the following we use the second approach to map particles in the automaton mesh.

2.4. Criterion for recrystallization nucleation events

Primary static recrystallization proceeds by the formation and growth of nuclei [31]. In the present model the nucleation stage is not explicitly simulated since the automaton works above the subgrain scale. This means that the current automaton model with its rather large cell size cannot explicitly be used to model discontinuous subgrain coarsening phenomena which entail nucleation in IF steels. The transformation rule of the cellular automaton explained above considers only the growth stage. This means that a nucleation criterion must be added as a separate model. Such a nucleation rule determines how the incipient stage of recrystallization is seeded. A nucleation rule has to fulfill the kinetic and thermodynamic instability criteria. The kinetic instability criterion means that a successful nucleation event leads to the formation of a mobile large angle grain boundary (misorientation above 15°) that can sweep the surrounding deformed matrix. The thermodynamic instability criterion means that the stored energy changes across the newly formed large angle grain boundary creating a driving force that pushes it forward into the surrounding deformed matrix. The latter step is captured by the transformation rule of the cellular automaton as outlined above.

The nucleation rule chosen in this simulation study is based on site saturated nucleation conditions. At the beginning of the algorithm, the local values of the stored deformation energy (dislocation density) are for each cell checked and compared to some critical value. If the local value of the dislocation density is larger than that critical value, the cell is considered as spontaneously recrystallized without any orientation change [16,17]. In practice, this means for a cell that its orientation attributes (Euler angles) remain unchanged whereas the stored energy density parameter (dislocation density) drops to zero. With this step, the thermodynamic criterion is fulfilled. In the ensuing time step a so recrystallized cell can attempt to sweep a non-recrystallized neighbor cell according to the transformation rule, i.e., it is only successful if one of its boundary segments has sufficient mobility and a sufficiently large net driving force to move.

2.5. Grain boundary input parameters for the simulations

The IF steel investigated is characterized by 1810 K for the melting point; 2.480 Å for the Burgers vector at 300 K; $15 \times 10^{-6}\,\mathrm{K}^{-1}$ for the thermal dilatation coefficient; 69.2 GPa for the shear modulus at 300 K; 0.015 GPa/K for the thermal stiffness dilatation coefficient of the shear modulus; and a Poisson coefficient of 0.3. The grain boundary mobility data used for large angle interfaces in the current simulations are taken from experiments on Fe–Si specimens [37–39], namely, $97.48 \times 10^{-2}\,\mathrm{m}^3/\mathrm{N\,s}$ for the pre-exponential factor of the mobility and 3.9 eV for the energy of activation of the grain boundary mobility. These values are applied for large angle grain boundaries irrespective of their boundary plane normal. The dependence of the grain boundary mobility on the orientation difference of the neighboring grains as used in this study is given by

$$m(\theta) = \left[0.9\left(\frac{1}{1+\exp[(-2)\times(\theta-15)]}\right)\right] + 1 \quad (5)$$

For the grain boundary energy and its dependence on the misorientation angle we use the Read-Shockley approximation for angles below 15° [31]

$$\gamma = \gamma_{\mathrm{HAGB}}\frac{\theta}{\theta_{\mathrm{HAGB}}}\left(1 - \ln\left(\frac{\theta}{\theta_{\mathrm{HAGB}}}\right)\right) \quad (6)$$

where γ_{HAGB} is the high angle grain boundary specific energy, θ the misorientation angle and θ_{HAGB} is the transition limit to the high angle grain boundary regime which is described by a grain boundary energy of 0.79 J/m^2.

2.6. Stored energy input data for the simulations

Several authors have suggested approaches to estimate the stored deformation energy in rolled steel sheets from EBSD data. Choi et al. [40,41] have recently discussed three different methods. The first one uses the Kikuchi pattern quality of the EBSD data. The authors suggest, that this parameter can be related to the dislocations density. They assume that a high magnitude of the image quality corresponds to a small value of the stored deformation energy. The authors suggest that the stored energy for each cell, E_i, can be expressed as being proportional to the image quality distribution for each measured point, I_i, according to the relation

$$E_i \propto I_i = 10\left(1 - \frac{Q_i - Q_{min}}{Q_{max} - Q_{min}}\right) \tag{7}$$

where Q_i is the image quality at the measured point I, and Q_{max} and Q_{min} are the maximum and minimum values of the image quality at that point, respectively. The factor is chosen to obtain values between 0 and 10 MPa for the driving force. The dislocation density for each cell ρ_i can then be evaluated by using

$$\rho_i \propto \frac{2I_i}{Gb^2} = \frac{2 \times 10^7}{Gb^2}\left(1 - \frac{Q_i - Q_{min}}{Q_{max} - Q_{min}}\right) \tag{8}$$

where G is the shear modulus and b the Burgers vector. It is obvious though that this method is affected by experimental details such as specimen preparation and contamination effects.

The second method described in [40,41] uses the Taylor model. In this approach it is suggested that the stored deformation energy of each cell can be related to the Taylor factor, M_i, which is the sum of crystallographic shear for an imposed von Mises strain step. The authors discuss that cells which have a small Taylor factor correspond to areas with a high deformation potential, and thus to areas with a high stored deformation energy. In our view this evaluation method has two drawbacks: First, the method cannot properly capture the inhomogeneity of the deformation [42]. Second, the Taylor factor alone only gives an image of the current deformation state and does not consider the deformation history. It is clear, however, that the accumulation of the stored energy during a deformation path is determined not only by the *final* Taylor factor but by the path that the Taylor factor takes during grain rotation in the course of deformation.

The third method discussed by the authors [40,41] is based on the subgrain substructure. When assuming that the dislocation substructure can be simplified in form of circular subgrains of radius r and a subgrain boundary energy of γ, the stored energy is given by

$$S_i = \alpha\frac{\gamma}{2r} \tag{9}$$

where α is a geometric constant equal to 3.

For the simulations conducted in this study the dislocation density is evaluated with the help of the first method as described by Eqs. (7) and (8). In order to normalize the values provided by this approach a new factor is introduced in order to obtain a reference value for the maximum occurring dislocation density. This value can be determined with the help of the tensile stress according to the equation

$$R_m \approx \frac{1}{2}MGb\sqrt{\rho_{max}} \tag{10}$$

where R_m is the tensile strength, M the Taylor factor, G the shear modulus, b the Burgers vector, and ρ_{max} the corresponding reference value of the dislocation density. According to this method the maximum occurring dislocation density amounts to 4.7×10^{15} m^{-2}. The so determined distribution of the stored dislocation density in the starting microstructure is given in Fig. 2.

2.7. Processing details, mesh parameters, and simulated temperature

The cellular automaton model is applied to a Ti stabilized interstitial free (IF) steel sheet. The steel slab was after continuous casting reheated at about 1500 K in a walking beam furnace and

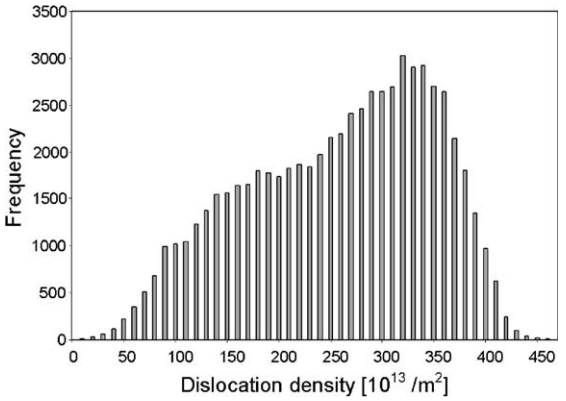

Fig. 2. Distribution of the evaluated dislocation density in the investigated area. The maximum occurring dislocation density is equal to 470×10^{13} m^{-2}.

subsequently hot-rolled completely in the austenitic range, i.e., above the A_{r3} temperature. The subsequent transformation to ferrite during cooling results in a homogeneous, nearly random crystallographic texture through the specimen thickness. The hot band thickness prior to cold rolling was 3 mm. After hot rolling the specimen was cold rolled to an engineering strain of 75% ($\varepsilon = \Delta d/d_0$, where Δd is the thickness reduction and d_0 the starting thickness). The heat treatment simulations were conducted under the assumption of isothermal conditions at a temperature of 1000 K. The cell size of the cellular automaton, λ_m, was chosen as 0.1 μm according to the step size of the underlying EBSD measurements.

2.8. Characterization of the starting microstructure (as cold-rolled)

EBSD measurements were carried out on the as cold rolled sample in longitudinal sections (Fig. 3). The cold rolling texture exhibits a strong α-fiber (texture components with a common crystallographic ⟨1 1 0⟩ axis parallel to the rolling direction) and a relatively weak γ-fiber (texture components with a common crystallographic ⟨1 1 1⟩ axis parallel to the sheet normal) [2,6,9]. In the cold rolled specimen used for the current simulations (Fig. 3) about 45% of the investigated area consists of α-fiber orientations (yellow), whereas only 25% can be assigned to the γ-fiber (green).

The maps reveal three different types of microstructure. Inside the α-fiber grains only a few subgrain boundaries appear, i.e., misorientations between neighboring EBSD points (point-to-point) are always below 2°, but the total accumulated orientation difference may continuously increase up to 7° over a distance of 5 μm (point-to-origin). In the γ-fiber areas, subgrain structures can be seen which are confined by low angle grain boundaries with misorientations between 2° and 15°.

In the γ-fiber grains a large frequency of subgrains with an average diameter of 1 μm is visible. These are in part surrounded by high angle grain boundaries. The dislocation density distribution as determined by using Eqs. (7) and (8) is clearly different for the two texture fibers. Deformation bands and γ-fiber areas are characterized by a high dislocation density. On the contrary, the α-fiber oriented regions reveal a smaller dislocation density. The measured area used for the simulations had a size of 40 μm × 13.6 μm (Fig. 4).

3. Simulation results and discussion

3.1. Simulation of primary recrystallization without Zener effect using different nucleation criteria

In order to identify reference microstructures for the simulations with particles we first conducted some calculations without including particle drag. The characteristic time step for these simulations, Δt, amounts to 0.54 s and the grid attack frequency, $\nu_0^{\min}$, to 1.85 s. The chosen sample area is mapped by using 400×136 automaton cells. Figs. 5–7 show simulated microstructures for three different site-saturated nucleation criteria (no particle pinning), Table 1.

The orientation map on the left-hand side of Figs. 5–7 is coded as orientation difference between the local orientation and the cube orientation ($\varphi_1 = 0°$, $\Phi = 0°$, $\varphi_2 = 0°$). The maps on the right-hand side show the stored dislocation density. Highest dislocation densities are colored in red. Blue regions have the lowest stored dislocation densities. The gray areas are recrystallized, i.e., they do not carry any further driving force.

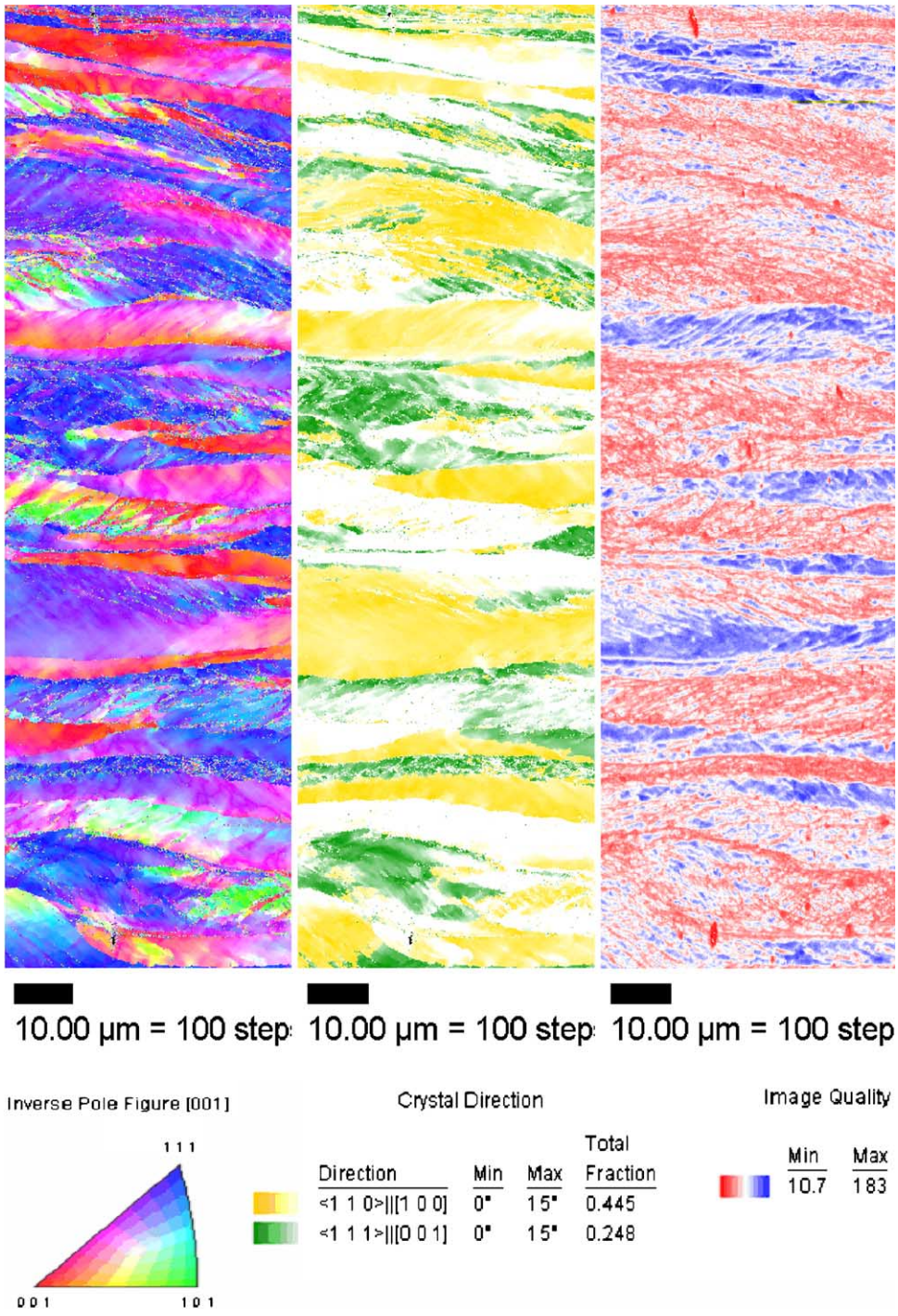

Fig. 3. EBSD measurements of a cold rolled IF steel sample: (a) inverse pole figure map with reference to the normal direction, (b) orientations close to the α-fiber (yellow) and to the γ-fiber (green) (including orientations with a maximum deviation of 15°), (c) image quality map which serves as a measure for the stored dislocation density (red = high, blue = low).

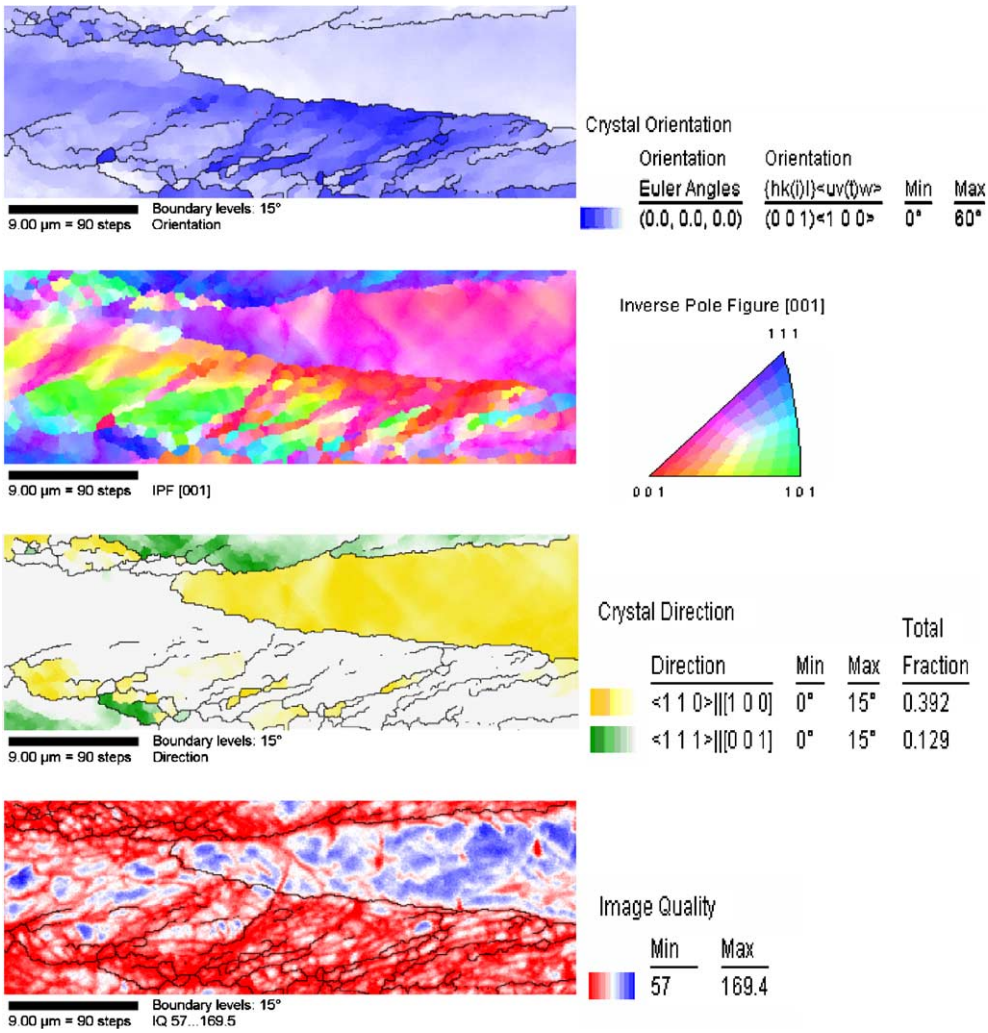

Fig. 4. EBSD measurements of the selected sample area: (a) crystal orientation using the cube orientation as a reference orientation, (b) inverse pole figure map in reference to the sheet normal direction, (c) α-fiber (yellow) and γ-fiber (green), (d) image quality as measure of the dislocation density (red = high, blue = low) according to Eqs. (7) and (8) (high angle grain boundaries are marked with thin black lines).

The black lines in both types of maps indicate large angle grain boundaries with misorientations above 15°.

The different maps, especially for nucleation criterion A (Table 1, Fig. 5), reveal that nucleation is particularly localized inside the deformation bands which are areas with high accumulated local dislocation densities. These highly deformed areas recrystallize with a grain size of about 1–2 μm. Less deformed areas exhibit a very small density of nuclei and are the last regions to be completely swept by recrystallization. Results obtained for nucleation criterion B also reveal strong nucleation clusters in areas with high dislocation densities (Table 1, Fig. 6). The average recrystallized grain size inside these clusters is between 2 and 3 μm. Cluster phenomena tend to disappear for higher threshold values, as shown exemplarily for nucleation criterion C, Table 1 (Fig. 7).

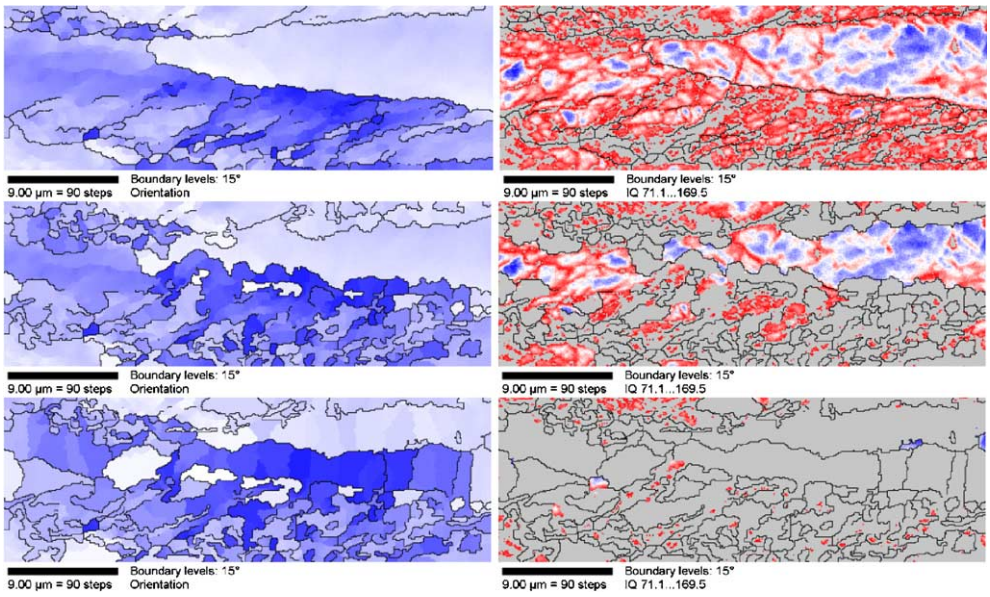

Fig. 5. Simulation results obtained for nucleation model A without particle drag (see Table 1). Recrystallization microstructures after 30, 65 and 99 vol.%. Left-hand side: crystal orientation using the cube orientation as reference. Right-hand side: dislocation density (red = high, blue = low) (high angle grain boundaries are marked with thin black lines); see color codes in Fig. 4.

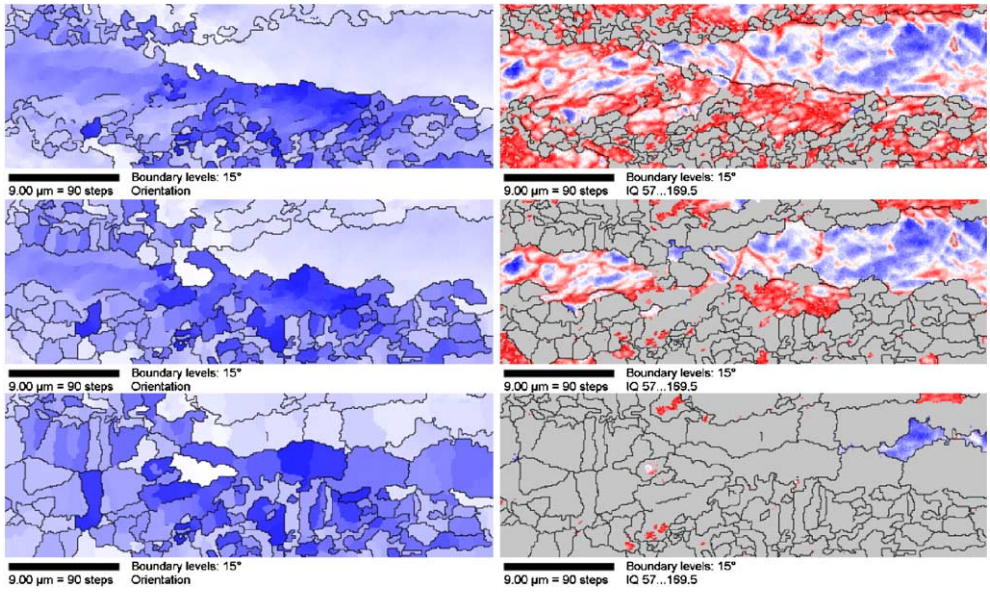

Fig. 6. Simulation results obtained for nucleation model B without particle drag (see Table 1). Recrystallization microstructures at 30, 65 and 99 vol.%. Left-hand side: crystal orientation using the cube orientation as reference. Right-hand side: dislocation density (red = high, blue = low) (high angle grain boundaries are marked with thin black lines); see color codes in Fig. 4.

It is an important topological result of these simulations that two kinds of nuclei can be observed. As prescribed by the model, nucleation takes place in areas with a large stored dislocation

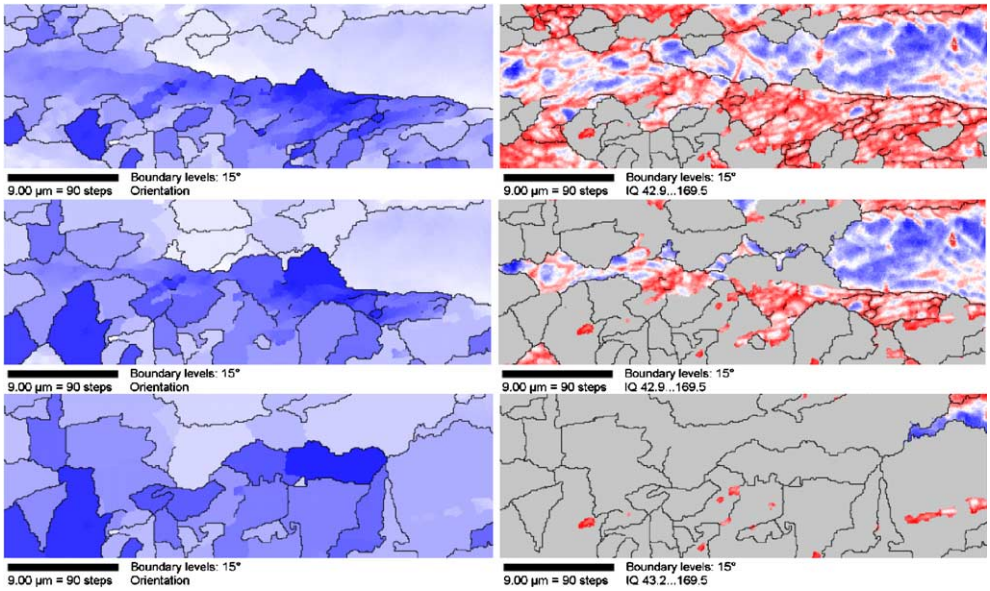

Fig. 7. Simulation results obtained for nucleation model C without particle drag (see Table 1). Recrystallization microstructures at 30, 65 and 99 vol.%. Left-hand side: crystal orientation using the cube orientation as reference. Right-hand side: dislocation density (red = high, blue = low) (high angle grain boundaries are marked with thin black lines); see color codes in Fig. 4.

Table 1
Conditions for spontaneous nucleation

Nucleation model	Nucleation criterion	Recrystallized volume fraction at $t = 0$ s
A (Fig. 5)	Cells with a dislocation density above 70% of the occurring maximum value undergo spontaneous recrystallization at $t = 0$ s (critical value: 329×10^{13} m^{-2})	~30% (16,451 cells)
B (Fig. 6)	Cells with a dislocation density above 80% of the occurring maximum value undergo spontaneous recrystallization at $t = 0$ s (critical value: 376×10^{13} m^{-2})	~10% (5272 cells)
C (Fig. 7)	Cells with a dislocation density above 90% of the occurring maximum value undergo spontaneous recrystallization at $t = 0$ s (critical value: 423×10^{13} m^{-2})	~0.5% (256 cells)

density above some critical threshold value. This means that the mechanical instability criterion which is a prerequisite for successful nucleation is automatically fulfilled for the spontaneously transformed cells, except for those which are themselves entirely surrounded by nuclei. Such cases represent trivial solutions of nucleation clustering. It occurs if a certain number of neighboring cells all fulfill independently at $t = 0$ s the condition of a critical dislocation density for nucleation (see values in Table 1).

However, according to the kinetic instability criterion which is included in the model in the form of the scaled mobility equation, spontaneously generated nuclei cannot grow if their grain boundary to the neighboring cell does not have sufficient mobility. Hence, the nuclei which are artificially formed at $t = 0$ s in the form of *potential nuclei* as described in Table 1 can only be considered as successful nuclei when the neighbor conditions described are met.

Numerous examples of such *potential nuclei* can be found inside less deformed areas, whereas the highest density of *successful nuclei,* which can freely expand after their spontaneous formation at the incipient stage of the simulation, are located

inside or close to in-grain deformation bands or in the vicinity of former grain boundaries. It is important to note that most *potential nuclei* which are formed at the beginning of recrystallization turn out to be also *successful* nuclei. This means that their neighbor cells are first, typically not themselves recrystallized (hence, sufficient local gradients in the dislocation density occur between neighbor cells) and second, that they form highly mobile large angle grain boundaries with their neighbor cells.

Another important observation is that the simulated specimen undergoes only partial recrystallization to about 99 vol.%. The corresponding mappings (Figs. 5–7) reveal two types of areas which remain unrecrystallized. The first type is indicated by the blue residual areas (indicating a small value of the stored dislocation density). These areas are mostly surrounded by large angle grain boundaries. This means that they could in principle be swept by expanding neighbor grains, but the driving forces are obviously so small that further progress of recrystallization is very slow compared to the characteristic grid attack frequency. This phenomenon can be referred to as thermodynamic decrease of the recrystallization tendency.

The second even more interesting type of unrecrystallized areas are some small red microstructure *islands* which have a sufficiently high driving force but which are surrounded by grain boundaries with a very small mobility. This phenomenon can be referred to as kinetic decrease of the recrystallization tendency. It is also referred to as *orientation pinning*. The red islands seems to be preferentially located in the deformation bands.

The kinetics of the recrystallization simulation can for the three simulations be analyzed in terms of the Avrami–Johnson–Mehl–Kolmogorov equation (JMAK) for statistical isotropic expansion of spheres,

$$X = 1 - \exp\left(-\left(\frac{t}{t_R}\right)^n\right) \tag{11}$$

where X is the recrystallized volume or area fraction, t the time, t_R the recrystallization (reference) time and n the Avrami coefficient. Site saturated 2D simulations of primary recrystallization have an Avrami coefficient equal to 2. Fig. 8 shows the results obtained from such kinetic analysis for the three different simulations. All show a substantial deviation from the typical JMAK-type growth kinetics. All curves exhibit a flattened shape when compared with the analytical equation. Also, all three simulations show Avrami coefficients below the theoretical 2D JMAK value of 2. The lower the dislocation density threshold value for nucleation is (Table 1), the larger is the deviation from the JMAK solution.

Several reasons are conceivable to explain this deviation: Firstly, nucleation is not homogeneous in the present case, but it is concentrated in areas with a large stored dislocation density. This means that the new nuclei impinge upon each other and compete at a very early stage of recrystallization unlike than in the JMAK model which makes a homogeneous assumption about the spatial

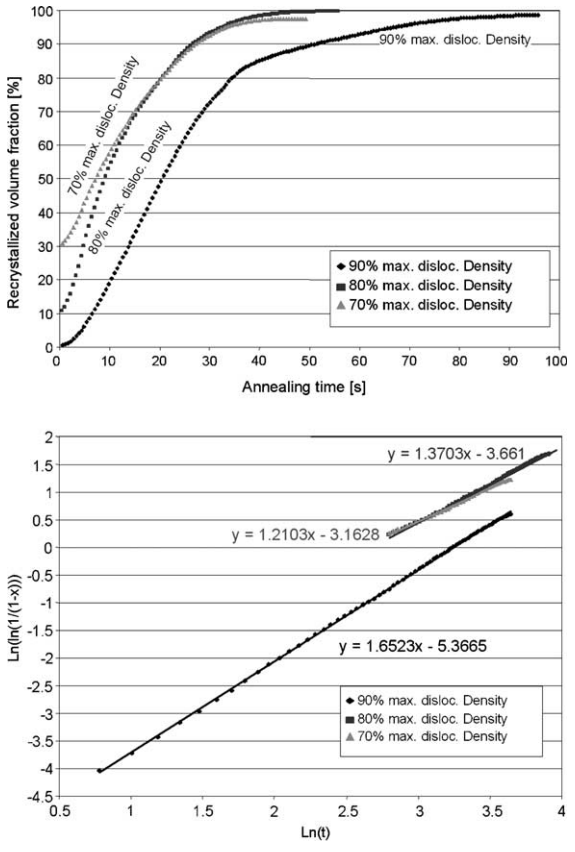

Fig. 8. Kinetics and Avrami coefficients of the recrystallization simulations shown in Figs. 5–7.

distribution of the nucleation sites. When the threshold value (dislocation density above which spontaneous nucleation occurs) becomes higher, nucleation clustering effects become more attenuated and recrystallization tends to follow the JMAK model. Secondly, the JMAK theory does not consider a heterogeneous distribution of the driving force and of the grain boundary mobility. The heterogeneous spectrum of these quantities as encountered in the starting configuration of the cellular automaton model will, on average, slow down the kinetics of recrystallization when compared to the JMAK owing to correlation effects. Finally, the discrete (cell) structure of the automaton algorithm also plays a role for the observed deviation. While the analytical model assumes a vanishing volume for freshly generated nuclei, the cellular automaton must assign at least one cell to each new nucleus. The predicted recrystallization time (around 50–100 s) is in good accord with the experimental values.

3.2. Simulation results of primary recrystallization considering Zener effects

The following simulations have been conducted using nucleation criterion B (80% of the maximum occurring dislocation density as a threshold value, see Table 1). Two models have been used for the implementation of particle pinning, namely, the classical Zener description, $p_r = -1.5\gamma f/r$ and a modified Zener model, $p_r = -2.6\gamma f^{0.92}/r$ (see details in Section 2). Since the particle radius is used as a constant (500 Å), simulations have been carried out with different magnitudes of the particle volume fraction.

The first step of the simulation study is to determine for which minimum value of the volume–particle radius ratio (f/r ratio) the recrystallization is stopped by the presence of particles. This ratio is identified by conducting an Avrami analysis for all simulations for different volume–radius ratios between 0 and 8 μm^{-1} (Fig. 9). Fig. 10 shows some selected simulated microstructures for different particle volume fractions.

According to the values of the f/r ratio, three different recrystallization regimes can be observed. The first regime can be identified for values below

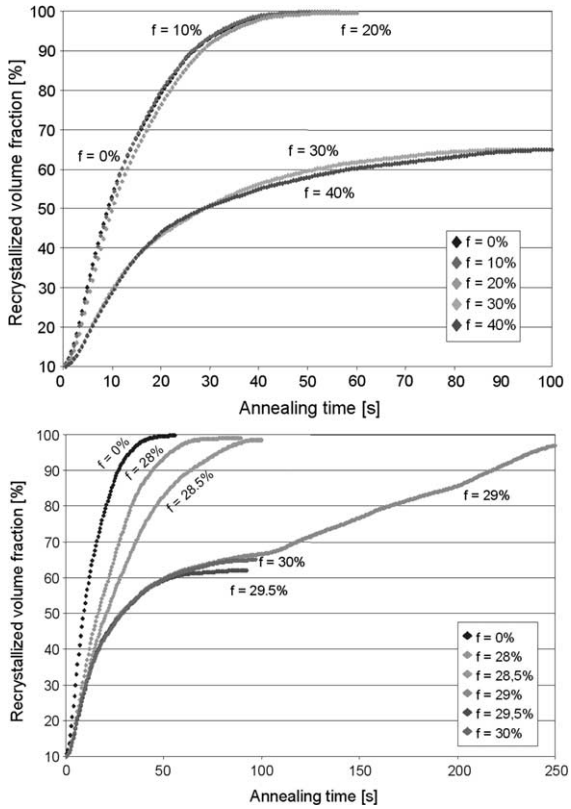

Fig. 9. Kinetics of recrystallization simulations with different particle volume fractions; classical Zener pinning assumed on the inherited grain boundaries.

5.7 μm^{-1}. In this range the sample recrystallizes completely. This means that the pinning forces exerted by the particles residing on the inherited grain boundaries are overcome by the local driving forces. When compared with the corresponding recrystallization simulations which were conducted without particle drag effects, the recrystallization observed in the current case is retarded but it is not suppressed.

The second regime can be identified for values larger than 5.9 μm^{-1}. In this case the primary recrystallization stops after sweeping about 65% of the sample volume. The final microstructure reveals a number of unrecrystallized regions.

The third regime can be identified for intermediate values between 5.7 and 5.9 μm^{-1}. In this range the recrystallization exhibits a transition regime. The occurrence of such a behavior is due to the

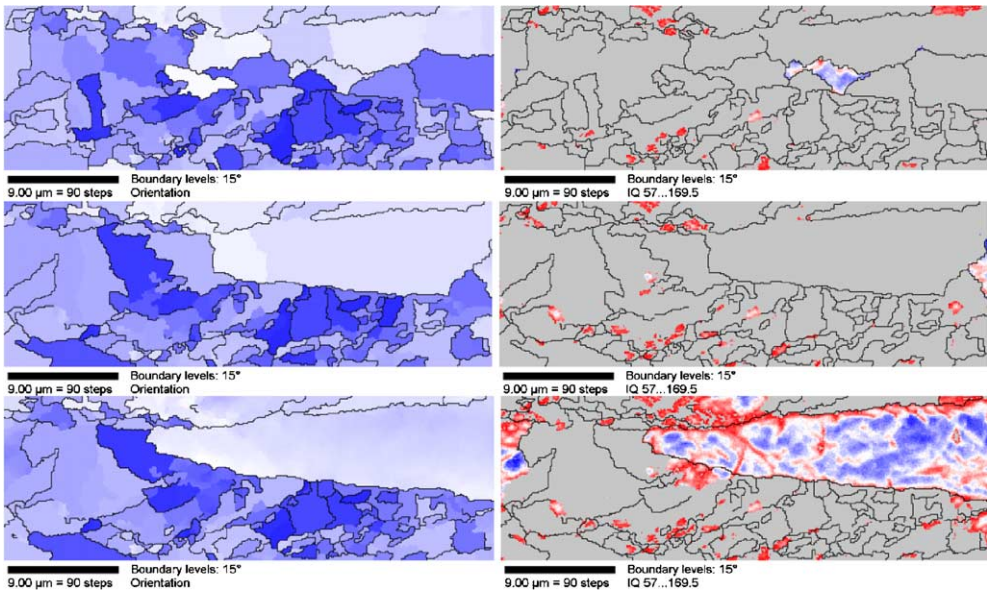

Fig. 10. Set of final simulated microstructures for different values of the precipitated volume fractions, f, of 28%, 29% and 30% (from top to bottom). The nucleation criterion was that all cells with a dislocation density above 80% of the occurring maximum value undergo spontaneous recrystallization at $t = 0$ s ($>376 \times 10^{13}$ m^{-2}) (see criterion B in Table 1); classical Zener pinning.

fact that most portions of the recrystallization front are successfully pinned by the particles. However, locally the particle pinning forces are overcome so that recrystallization expands rapidly further in those areas. This transition or two-stage recrystallization behavior could be termed *percolation recrystallization* regime. In such cases those local sites, where single grains can overcome the pinning force, assume the role of a nucleus which percolates across grain boundaries if the pinning forces are weak or the local driving force is very high. Since only a few such sites occur, the final grain sizes can become quite large in such cases. The transition regime occurs within a relatively sharp interval of the f/r values. This means that the driving forces occurring locally at the recrystallization front encounter particles which, on average, impose a drag force of almost the same magnitude. This average magnitude amounts to about 7 MPa for the present case, i.e., particle pinning forces must exceed this average value in order to completely suppress primary static recrystallization everywhere in the system.

Fig. 11 shows the evolution of the α- and γ-texture fibers during the simulated annealing treatment for different f/r ratios. The α-fiber is a typical cold rolling fiber for IF steels. It collects texture components with a common crystallographic ⟨1 1 0⟩ axis parallel to the rolling direction. The γ-fiber is a typical annealing fiber. It presents texture components with a common crystallographic ⟨1 1 1⟩ axis parallel to the sheet normal) [2,3].

The data show that for f/r ratios below 5.7 μm^{-1} the evolution of both, α-fiber and γ-fiber, is in good accord with the texture evolution typically observed for low-carbon steels, i.e., the γ-fiber increases and the components on the α-fiber decrease. A special feature of these simulations is the relatively late increase of the γ-fiber. Until a recrystallized volume fraction of 50% is reached, the γ-fiber orientations remain approximately constant at about 13 vol.%. After that it drops rapidly as a function of time.

For f/r ratios between 5.7 and 5.9 μm^{-1} the evolution of the α- and γ-fiber texture components is reversed at the beginning of recrystallization. With an increasing progress of recrystallization, however, the γ-fiber orientations become quite strong corresponding to a pronounced drop of the orientations on the α-fiber.

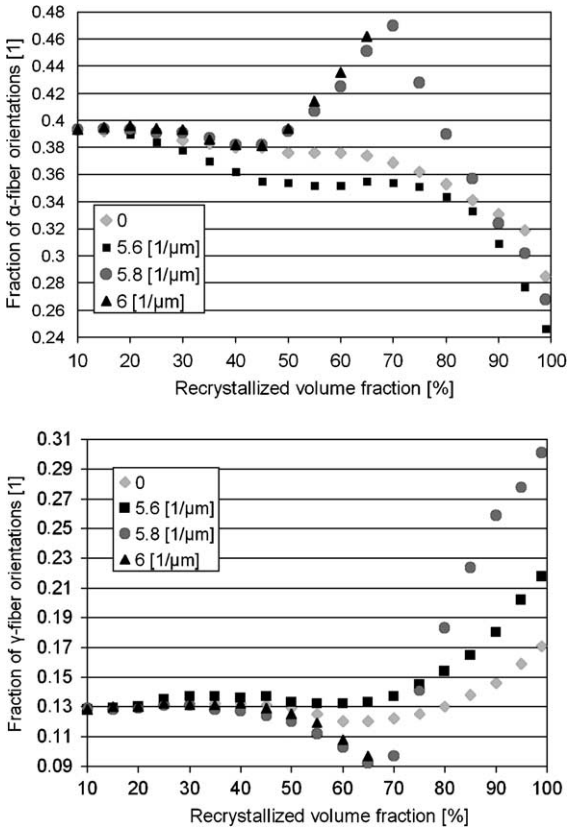

Fig. 11. Evolution of the α- and γ-fiber orientations during the simulated annealing under consideration of particle drag for different ratios of the volume fraction and particle radius, *f*/*r*.

For *f*/*r* ratios larger than 5.9 μm^{-1} the same reversed trend as found between 5.7 and 5.9 μm^{-1} is observed. However, no increase in the γ-fiber occurs before the recrystallization ceases to proceed. Consequently, after a recrystallized volume fraction of 50% the α-fiber still dominates the texture.

The results obtained for the predictions which were conducted by using the Zener–Friedel instead of the classical Zener model are very similar to the data shown above. When using the same starting configurations as for the Zener calculations, especially the same assumed particle radius of 0.05 μm, the transition regime occurs for a particle volume fraction between 14% and 15%. This is consistent with the analytical result for the critical volume fraction associated with the Friedel–Zener pinning force, f_{FZ}.

$$\frac{3}{2}\gamma\frac{f_Z}{r} = 2.6\gamma\frac{f_{FZ}^{0.92}}{r} \Longleftrightarrow f_{FZ} = \exp\left(\frac{\ln(0.58 f_Z)}{0.92}\right), \quad \text{i.e., } f_{FZ} \approx 0.141 \tag{12}$$

4. Conclusions

We used a cellular automaton model for the simulation of the recrystallization texture of an 80% cold rolled interstitial free (IF) steel with and without consideration of particles on the inherited grain boundaries. The model was applied to experimentally obtained high resolution EBSD data. Depending on the ratio of the precipitated volume fraction and the average radius of the particles, *f*/*r*, the simulations revealed three different regimes for the influence of particle pinning on the resulting microstructures, kinetics and textures. The first regime which occurred for small values of the *f*/*r* ratio on the former grain boundaries was characterized by complete, though retarded recrystallization. The second regime which occurred for intermediate values of the *f*/*r* ratio on the former grain boundaries was characterized by a partially suppressed progress of recrystallization. The third regime which occurred for large values of the *f*/*r* ratio on the former grain boundaries was characterized by a kinetic transition, i.e., most of the recrystallization front was successfully pinned by particles except for some small areas where recrystallization could percolate into neighboring grains. This regime, therefore, revealed a two-stage recrystallization behavior which was be referred to as percolation recrystallization.

References

[1] W.B. Hutchinson, Int. Mat. Rev. 29 (1984) 25.
[2] M. Hölscher, D. Raabe, K. Lücke, Steel Res. 62 (1991) 567.
[3] D. Raabe, K. Lücke, Scripta Metall. 27 (1992) 1533.
[4] C. Klinkenberg, D. Raabe, K. Lücke, Steel Res. 63 (1992) 227.
[5] D. Raabe, C. Klinkenberg, K. Lücke, Steel Res. 64 (1993) 262.
[6] P. Juntunen, D. Raabe, P. Karjalainen, T. Kopio, G. Bolle, Metall. Mater. Trans. A 32 (2001) 1989.

[7] D. Raabe, K. Lücke, Mater. Sci. Technol. 9 (1993) 302.
[8] D. Raabe, P. Klose, B. Engl, K.-P. Imlau, F. Friedel, F. Roters, Adv. Eng. Mater. 4 (2002) 169.
[9] I. Thomas, S. Zaefferer, F. Friedel, D. Raabe, Adv. Eng. Mater. 5 (2003) 566.
[10] D. Raabe, Phil. Mag. A 79 (1999) 2339.
[11] C. Zener, Private communication to C.S. Smith. Cited in Trans. Am. Inst. Min. Engrs 175 (1948) 15.
[12] D. Raabe, Steel Res. 66 (1995) 222.
[13] J. von Neumann, in: W. Aspray, A. Burks (Eds.), Papers of John Von Neumann on Computing and Computer Theory, Charles Babbage Institute Reprint Series for the History of Computing, vol. 12, MIT Press, Cambridge, MA, 1987.
[14] S. Wolfram, Theory and Applications of Cellular AutomataAdvanced Series on Complex Systems, selected papers 1983–1986, vol. 1, World Scientific, Singapore, 1986.
[15] D. Raabe, Computational Materials Science, Wiley-VCH, Weinheim, 1998.
[16] D. Raabe, Ann. Rev. Mater. Res. 32 (2002) 53.
[17] D. Raabe, F. Roters, F. Barlat, L.-Q. Chen (Eds.), Continuum Scale Simulation of Engineering Materials, WILEY-VCH, Weinheim, 2004.
[18] H.W. Hesselbarth, I.R. Göbel, Acta Metall. 39 (1991) 2135.
[19] C.E. Pezzee, D.C. Dunand, Acta Metall. 42 (1994) 1509.
[20] R.K. Sheldon, D.C. Dunand, Acta Mater. 44 (1996) 4571.
[21] C.H.J. Davies, Scripta Metall. Mater. 33 (1995) 1139.
[22] V. Marx, D. Raabe, O. Engler, G. Gottstein, Text. Microstruct. 28 (1997) 211.
[23] V. Marx, F.R. Reher, G. Gottstein, Acta Mater. 47 (1998) 1219.
[24] C.H.J. Davies, Scripta Mater. 36 (1997) 35.
[25] C.H.J. Davies, L. Hong, Scripta Mater. 40 (1999) 1145.
[26] D. Raabe, R. Becker, Model. Simul. Mater. Sci. Eng. 8 (2000) 445.
[27] D. Raabe, Comput. Mater. Sci. 19 (2000) 13.
[28] D. Raabe, F. Roters, V. Marx, Text. Microstruct. 26–27 (1996) 611.
[29] K.G.F. Janssens, Model. Simul. Mater. Sci. Eng. 11 (2003) 157.
[30] D. Raabe, Acta Mater. 52 (2004) 2653.
[31] F.J. Humphreys, M. Hatherly, Recrystallization and Related Annealing Phenomena, Pergamon, New York, 1995.
[32] R.D. Doherty, K. Li, K. Kershyup, A.D. Rollet, M.P. Anderson, in: J.B. Bilde-Sorensen et al. (Eds.), Materials Architecture, 10th Risø Symposium, Risø National Laboratory, Roskilde, Denmark, 1989, p. 31.
[33] R.D. Doherty, D.J. Srolovitz, A.D. Rollet, M.P. Anderson, Scripta Metal. 21 (1987) 675.
[34] E. Nes, E. Ryum, O. Hunderi, Acta Metall. 33 (1985) 11.
[35] O. Hunderi, E. Nes, N. Ryum, Acta Metall. 37 (1989) 129.
[36] N. Louat, Acta Metall. 30 (1982) 1291.
[37] M. Furtkamp, G. Gottstein, D.A. Molodov, V.N. Semenov, L.S. Shvindlerman, Acta Mater. 46 (1998) 4103.
[38] Y. Avramov, A. Gvozdev, Phys. Met. 36 (1973) 198.
[39] G. Gottstein, L.S. Shvindlerman, Grain Boundary Migration in Metals—Thermodynamics, Kinetics, Applications, CRC Press, Boca Raton, 1999.
[40] S.-H. Choi, Acta. Mater. 51 (2003) 1775.
[41] S.-H. Choi, Y.-S. Jin, Mater. Sci. Eng., A 371 (2004) 149.
[42] D. Raabe, M. Sachtleber, Z. Zhao, F. Roters, S. Zaefferer, Acta Mater. 49 (2001) 3433.

Annu. Rev. Mater. Res. 2002. 32:53–76
doi: 10.1146/annurev.matsci.32.090601.152855

CELLULAR AUTOMATA IN MATERIALS SCIENCE WITH PARTICULAR REFERENCE TO RECRYSTALLIZATION SIMULATION

Dierk Raabe
Max-Planck-Institut für Eisenforschung, Max-Planck-Str. 1, 40237 Düsseldorf, Germany, e-mail: raabe@mpie.de

Key Words integrated model, interface, transformation, nucleation, crystal plasticity

■ **Abstract** The paper is about cellular automaton models in materials science. It gives an introduction to the fundamentals of cellular automata and reviews applications, particularly for those that predict recrystallization phenomena. Cellular automata for recrystallization are typically discrete in time, physical space, and orientation space and often use quantities such as dislocation density and crystal orientation as state variables. Cellular automata can be defined on a regular or nonregular two- or three-dimensional lattice considering the first, second, and third neighbor shell for the calculation of the local driving forces. The kinetic transformation rules are usually formulated to map a linearized symmetric rate equation for sharp grain boundary segment motion. While deterministic cellular automata directly perform cell switches by sweeping the corresponding set of neighbor cells in accord with the underlying rate equation, probabilistic cellular automata calculate the switching probability of each lattice point and make the actual decision about a switching event by evaluating the local switching probability using a Monte Carlo step. Switches are in a cellular automaton algorithm generally performed as a function of the previous state of a lattice point and the state of the neighboring lattice points. The transformation rules can be scaled in terms of time and space using, for instance, the ratio of the local and the maximum possible grain boundary mobility, the local crystallographic texture, the ratio of the local and the maximum-occurring driving forces, or appropriate scaling measures derived from a real initial specimen. The cell state update in a cellular automaton is made in synchrony for all cells. The review deals, in particular, with the prediction of the kinetics, microstructure, and texture of recrystallization. Couplings between cellular automata and crystal plasticity finite element models are also discussed.

INTRODUCTION TO CELLULAR AUTOMATA

Basic Setup of Cellular Automata

Cellular automata are algorithms that describe the discrete spatial and temporal evolution of complex systems by applying local (or sometimes long-range)

deterministic or probabilistic transformation rules to the cells of a regular (or nonregular) lattice.

The space variable in cellular automata usually stands for real space, but orientation space, momentum space, or wave vector space can be used as well. Cellular automata can have arbitrary dimensions. Space is defined on a regular array of lattice points that can be regarded as the nodes of a finite difference field. The lattice maps the elementary system entities that are regarded as relevant to the model under investigation. The individual lattice points can represent continuum volume units, atomic particles, lattice defects, or colors depending on the underlying model. The state of each lattice point is characterized in terms of a set of generalized state variables. These could be dimensionless numbers, particle densities, lattice defect quantities, crystal orientation, particle velocity, blood pressure, animal species, or any other quantity the model requires. The actual values of these state variables are defined at each of the individual lattice points. Each point assumes one out of a finite set of possible discrete states. The opening state of the automaton, which can be derived from experiment (for instance from a microtexture experiment) or theory (for instance from crystal plasticity finite element simulations), is defined by mapping the initial distribution of the values of the chosen state variables onto the lattice.

The dynamical evolution of the automaton takes place through the application of deterministic or probabilistic transformation rules (also referred to as switching rules) that act on the state of each lattice point. These rules determine the state of a lattice point as a function of its previous state and the state of the neighboring sites. The number, arrangement, and range of the neighbor sites used by the transformation rule for calculating a state switch determine the range of the interaction and the local shape of the areas that evolve. Cellular automata work in discrete time steps. After each time interval, the values of the state variables are updated for all lattice points in synchrony, mapping the new (or unchanged) values assigned to them through the transformation rule.

Owing to these features, cellular automata provide a discrete method of simulating the evolution of complex dynamical systems that contain large numbers of similar components on the basis of their local (or long-range) interactions. Cellular automata do not have restrictions in the type of elementary entities or transformation rules employed. They can map such different situations as the distribution of the values of state variables in a simple finite difference simulation, the colors in a blending algorithm, the elements of fuzzy sets, or elementary growth and decay processes of cells. For instance, the Pascal triangle, which can be used to calculate higher-order binominal coefficients or the Fibonaccy numbers, can be regarded as a one-dimensional cellular automaton in which the value that is assigned to each site of a regular triangular lattice is calculated through the summation of the two numbers above it. In this case, the entities of the automaton are dimensionless integer numbers and the transformation rule is a summation.

Cellular automata were introduced by von Neumann (1) for the simulation of self-reproducing Turing automata and population evolution. In his early contributions, von Neumann denoted the automata as cellular spaces (1). Other authors used

notions like tessellation automata, homogeneous structures, tessellation structures, or iterative arrays. Later applications were mainly in the field of describing nonlinear dynamic behavior of fluids and reaction-diffusion systems. During the past decade, cellular automata have increasingly gained momentum for the simulation of microstructure evolution in the materials sciences.

Formal Description and Classes of Cellular Automata

The local interaction of neighboring lattice sites in a cellular automaton is specified through a set of transformation (switching) rules. Although von Neumann's original automata were designed with deterministic transformation rules, probabilistic transformations are conceivable as well. The value of an arbitrary state variable ξ assigned to a particular lattice site at a time $(t_0 + \Delta t)$ is determined by its present state (t_0) (or its last few states t_0, $t_0 - \Delta t$, etc.) and the state of its neighbors (1–4).

Considering the last two time steps for the evolution of a one-dimensional cellular automaton, this can be put formally by writing $\xi_j^{t_0+\Delta t} = f(\xi_{j-1}^{t_0-\Delta t}, \xi_j^{t_0-\Delta t}, \xi_{j+1}^{t_0-\Delta t}, \xi_{j-1}^{t_0}, \xi_j^{t_0}, \xi_{j+1}^{t_0})$, where $\xi_j^{t_0}$ indicates the value of the variable at a time t_0 at the node j. The positions $(j+1)$ and $(j-1)$ indicate the nodes in the immediate neighborhood of position j (for one dimension). The function f specifies the set of transformation rules, for instance such as provided by standard discrete finite difference algorithms.

If the state of the node depends only on its nearest neighbors (NN), the array is referred to as von Neumann neighboring (Figure 1*a*). If both the NN and the next-nearest neighbors (NNN) determine the ensuing state of the node, the array is called

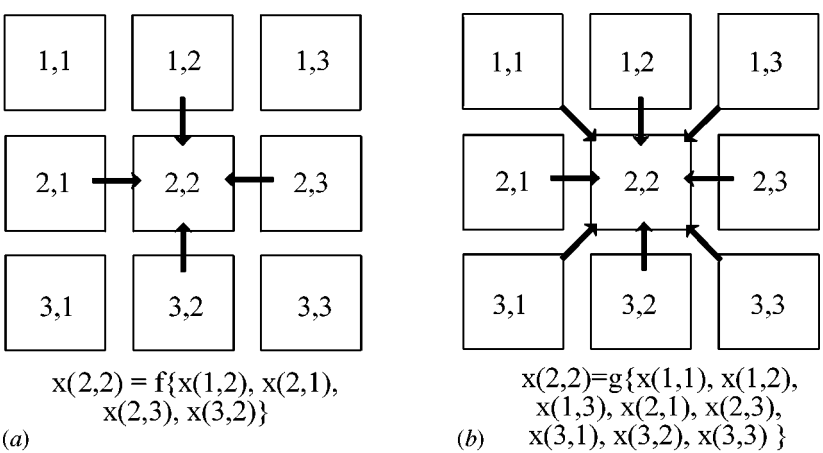

Figure 1 (*a*) Example of a two-dimensional von Neumann configuration considering nearest neighbors. (*b*) Example of a two-dimensional Moore configuration considering both nearest and next-nearest neighbors.

Moore neighboring (Figure 1*b*) (2). Owing to the discretization of space, the type of neighboring affects the local transformation rates and the evolving morphologies (1–4). For the Moore and other extended configurations, for which a certain medium-range interaction can be introduced among the sites, the transformation rule can in one dimension and for interaction with the last two time steps be rewritten as $\xi_j^{t_0+\Delta t} = f(\xi_{j-n}^{t_0-\Delta t}, \xi_{j-n+1}^{t_0-\Delta t}, \ldots, \xi_{j-1}^{t_0-\Delta t}, \xi_j^{t_0-\Delta t}, \xi_{j+1}^{t_0-\Delta t}, \xi_{j-1}^{t_0}, \xi_j^{t_0}, \xi_{j+1}^{t_0}, \ldots, \xi_{j+n-1}^{t_0}, \xi_{j+n}^{t_0})$, where n indicates the range of the transformation rule in units of lattice cells.

Even for very simple automata there exists an enormous variety of possible transformation rules. For instance, for a one-dimensional cellular automaton (Boolean, von Neumann neighboring), where each node can have one of two possible ground states, say $\xi_j = 1$ or $\xi_j = 0$, the transformation rule assumes the form $\xi_j^{t_0+\Delta t} = f(\xi_{j-1}^{t_0}, \xi_j^{t_0}, \xi_{j+1}^{t_0})$. This simple Boolean configuration defines 2^8 possible transformation rules. One of them has the form

$$
\begin{array}{llll}
\text{if } \left(\xi_{j-1}^{t_0}=1, \xi_j^{t_0}=1, \xi_{j+1}^{t_0}=1\right) & \text{then} & \xi_j^{t_0+\Delta t}=0 & (1,1,1)\rightarrow 0\\
\text{if } \left(\xi_{j-1}^{t_0}=1, \xi_j^{t_0}=1, \xi_{j+1}^{t_0}=0\right) & \text{then} & \xi_j^{t_0+\Delta t}=1 & (1,1,0)\rightarrow 1\\
\text{if } \left(\xi_{j-1}^{t_0}=1, \xi_j^{t_0}=0, \xi_{j+1}^{t_0}=1\right) & \text{then} & \xi_j^{t_0+\Delta t}=0 & (1,0,1)\rightarrow 0\\
\text{if } \left(\xi_{j-1}^{t_0}=1, \xi_j^{t_0}=0, \xi_{j+1}^{t_0}=0\right) & \text{then} & \xi_j^{t_0+\Delta t}=1 & (1,0,0)\rightarrow 1\\
\text{if } \left(\xi_{j-1}^{t_0}=0, \xi_j^{t_0}=1, \xi_{j+1}^{t_0}=1\right) & \text{then} & \xi_j^{t_0+\Delta t}=1 & (0,1,1)\rightarrow 1\\
\text{if } \left(\xi_{j-1}^{t_0}=0, \xi_j^{t_0}=1, \xi_{j+1}^{t_0}=0\right) & \text{then} & \xi_j^{t_0+\Delta t}=0 & (0,1,0)\rightarrow 0\\
\text{if } \left(\xi_{j-1}^{t_0}=0, \xi_j^{t_0}=0, \xi_{j+1}^{t_0}=1\right) & \text{then} & \xi_j^{t_0+\Delta t}=1 & (0,0,1)\rightarrow 1\\
\text{if } \left(\xi_{j-1}^{t_0}=0, \xi_j^{t_0}=0, \xi_{j+1}^{t_0}=0\right) & \text{then} & \xi_j^{t_0+\Delta t}=0 & (0,0,0)\rightarrow 0
\end{array}
$$

This particular transformation rule can be encoded by $(01011010)_2$, where the digits in brackets indicate the right-hand side of the table given above, and the ξ indicates the Boolean description. Its digital description is, of course, only valid for a given arrangement of the corresponding basis. This order is commonly chosen as a decimal row with decreasing value, i.e., (1, 1, 1) translates to 111 (one hundred eleven), (1, 1, 0) to 110 (one hundred ten), and so on. Transforming the binary code into decimal numbers using

2^7	2^6	2^5	2^4	2^3	2^2	2^1	2^0
0	1	0	1	1	0	1	0

leads to the decimal code number 90_{10}. The digital coding system is commonly used for compactly describing transformation rules for cellular automata in the literature (2–4).

In general terms the number of rules can be calculated by $k^{(kn)}$, where k is the number of states for the cell and n is the number of neighbors including the core cell. For a two-dimensional automaton with a Moore neighborhood and two possible

cell states (i.e., $k = 2$ and $n = 9$) $2^{29} = 262144$ different transformation rules exist.

If the state of a node is determined by the sum of the neighbor site values, the model is referred to as a totalistic cellular automaton. If the state of a node has a separate dependence on the state itself and on the sum of the values taken by the variables of the neighbors, the model is referred to as an outer totalistic cellular automaton (2–6).

Cellular automata fall into four basic classes of behavior (2–4) (for almost any initial configuration). Class 1 cellular automata evolve after a finite number of time steps to a homogeneous and unique state from which they do not evolve further. Cellular automata in this class exhibit the maximal possible order both at the global and local scale. The geometrical analogy for this class is a limit point in the corresponding phase space. Class 2 cellular automata usually create short period patterns that repeat periodically, typically either recurring after small periods or are stable. Local and global order exhibited is in such automata, although not maximal. Class 2 automata can be interpreted as filters that derive the essence from discrete data sets for a given set of transformation rules. In phase space such systems form a limit cycle. Class 3 cellular automata lead from almost all possible initial states to aperiodic chaotic patterns. The statistical properties of these patterns and the statistical properties of the starting patterns are almost identical at least after a sufficient period of time. The patterns created by class 3 automata are usually self-similar fractal arrays. After sufficiently many time steps, the statistical properties of these patterns are typically the same for almost all initial configurations. Geometrically, class 3 automata form so-called strange attractors in phase space. Class 3 is the most frequent type of cellular automata. With increasing size of the neighborhood and increasing number of possible cell states, the probability to design a class 3 automaton increases for an arbitrary selected rule. Cellular automata in this class can exhibit maximal disorder on both global and local scales. Class 4 cellular automata yield stable, periodic, and propagating structures that can persist over arbitrary lengths of time. Some class 4 automata dissolve after a finite number of steps of time, i.e., the state of all cells becomes zero. In some class 4 automata a small set of stable periodic figures can occur [such as for instance in Conway's "game of life" (5)]. By properly arranging these propagating structures, final states with any cycle length may be obtained. Class 4 automata show a high degree of irreversibility in their time development. They usually reveal more complex behavior and very long transient lengths, having no direct analogue in the field of dynamical systems. The cellular automata in this class can exhibit significant local (not global) order.

These introductory remarks show that the cellular automaton concept is defined in a very general and versatile way. Cellular automata can be regarded as a generalization of discrete calculation methods (1, 2). Their flexibility is due to the fact that, in addition to the use of crisp mathematical expressions as variables and discretized differential equations as transformation rules, automata can incorporate practically any kind of element or rule that is deemed relevant.

APPLICATION OF CELLULAR AUTOMATA IN MATERIALS SCIENCE

Transforming the abstract rules and properties of general cellular automata into a materials-related simulation concept consists of mapping the values of relevant state variables onto the points of a cellular automaton lattice and using the local finite difference formulations of the partial differential equations of the underlying model as local transformation rules. The particular versatility of the cellular automaton approach for microstructure simulations, particularly in the fields of recrystallization, grain growth, and phase transformation phenomena, is due to its flexibility in considering a large variety of state variables and transformation laws.

The design of such time and space discretized simulations of materials microstructures, which track kinetics and energies in a local fashion, are of interest for two reasons. First, from a fundamental standpoint, it is desirable to understand better the dynamics and the topology of microstructures that arise from the interaction of large numbers of lattice defects, which are characterized by a spectrum of intrinsic properties and interactions in spatially heterogeneous materials. For instance, in the fields of recrystallization and grain growth, the influence of local grain boundary characteristics (mobility, energy), local driving forces, and local crystallographic textures on the final microstructure is of particular interest. Second, from a practical point of view, it is desirable to predict microstructure parameters such as grain size or texture that determine the mechanical and physical properties of real materials subjected to industrial processes from a phenomenological, though sound, physical basis.

Apart from cellular automata, a number of excellent models for discretely simulating recrystallization and grain growth phenomena have been suggested. They can be grouped as multistate kinetic Potts Monte Carlo models, topological boundary dynamics and front-tracking models, and Ginzburg-Landau type phase field kinetic models [see overview in (6)]. However, compared with these approaches, the strength of scaleable kinetic cellular automata is such that they combine the computational simplicity and scalability of a switching model with the physical stringency of a boundary dynamics model. Their objective lies in providing a numerically efficient and at the same time phenomenologically sound method of discretely simulating recrystallization and grain growth phenomena. As far as computational aspects are concerned, cellular automata can be designed to minimize calculation time and reduce code complexity in terms of storage and algorithm. As far as microstructure physics is concerned, they can be designed to provide kinetics, texture, and microstructure on a real space and time scale on the basis of realistic or experimental input data for microtexture, grain boundary characteristics, and local driving forces. The possible incorporation of realistic values, particularly for grain boundary energies and mobilities, deserves particular attention because such experimental data are increasingly available, enabling one to make quantitative predictions.

Cellular automaton simulations are often carried out at an elementary level using atoms, clusters of atoms, dislocation segments, or small crystalline or continuum elements as underlying units. It should be emphasized in particular that those variants that discretize and map microstructure in continuum space are not intrinsically calibrated by a characteristic physical length or timescale. This means that a cellular automaton simulation of continuum systems requires the definition of elementary units and transformation rules that adequately reflect the system behavior at the level addressed. If some of the transformation rules refer to different real timescales (e.g., recrystallization and recovery, bulk diffusion and grain boundary diffusion) it is essential to achieve a correct common scaling of the entire system. The requirement for an adjustment of timescaling among various rules is due to the fact that the transformation behavior of a cellular automaton is sometimes determined by noncoupled Boolean routines rather than by the exact local solutions of coupled differential equations. The same is true when underlying differential equations with entirely different time scales enter the formulation of a set of transformation rules. The scaling problem becomes particularly important in the simulation of nonlinear systems (which applies for most microstructure-based cellular automata). During the simulation, it can be useful to refine or coarsen the scale according to the kinetics (time re-scaling) and spatial resolution (space re-scaling). Because the use of cellular automata is not confined to the microscopic regime, it provides a convenient numerical means for bridging various space and timescales in microstructure simulation.

Important fields where microstructure-based cellular automata have been successfully used in the materials sciences are primary static recrystallization and recovery (6–19), formation of dendritic grain structures in solidification processes (20–26), and related nucleation and coarsening phenomena (27–36). The following is devoted to the simulation of primary static recrystallization. For further study of related microstructural topics, the reader is referred to the references cited above.

EXAMPLE OF A RECRYSTALLIZATION SIMULATION BY USE OF A PROBABILISTIC CELLULAR AUTOMATON

Lattice Structure and Transformation Rule

The model for the present recrystallization simulation is designed as a cellular automaton with a probabilistic transformation rule (16–18). Independent variables are time t and space $\mathbf{x} = (x_1, x_2, x_3)$. Space is discretized into an array of equally shaped cells (two- or three-dimensional depending on input data). Each cell is characterized in terms of the dependent variables. These are scalar (mechanical, electromagnetic) and configurational (interfacial) contributions to the driving force and the crystal orientation $\mathbf{g} = \mathbf{g}(\varphi_1, \phi, \varphi_2)$, where $\mathbf{g}$ is the rotation matrix and φ_1, ϕ, φ_2 the Euler angles. The driving force is the negative change in Gibbs enthalpy G_t per transformed cell. The starting data, i.e., the crystal orientation map and the spatial distribution of the driving force, can be provided by experiment,

i.e., orientation imaging microscopy via electron back scatter diffraction, or by simulation, e.g., a crystal plasticity finite element simulation. Grains or subgrains are mapped as regions of identical crystal orientation, but the driving force may vary inside these areas.

The kinetics of the automaton result from changes in the state of the cells (cell switches). They occur in accord with a switching rule (transformation rule), which determines the individual switching probability of each cell as a function of its previous state and the state of its neighbor cells. The switching rule is designed to map the phenomenology of primary static recrystallization in a physically sound manner. It reflects that the state of a non-recrystallized cell belonging to a deformed grain may change owing to the expansion of a recrystallizing neighbor grain, which grows according to the local driving force and boundary mobility. If such an expanding grain sweeps a non-recrystallized cell, the stored dislocation energy of that cell drops to zero and a new orientation is assigned to it, namely that of the expanding neighbor grain. To put this formally, the switching rule is cast in a probabilistic form of a linearized symmetric rate equation, which describes grain boundary motion in terms of isotropic single-atom diffusion processes perpendicular through a homogeneous planar grain boundary segment under the influence of a decrease in Gibbs energy,

$$\dot{\mathbf{x}} = \mathbf{n}\nu_{\mathrm{D}}\lambda_{\mathrm{gb}}c\left\{\exp\left(-\frac{\Delta G + \Delta G_{\mathrm{t}}/2}{k_{\mathrm{B}}T}\right) - \exp\left(-\frac{\Delta G - \Delta G_{\mathrm{t}}/2}{k_{\mathrm{B}}T}\right)\right\}, \qquad 1.$$

where $\dot{\mathbf{x}}$ is the grain boundary velocity, ν_{D} the Debye frequency, λ_{gb} the jump width through the boundary, c the intrinsic concentration of grain boundary vacancies or shuffle sources, $\mathbf{n}$ the normal of the grain boundary segment, ΔG the Gibbs enthalpy of motion through the interface, ΔG_{t} the Gibbs enthalpy associated with the transformation, k_{B} the Boltzmann constant, and T the absolute temperature. Replacing the jump width by the Burgers vector and the Gibbs enthalpy terms by the total entropy, ΔS, and total enthalpy, ΔH, leads to a linearized form

$$\dot{\mathbf{x}} \approx \mathbf{n}\nu_{\mathrm{D}}\mathrm{b}\exp\left(-\frac{\Delta S}{k_{\mathrm{B}}}\right)\exp\left(-\frac{\Delta H}{k_{\mathrm{B}}T}\right)\left(\frac{pV}{k_{\mathrm{B}}T}\right), \qquad 2.$$

where p is the driving force and V the atomic volume, which is of the order of b^3 (b is the magnitude of the Burgers vector). Summarizing these terms reproduces Turnbull's rate expression

$$\dot{\mathbf{x}} = \mathbf{n}mp = \mathbf{n}m_0\exp\left(-\frac{Q_{\mathrm{gb}}}{k_{\mathrm{B}}T}\right)p, \qquad 3.$$

where m is the mobility. These equations provide a well-known kinetic picture of grain boundary segment motion, where the atomistic processes (including thermal fluctuations, i.e., random thermal backward and forward jumps) are statistically described in terms of the pre-exponential factor of the mobility $m_0 = m_0(\Delta\mathbf{g}, \mathbf{n})$ and of the activation energy of grain boundary mobility $Q_{\mathrm{gb}} = Q_{\mathrm{gb}}(\Delta\mathbf{g}, \mathbf{n})$.

For dealing with competing switches affecting the same cell, the deterministic rate equation can be replaced by a probabilistic analogue that allows one to calculate switching probabilities. For this purpose, Equation 3 is separated into a deterministic part, $\dot{\mathbf{x}}_0$, which depends weakly on temperature, and a probabilistic part, w, which depends strongly on temperature:

$$\dot{\mathbf{x}} = \dot{\mathbf{x}}_0 w = \mathbf{n}\frac{k_B T m_0}{V}\frac{pV}{k_B T}\exp\left(-\frac{Q_{gb}}{k_B T}\right) \quad \text{with} \quad \dot{\mathbf{x}}_0 = \mathbf{n}\frac{k_B T m_0}{V},$$

$$w = \frac{pV}{k_B T}\exp\left(-\frac{Q_{gb}}{k_B T}\right). \qquad 4.$$

The probability factor w represents the product of the linearized part $pV/(k_B T)$ and the non-linearized part $\exp[-Q_{gb}/(k_B T)]$ of the original Boltzmann terms. According to this expression, non-vanishing switching probabilities occur for cells that reveal neighbors with different orientation and a driving force that points in their direction. The automaton considers the first, second (two-dimensional), and third (three-dimensional) neighbor shell for the calculation of the total driving force acting on a cell. The local value of the switching probability depends on the crystallographic character of the boundary segment between such unlike cells.

Scaling and Normalization

Microstructure-based cellular automata are usually applied to starting data that have a spatial resolution far above the atomic scale. This means that the automaton lattice has a lateral scaling of $\lambda_m \gg b$, where λ_m is the scaling length of the cellular automaton lattice and b the Burgers vector. If a moving boundary segment sweeps a cell, the grain thus grows (or shrinks) by λ_m^3 rather than b^3. Because the net velocity of a boundary segment must be independent of this scaling value of λ_m, an increase in jump width must lead to a corresponding decrease in the grid attack frequency, i.e., to an increase of the characteristic time step and vice versa. For obtaining a scale-independent grain boundary velocity, the grid frequency must be chosen in a way to ensure that the attempted switch of a cell of length λ_m occurs with a frequency much below the atomic attack frequency, which attempts to switch a cell of length b. This scaling condition, which is prescribed by an external scaling length λ_m, leads to the equation

$$\dot{\mathbf{x}} = \dot{\mathbf{x}}_0 w = \mathbf{n}(\lambda_m \nu) w \quad \text{with} \quad \nu = \frac{k_B T m_0}{V \lambda_m}, \qquad 5.$$

where ν is the eigenfrequency of the chosen lattice characterized by the scaling length λ_m.

The eigenfrequency represents the attack frequency for one particular grain boundary with constant mobility. To use a whole spectrum of mobilities and driving forces in one simulation, it is necessary to normalize the eigenfrequency by a

common grid attack frequency ν_0, yielding

$$\dot{\mathbf{x}} = \dot{\mathbf{x}}_0 w = \mathbf{n}\lambda_\mathrm{m}\nu_0\left(\frac{\nu}{\nu_0}\right)w = \hat{\dot{\mathbf{x}}}_0\left(\frac{\nu}{\nu_0}\right)w = \hat{\dot{\mathbf{x}}}_0\hat{w}. \tag{6.}$$

The value of the attack frequency ν_0, which is characteristic of the lattice, can be calculated by the assumption that the maximum occurring switching probability cannot be larger than one;

$$\hat{w}^\mathrm{max} = \frac{m_0^\mathrm{max} p^\mathrm{max}}{\lambda_\mathrm{m}\nu_0^\mathrm{min}} \exp\left(-\frac{Q_\mathrm{gb}^\mathrm{min}}{k_\mathrm{B}T}\right) \stackrel{!}{\leq} 1, \tag{7.}$$

where m_0^max is the maximum occurring pre-exponential factor of the mobility, p^max the maximum possible driving force, ν_0^min the minimum allowed grid attack frequency, and $Q_\mathrm{gb}^\mathrm{min}$ the minimum occurring activation energy. With $\hat{w}^\mathrm{max} = 1$, one obtains the normalization frequency as a function of the upper bound input data.

$$\nu_0^\mathrm{min} = \frac{m_0^\mathrm{max} p^\mathrm{max}}{\lambda_\mathrm{m}} \exp\left(-\frac{Q_\mathrm{gb}^\mathrm{min}}{k_\mathrm{B}T}\right). \tag{8.}$$

This frequency and the local values of the mobility and the driving force lead to

$$\begin{aligned}\hat{w}^\mathrm{local} &= \frac{m_0^\mathrm{local} p^\mathrm{local}}{\lambda_\mathrm{m}\nu_0^\mathrm{min}} \exp\left(-\frac{Q_\mathrm{gb}^\mathrm{local}}{k_\mathrm{B}T}\right) \\ &= \left(\frac{m_0^\mathrm{local}}{m_0^\mathrm{max}}\right)\left(\frac{p^\mathrm{local}}{p^\mathrm{max}}\right) \exp\left(-\frac{\left(Q_\mathrm{gb}^\mathrm{local} - Q_\mathrm{gb}^\mathrm{min}\right)}{k_\mathrm{B}T}\right) = \left(\frac{m^\mathrm{local} p^\mathrm{local}}{m^\mathrm{max} p^\mathrm{max}}\right).\end{aligned} \tag{9.}$$

This expression is the central switching equation of the algorithm. One can interpret this equation also in terms of the local time $\mathrm{t} = \lambda_\mathrm{m}/\dot{\mathbf{x}}$, which is required by a grain boundary with velocity $\dot{\mathbf{x}}$ to sweep an automaton cell of size λ_m.

$$\hat{w}^\mathrm{local} = \left(\frac{m^\mathrm{local} p^\mathrm{local}}{m^\mathrm{max} p^\mathrm{max}}\right) = \left(\frac{\dot{x}^\mathrm{local}}{\dot{x}^\mathrm{max}}\right) = \left(\frac{t^\mathrm{max}}{t^\mathrm{local}}\right). \tag{10.}$$

Equation 9 shows that the local switching probability can be quantified by the ratio of the local and the maximum mobility $m^\mathrm{local}/m^\mathrm{max}$, which is a function of the grain boundary character and by the ratio of the local and the maximum driving pressure $p^\mathrm{local}/p^\mathrm{max}$. The probability of the fastest occurring boundary segment (characterized by $m_0^\mathrm{local} = m_0^\mathrm{max}$, $p^\mathrm{local} = p^\mathrm{max}$, $Q_\mathrm{gb}^\mathrm{local} = Q_\mathrm{gb}^\mathrm{min}$) to realize a cell switch is equal to 1.

Equation 9 shows that an increasing cell size does not influence the switching probability but only the time step elapsing during an attempted switch. This relationship is obvious since the volume to be swept becomes larger, which requires more time. The characteristic time constant of the simulation Δt is $1/\nu_0^\mathrm{min}$.

Although Equation 9 allows one to calculate the switching probability of a cell as a function of its previous state and the state of the neighbor cells, the actual decision about a cell switch is made by a Monte Carlo step. The use of random numbers ensures that all cell switches are sampled according to their proper statistical weight, i.e., according to the local driving force and mobility between cells. The simulation proceeds by calculating the individual local switching probabilities $\hat{w}^{\text{local}}$ for each cell and evaluating them using a Monte Carlo algorithm. This means that for each cell the calculated switching probability is compared with a randomly generated number r, which lies between 0 and 1. The switch is accepted if the random number is equal or smaller than the calculated switching probability. Otherwise the switch is rejected.

$$\text{Random number } r \text{ between 0 and 1} \begin{cases} \text{accept switch if } \mathrm{r} \leq \left(\dfrac{m^{\text{local}} p^{\text{local}}}{m^{\max} p^{\max}} \right) \\ \text{reject switch if } \mathrm{r} > \left(\dfrac{m^{\text{local}} p^{\text{local}}}{m^{\max} p^{\max}} \right) \end{cases} . \quad 11.$$

Except for the probabilistic evaluation of the analytically calculated transformation probabilities, the approach is entirely deterministic. Thermal fluctuations other than already included via Turnbull's rate equation are not permitted. The use of realistic or even experimental input data for the grain boundaries enables one to make predictions on a real time and space scale. The switching rule is scalable to any mesh size and to any spectrum of boundary mobility and driving force data. The state update of all cells is made in synchrony.

Simulation of Primary Static Recrystallization and Comparison to Avrami-Type Kinetics

Figure 2 shows the kinetics and three-dimensional microstructures of a recrystallizing aluminum single crystal. The initial deformed crystal had a uniform Goss orientation (011)[100] and a dislocation density of $10^{15}\,\mathrm{m}^{-2}$. The driving force was from the stored elastic energy provided by the dislocations. In order to compare the predictions with analytical Avrami kinetics, recovery and driving forces arising from local boundary curvature were not considered. The simulation used site saturated nucleation conditions, i.e., the nuclei at $t = 0$ s were statistically distributed in physical space and orientation space. The grid size was $10 \times 10 \times 10\ \mu\mathrm{m}^3$. The cell size was 0.1 μm. All grain boundaries had the same mobility using an activation energy of the grain boundary mobility of 1.3 eV and a pre-exponential factor of the boundary mobility of $m_0 = 6.2 \cdot 10^{-6}\,\mathrm{m}^3/(\mathrm{N{\cdot}s})$ (37). Small angle grain boundaries had a mobility of zero. The temperature was 800 K. The time constant of the simulation was 0.35 s.

Figure 3 shows the kinetics for a number of three-dimensional recrystallization simulations with site-saturated nucleation conditions and identical mobility for all grain boundaries. The different curves correspond to different initial numbers

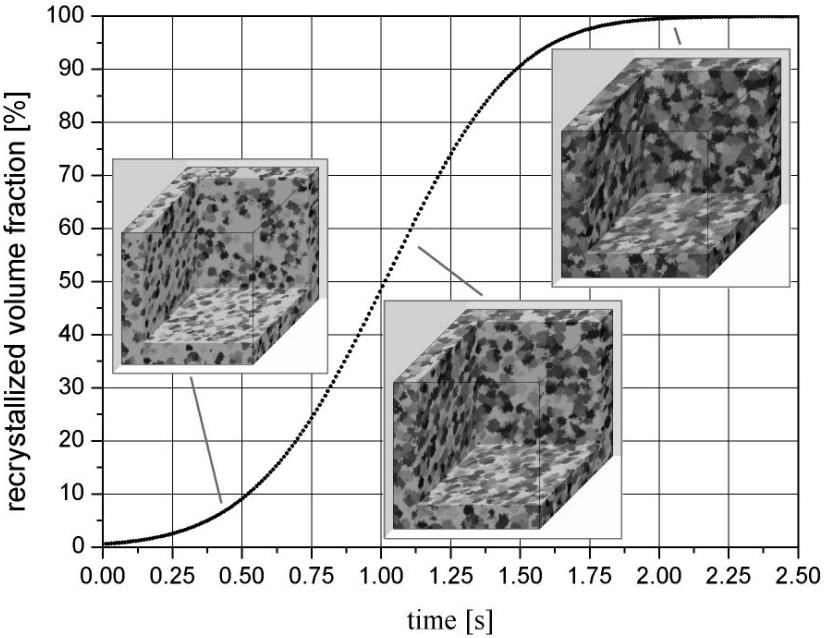

Figure 2 Kinetics and microstructure of recrystallization in a plastically strained aluminum single crystal. The deformed crystal had a uniform (011)[100] orientation and a uniform dislocation density of 10^{15} m^{-2}. Simulation parameter: site-saturated nucleation; lattice size, $10 \times 10 \times 10$ μm^3; cell size, 0.1 μm; activation energy of large-angle grain boundary mobility, 1.3 eV; pre-exponential factor of large-angle boundary mobility, $m_0 = 6.2 \cdot 10^{-6}$ m^3/(N $\cdot$ s); temperature, 800 K; time constant 0.35 s.

of nuclei. The initial number of nuclei varied between 9624 (pseudo-nucleation energy of 3.2 eV) and 165 (pseudo-nucleation energy of 6.0 eV). The curves (Figure 3*a*) all show a typical Avrami shape, and the logarithmic plots (Figure 3*b*) reveal Avrami exponents between 2.86 and 3.13, which is in good accord with the analytical value of 3.0 for site-saturated conditions. The simulations with a very high initial density of nuclei reveal a more pronounced deviation of the Avrami exponent with values around 2.7 during the beginning of recrystallization. This deviation from the analytical behavior is due to lattice effects: While the analytical derivation assumes a vanishing volume for newly formed nuclei, the cellular automaton has to assign one lattice point to each new nucleus.

Figure 4 shows the effect of grain boundary mobility on growth selection. Whereas in Figure 4*a* all boundaries have the same mobility, in Figure 4*b* one grain boundary has a larger mobility than the others (activation energy of the mobility of 1.35 eV instead of 1.40 eV) and consequently grew much faster than the neighboring grains that finally ceased to grow. The grains in this simulation all grew into a heavily deformed single crystal.

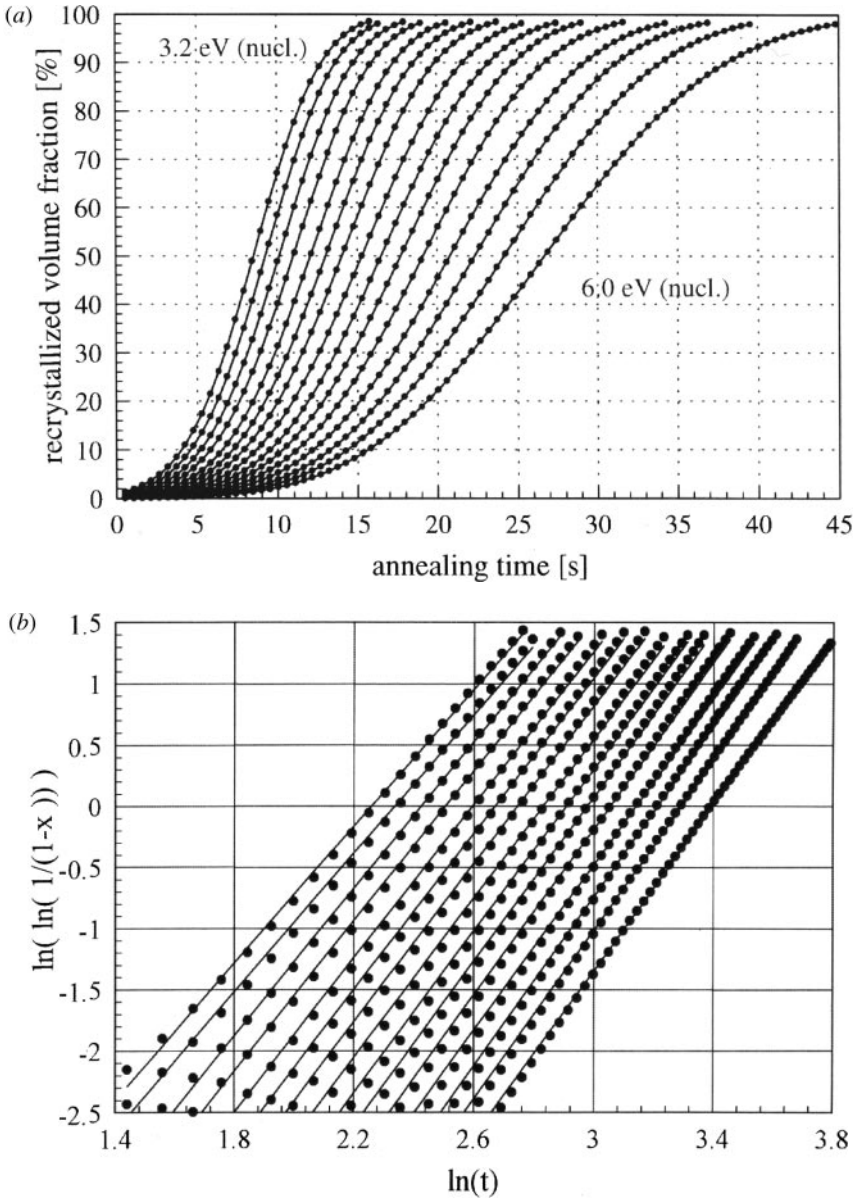

Figure 3 Kinetics for various three-dimensional recrystallization simulations with site-saturated nucleation conditions and identical mobility for all grain boundaries. The different curves correspond to different initial numbers of nuclei. The initial number of nuclei varied between 9624 (pseudo-nucleation energy of 3.2 eV) and 165 (pseudo-nucleation energy of 6.0 eV). (*a*) Avrami diagrams, (*b*) logarithmic diagrams showing Avrami exponents between 2.86 and 3.13.

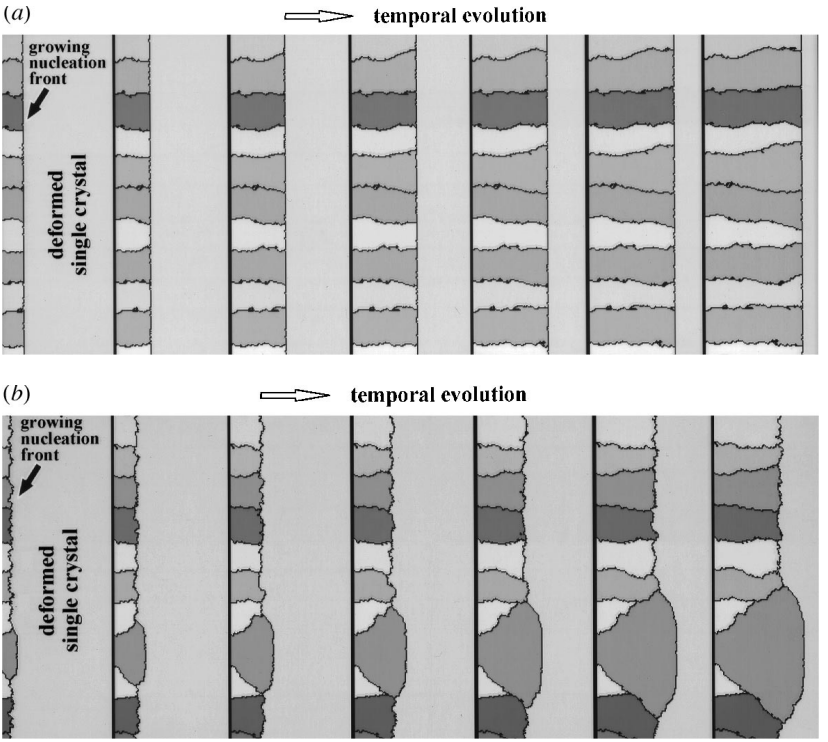

Figure 4 Effect of grain boundary mobility on growth selection. All grains grow into a deformed single crystal. (*a*) All grain boundaries have the same mobility. (*b*) One grain boundary has a larger mobility than the others (activation energy of the mobility of 1.35 eV instead of 1.40 eV) and grows faster than the neighboring grains.

Examples of Coupling Cellular Automata with Crystal Plasticity Finite Element Models for Predicting Recrystallization

Simulation approaches such as the crystal plasticity finite element method or cellular automata are increasingly gaining momentum as tools for spatial and temporal discrete prediction methods for microstructures and textures. The major advantage of such approaches is that they consider material heterogeneity as opposed to classical statistical approaches, which are based on the assumption of material homogeneity.

Although the average behavior of materials during deformation and heat treatment can sometimes be sufficiently well described without considering local effects, prominent examples exist where substantial progress in understanding and tailoring material response can only be attained by taking material heterogeneity into account. For instance, in the field of plasticity, the quantitative investigation of ridging and roping or related surface defects observed in sheet metals requires

knowledge about local effects such as the grain topology or the form and location of second phases. In the field of heat treatment, the origin of the Goss texture in transformer steels, the incipient stages of cube texture formation during primary recrystallization of aluminum, the reduction of the grain size in microalloyed low carbon steel sheets, and the development of strong $\{111\}\langle uvw\rangle$ textures in steels can hardly be predicted without incorporating local effects such as the orientation and location of recrystallization nuclei and the character and properties of the grain boundaries surrounding them.

Although spatially discrete microstructure simulations have already profoundly enhanced our understanding of microstructure and texture evolution over the past decade, their potential is sometimes simply limited by an insufficient knowledge about the external boundary conditions that characterize the process and an insufficient knowledge about the internal starting conditions, which are, to a large extent, inherited from the preceding process steps. It is thus an important goal to improve the incorporation of both types of information into such simulations. External boundary conditions prescribed by real industrial processes are often spatially non-homogeneous. They can be investigated using experiments or process simulations that consider spatial resolution. Spatial heterogeneities in the internal starting conditions, i.e., in the microstructure and texture, can be obtained from experiments or microstructure simulations that include spatial resolution.

Coupling, Scaling, and Boundary Conditions

In the present example, the results obtained from a crystal plasticity finite element simulation were used to map a starting microstructure for a subsequent discrete recrystallization simulation carried out with a probabilistic cellular automaton. The finite element model was used to simulate a plane strain compression test conducted on aluminum with columnar grain structure to a total logarithmic strain of $\varepsilon = -0.434$. Details about the finite element model are given elsewhere (17, 18, 38, 39). The values of the state variables (dislocation density, crystal orientation) given at the integration points of the finite element mesh were mapped on the regular lattice of a two-dimensional cellular automaton. Whereas the original finite element mesh consisted of 36977 quadrilateral elements, the cellular automaton lattice consisted of 217600 discrete points. The values of the state variables at each of the integration points were assigned to the new cellular automaton lattice points, which fell within the Wigner-Seitz cell corresponding to that integration point. The Wigner-Seitz cells of the finite element mesh were constructed from cell walls that were the perpendicular and bisected planes of all lines connecting neighboring integration points, i.e., the integration points were in the centers of the Wigner-Seitz cells.

In the present example, the original size of the specimen providing the input microstructure to the crystal plasticity finite element simulations gave a lattice point spacing of $\lambda_m = 61.9\ \mu$m. The maximum driving force in the region arising from the stored dislocation density amounted to about 1 MPa. The temperature dependence of the shear modulus and of the Burgers vector was considered in the calculation of the driving force. The grain boundary mobility in the region was characterized by an activation energy of the grain boundary mobility of 1.46 eV and a

pre-exponential factor of the grain boundary mobility of $m_0 = 8.3 \times 10^{-3}\,m^3/(N\,s)$. Together with the scaling length $\lambda_m = 61.9\ \mu m$, these data were used for the calculation of the timestep $\Delta t = 1/\nu_0^{min}$ and of the local switching probabilities $\hat{w}^{local}$. The annealing temperature was 800 K. Large-angle grain boundaries were characterized by an activation energy for the mobility of 1.3 eV. Small-angle grain boundaries were assumed to be immobile.

Nucleation Criterion

The nucleation process during primary static recrystallization has been explained for pure aluminum in terms of discontinuous subgrain growth (40). According to this model, nucleation takes place in areas that reveal high misorientations among neighboring subgrains and a high local driving force for curvature driven discontinuous subgrain coarsening. The present simulation approach works above the subgrain scale, i.e., it does not explicitly describe cell walls and subgrain coarsening phenomena. Instead, it incorporates nucleation on a more phenomenological basis using the kinetic and thermodynamic instability criteria known from classical recrystallization theory (see, e.g., 40).

The kinetic instability criterion means that a successful nucleation process leads to the formation of a mobile large-angle grain boundary that can sweep the surrounding deformed matrix. The thermodynamic instability criterion means that the stored energy changes across the newly formed large-angle grain boundary providing a net driving force that pushes it forward into the deformed matter. Nucleation in this simulation is performed in accord with these two aspects: Potential nucleation sites must fulfill both the kinetic and the thermodynamic instability criteria.

This nucleation model does not create any new orientations: At the beginning of the simulation, the thermodynamic criterion (the local value of the dislocation density) was first checked for all lattice points. If the dislocation density was larger than some critical value of its maximum value in the sample, the cell was spontaneously recrystallized without any orientation change, i.e., a dislocation density of zero was assigned to it, and the original crystal orientation was preserved. In the next step, the ordinary growth algorithm was employed according to Equations 1–11, i.e., the kinetic conditions for nucleation were checked by calculating the misorientations among all spontaneously recrystallized cells (preserving their original crystal orientation) and their immediate neighborhood considering the first, second, and third neighbor shell. If any such pair of cells revealed a misorientation above 15°, the cell flip of the unrecrystallized cell was calculated according to its actual transformation probability, Equation 9. In case of a successful cell flip, the orientation of the first recrystallized neighbor cell was assigned to the flipped cell.

Predictions and Interpretation

Figures 5–7 show simulated microstructures for site-saturated spontaneous nucleation in all cells with a dislocation density larger than 50% of the maximum value (in Figure 5), larger than 60% of the maximum value (in Figure 6),

and larger than 70% of the maximum value (in Figure 7). Each figure shows a set of four subsequent microstructures during recrystallization.

The upper graphs in Figures 5–7 show the evolution of the stored dislocation densities. The gray areas are recrystallized, i.e., the stored dislocation content of the affected cells was dropped to zero. The lower graphs represent the microtexture images where each color represents a specific crystal orientation. The color level is determined as the magnitude of the Rodriguez orientation vector using the cube component as reference. The fat white lines in both types of figures indicate grain boundaries with misorientations above 15° irrespective of the rotation axis. The thin green lines indicate misorientations between 5° and 15° irrespective of the rotation axis.

The incipient stages of recrystallization in Figure 5 (cells with 50% of the maximum occurring dislocation density undergoing spontaneous nucleation without orientation change) reveal that nucleation is concentrated in areas with large accumulated local dislocation densities. As a consequence, the nuclei form clusters of similarly oriented new grains (e.g., Figure 5*a*). Less deformed areas between the bands reveal a very small density of nuclei. Logically, the subsequent stages of recrystallization (Figure 5*b–d*) reveal that the nuclei do not sweep the surrounding deformation structure freely as described by Avrami-Johnson-Mehl theory but impinge upon each other and thus compete at an early stage of recrystallization.

Figure 6 (using 60% of the maximum occurring dislocation density as threshold for spontaneous nucleation) also reveals strong nucleation clusters in areas with high dislocation densities. Owing to the higher threshold value for a spontaneous cell flip, nucleation outside of the deformation bands occurs vary rarely. Similar observations hold for Figure 7 (70% threshold value). It also shows an increasing grain size as a consequence of the reduced nucleation density.

The deviation from Avrami-Johnson-Mehl type growth, i.e., the early impingement of neighboring crystals, is also reflected by the overall kinetics that differ from the classical sigmoidal curve that is found for homogeneous nucleation conditions. Figure 8 shows the kinetics of recrystallization (for the simulations with different threshold dislocation densities for spontaneous nucleation) (Figures 5–7). All curves reveal a flattened shape compared with the analytical model. The high offset value for the curve with 50% critical dislocation density is due to the small threshold value for a spontaneous initial cell flip. This means that 10% of all cells undergo initial site saturated nucleation. Figure 9 shows the corresponding Cahn-Hagel diagrams. It is found that the curves increasingly flatten and drop with an increasing threshold dislocation density for spontaneous recrystallization.

Interestingly, in all three simulation series where spontaneous nucleation took place in areas with large local dislocation densities, the kinetic instability criterion was usually also well enough fulfilled to enable further growth of these freshly recrystallized cells. In this context, it is notable that both instability criteria were treated entirely independently in this simulation. In other words, only those spontaneously recrystallized cells that subsequently found a misorientation above 15° to at least one non-recrystallized neighbor cell were able to expand further.

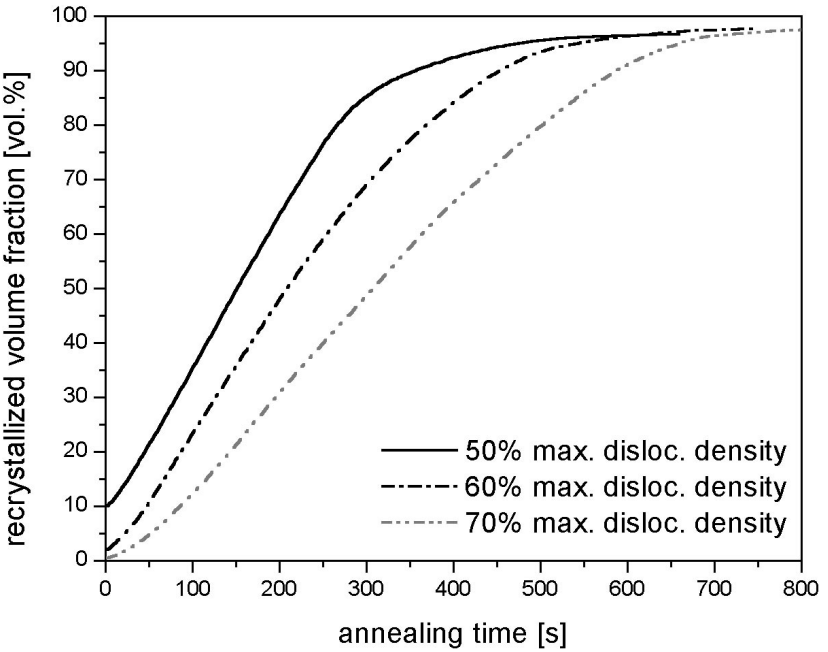

Figure 8 Kinetics of the recrystallization simulations shown in Figures 5–7. Annealing temperature, 800 K; scaling length $\lambda_m = 61.9\ \mu$m.

This makes the essential difference between a potential nucleus and a successful nucleus. Translating this observation into the initial deformation microstructure means that in the present example high dislocation densities and large local lattice curvatures typically occur in close neighborhood or even at the same sites.

Another essential observation is that the nucleation clusters are particularly concentrated in macroscopical deformation bands formed as diagonal instabilities through the sample thickness. Generic intrinsic nucleation inside heavily deformed grains, however, occurs rarely. Only the simulation with a very small threshold value of 50% of the maximum dislocation density as a precondition for a spontaneous energy drop shows some successful nucleation events outside the large bands. But even then, nucleation is successful only at former grain boundaries where orientation changes occur naturally. Summarizing this argument means that there might be a transition from extrinsic nucleation such as inside bands or related large-scale instabilities to intrinsic nucleation inside grains or close to existing grain boundaries. It is likely that both types of nucleation deserve separate attention. As far as the strong nucleation in macroscopic bands is concerned, future consideration should be placed on issues such as the influence of external friction conditions and sample geometry on nucleation. Both aspects strongly influence through thickness shear localization effects.

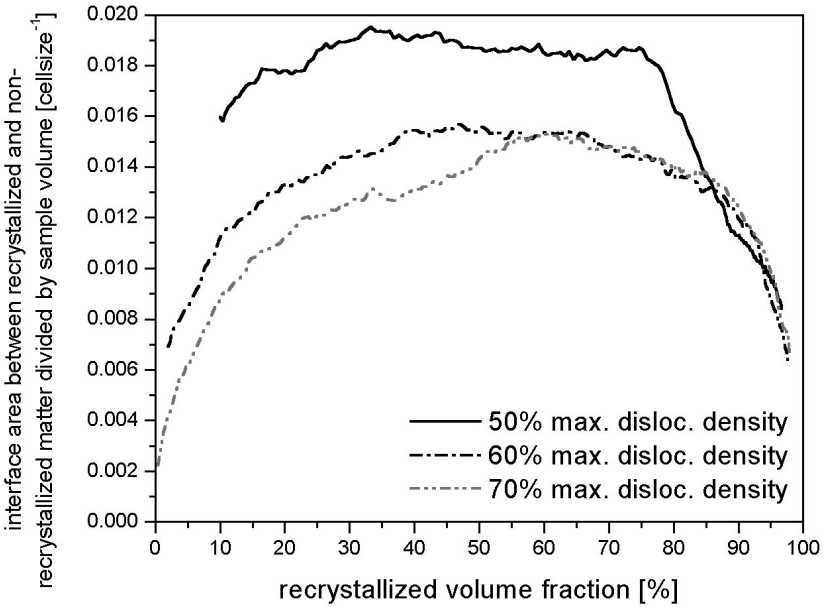

Figure 9 Simulated interface fractions between recrystallized and non-recrystallized material for the recrystallization simulations shown in Figures 5–7. Annealing temperature, 800 K; scaling length $\lambda_m = 61.9\ \mu$m.

Another result of relevance is the partial recovery of deformed material. Figures 5*d*, 6*d*, and 7*d* reveal small areas where moving large-angle grain boundaries did not entirely sweep the deformed material. An analysis of the state variable values at these coordinates and of the grain boundaries involved substantiates that insufficient misorientations, not insufficient driving forces, between the deformed and the recrystallized areas—entailing a drop in grain boundary mobility—were responsible for this effect. This mechanism is referred to as orientation pinning.

Simulation of Nucleation Topology Within a Single Grain

Recent efforts in simulating recrystallization phenomena on the basis of crystal plasticity finite element or electron microscopy input data are increasingly devoted to tackling the question of nucleation. Here it must be stated clearly that mesoscale cellular automata can neither directly map the physics of a nucleation event nor develop any novel theory for nucleation at the subgrain level. However, cellular automata can predict the topological evolution and competition among growing nuclei during the incipient stages of recrystallization. The initial nucleation criterion itself must be incorporated in a phenomenological form.

This section deals with such as an approach for investigating nucleation topology. The simulation was again started using a crystal plasticity finite element

approach. The crystal plasticity model set-up consisted in a single aluminum grain with face centered cubic crystal structure and 12 $\{111\}\langle 1\underline{1}0\rangle$ slip systems embedded in a plastic continuum, which had the elastic-plastic properties of an aluminum polycrystal with random texture. The crystallographic orientation of the aluminum grain in the center was $\varphi_1 = 32^\circ$, $\phi = 85^\circ$, $\varphi_2 = 85^\circ$. The entire aggregate was plane strain deformed to 50% thickness reduction (given as $\Delta d/d_0$, where d is the actual sample thickness and d_0 its initial thickness). The resulting data (dislocation density, orientation distribution) were then used as input data for the ensuing cellular automaton recrystallization simulation. The distribution of the dislocation density taken from all integration points of the finite element simulation is given in Figure 10.

Nucleation was initiated as outlined in detail above, i.e., each lattice point that had a dislocation density above some critical value (500×10^{13} m^{-2} in the present

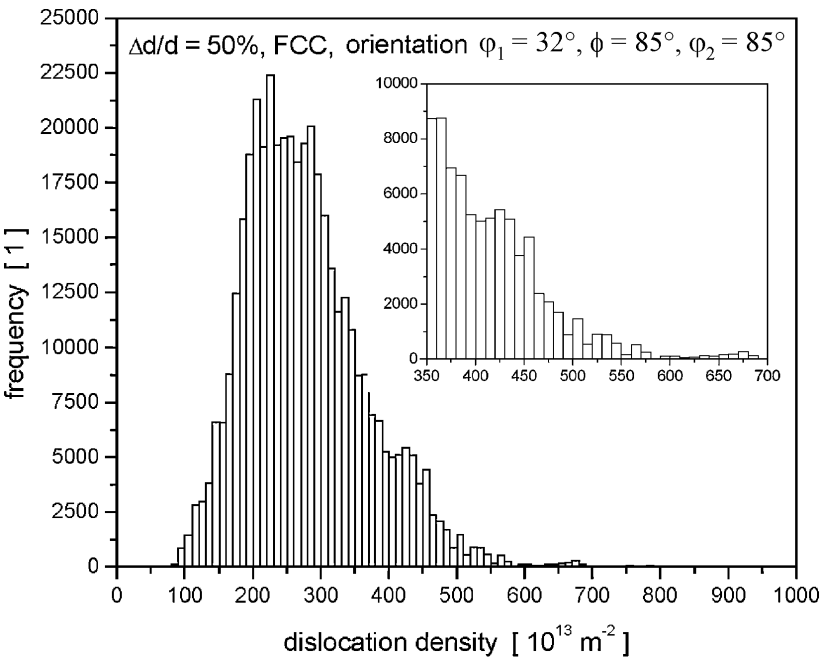

Figure 10 Distribution of the simulated dislocation density in a deformed aluminum grain embedded in a plastic aluminum continuum. The simulation was performed by using a crystal plasticity finite element approach. The set-up consisted of a single aluminum grain (orientation: $\varphi_1 = 32^\circ$, $\phi = 85^\circ$, $\varphi_2 = 85^\circ$ in Euler angles), with face centered cubic crystal structure and 12 $\{111\}\langle 1\underline{1}0\rangle$ slip systems, that was embedded in a plastic continuum, which had the elastic-plastic properties of an aluminum polycrystal with random texture. The sample was plane strain deformed to 50% thickness reduction. The resulting data (dislocation density, orientation distribution) were used as input data for a cellular automaton recrystallization simulation.

case; see Figure 10) of the maximum value in the sample was spontaneously recrystallized without orientation change. In the ensuing step, the growth algorithm was started according to Equations 1–11, i.e., a nucleus could only expand further if it was surrounded by lattice points of sufficient misorientation (above 15°). In order to concentrate on recrystallization in the center grain, the nuclei could not expand into the surrounding continuum material.

Figures 11*a–c* show the change in dislocation density during recrystallization (Figure 11*a*: 9% of the entire sample recrystallized, 32.1 s; Figure 11*b*: 19% of the entire sample recrystallized, 45.0 s; Figure 11*c*: 29.4% of the entire sample recrystallized, 56.3 s). The color scale marks the dislocation density of each lattice point in units of 10^{13} m^{-2}. The white areas are recrystallized. The surrounding blue area indicates the continuum material in which the grain is embedded (and into which recrystallization was not allowed to proceed). Figures 12*a–c* show the topology of the evolving nuclei without coloring the as-deformed volume. All recrystallized grains are colored to indicate their crystal orientation. The non-recrystallized material and the continuum surrounding the grain are colored white.

Figure 13 shows the volume fractions of the growing nuclei during recrystallization as a function of annealing time (800 K). The data reveal that two groups of nuclei occur: The first class of nuclei shows some growth in the beginning but no further expansion during the later stages of the anneal. The second class of nuclei

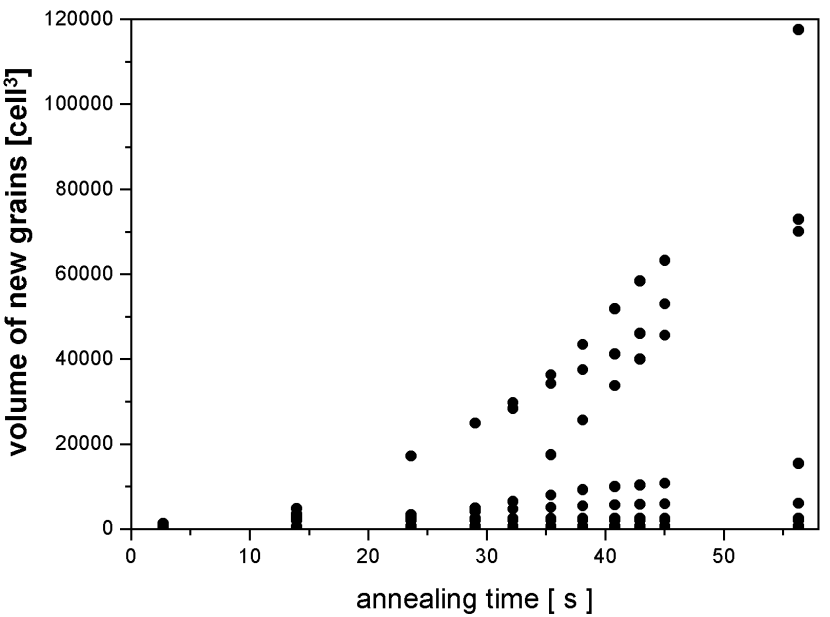

Figure 13 Volume fractions of the growing nuclei in Figure 11 during recrystallization as a function of annealing time (800 K).

shows strong and steady growth during the entire recrystallization time. The first group could be considered non-relevant nuclei, the second group could be termed relevant nuclei. The spread in the evolution of nucleation topology after their initial formation can be attributed to nucleation clustering, orientation pinning, growth selection, or driving force selection phenomena. Nucleation clustering means that areas with localization of strain and misorientation produce high local nucleation rates. This entails clusters of newly formed nuclei where competing crystals impinge on each other at an early stage of recrystallization so that only some of the newly formed grains of each cluster can expand further, which is another example of orientation pinning, as described above. In other words, some nuclei expand during growth into areas where the local misorientation drops below 15°. Growth selection is a phenomenon where some grains grow significantly faster than others due to a local advantage originating from higher grain boundary mobility such as shown in Figure 4*b*. Typical examples are the 40° ⟨111⟩ rotation relationship in aluminum or the 27° ⟨110⟩ rotation relationship in iron-silicon, both of which are known to have a growth advantage [e.g., (40)]. Driving force selection is a phenomenon where some grains grow significantly faster than others due to a local advantage in driving force (shear bands, microbands, heavily deformed grain).

CONCLUSIONS AND OUTLOOK

We have reviewed the fundamentals and some applications of cellular automata in the field of microstructure research, with special attention given to the fundamentals of mapping rate formulations for interfaces and driving forces on cellular grids. Some applications were discussed from the field of recrystallization theory.

The future of the cellular automaton method in the field of mesoscale materials science lies most likely in the discrete simulation of equilibrium and non-equilibrium phase transformation phenomena. The particular advantage of automata in this context is their versatility with respect to the constitutive ingredients, to the consideration of local effects, and to the modification of the grid structure and the interaction rules. In the field of phase transformation simulations, the constitutive ingredients are the thermodynamic input data and the kinetic coefficients. Both sets of input data are increasingly available from theory and experiment, rendering cellular automaton simulations more and more realistic. The second advantage, i.e., the incorporation of local effects will improve our understanding of cluster effects, such as those arising from the spatial competition of expanding neighboring spheres already in the incipient stages of transformations. The third advantage, i.e., the flexibility of automata with respect to the grid structure and the interaction rules, is probably the most important aspect for novel future applications. By introducing more global interaction rules (in addition to the local rules) and long-range or even statistical elements, in addition to the local rules for the state update, cellular automata could be established as a means for solving some of the intricate scale problems that are often encountered in the materials sciences. It is conceivable that for certain mesoscale problems, such as

the simulation of transformation phenomena in heterogeneneous materials in dimensions far beyond the grain scale, cellular automata can occupy a role between the discrete atomistic approaches and statistical Avrami-type approaches.

The major drawback of the cellular automaton method in the field of transformation simulations is the absence of solid approaches for the treatment of nucleation phenomena. Although basic assumptions about nucleation sites, rates, and textures can often be included on an empirical basis as a function of the local values of the state variables, intrinsic physically based phenomenological concepts such as those found, to a certain extent, in the Ginzburg-Landau framework (in case of the spinodal mechanism) are not available for automata. Hence, it might be advantageous in future work to combine Ginzburg-Landau-type phase field approaches with the cellular automaton method. For instance the (spinodal) nucleation phase could then be treated with a phase field method and the resulting microstructure could be further treated with a cellular automaton simulation.

The *Annual Review of Materials Research* is online at http://matsci.annualreviews.org

LITERATURE CITED

1. von Neumann J. 1963. In *Papers of John von Neumann on Computing and Computer Theory*, Vol. 12. Charles Babbage Inst. Reprint Ser. History of Computing, ed. W Aspray, A Burks. Cambridge, MA: MIT Press
2. Wolfram S, ed. 1986. *Theory and Applications of Cellular Automata, Advanced Series on Complex Systems, Selected Papers 1983–1986*, Vol. 1. Singapore: World Sci
3. Wolfram S. 1983. *Rev. Mod. Phys.* 55:601–22
4. Minsky M. 1967. *Computation: Finite and Infinite Machines*. Englewood Cliffs, NJ: Prentice-Hall
5. Conway JH. 1971. *Regular Algebra and Finite Machines*. London: Chapman & Hall
6. Raabe D. 1998. *Computational Materials Science*. Weinheim: Wiley
7. Hesselbarth HW, Göbel IR. 1991. *Acta Metall.* 39:2135–44
8. Pezzee CE, Dunand DC. 1994. *Acta Metall.* 42:1509–22
9. Sheldon RK, Dunand DC. 1996. *Acta Mater.* 44:4571–82
10. Davies CHJ. 1995. *Scripta Metall. Mater.* 33:1139–54
11. Marx V, Raabe D, Gottstein G. 1995. *Proc. 16th RISØ Int. Symp. Mater. Sci. Materials: Microstructural and Crystallographic Aspects of Recrystallization*, ed. N Hansen, D Juul Jensen, YL Liu, B Ralph, pp. 461–66. Roskilde, Denmark: RISO Natl. Lab
12. Marx V, Raabe D, Engler O, Gottstein G. 1997. *Textures Microstruct.* 28:211–18
13. Marx V, Reher FR, Gottstein G. 1998. *Acta Mater.* 47:1219–30
14. Davies CHJ. 1997. *Scripta Mater.* 36:35–46
15. Davies CHJ, Hong L. 1999. *Scripta Mater.* 40:1145–52
16. Raabe D. 1999. *Philos. Mag. A* 79:2339–58
17. Raabe D, Becker R. 2000. *Modelling Simulation Mater. Sci. Eng.* 8:445–62
18. Raabe D. 2000. *Comput. Mater. Sci.* 19:13–26
19. Raabe D, Roters F, Marx V. 1996. *Textures Microstruct.* 26–27:611–35
20. Cortie MB. 1993. *Metall. Trans. B* 24: 1045–52

21. Brown SGR, Williams T, Spittle JA. 1994. *Acta Metall.* 42:2893–906
22. Gandin CA, Rappaz M. 1997. *Acta Metall.* 45:2187–98
23. Gandin CA. 2001. *Adv. Eng. Mater.* 3:303–6
24. Gandin CA, Desbiolles JL, Thevoz PA. 1999. *Metall. Mater. Trans. A* 30:3153–72
25. Spittle JA, Brown SGR. 1995. *J. Mater. Sci.* 30:3989–402
26. Brown SGR, Clarke GP, Brooks AJ. 1995. *Mater. Sci. Technol.* 11:370–82
27. Spittle JA, Brown SGR. 1994. *Acta Metall.* 42:1811–20
28. Kumar M, Sasikumar R, Nair P, Kesavan R. 1998. *Acta Mater.* 46:6291–304
29. Brown SGR. 1998. *J. Mater. Sci.* 33:4769–82
30. Yanagita T. 1999. *Phys. Rev. Lett.* 1999: 3488–92
31. Koltsova EM, Nenaglyadkin IS, Kolosov AY, Dovi VA. 2000. *Russ. J. Phys. Chem.* 74:85–91
32. Geiger J, Roosz A, Barkoczy P. 2001. *Acta Mater.* 49:623–29
33. Liu Y, Baudin T, Penelle R. 1996. *Scripta Mater.* 34:1679–86
34. Karapiperis T. 1995. *J. Stat. Phys.* 81:165–74
35. Young MJ, Davies CHJ. 1999. *Scripta Mater.* 41:697–708
36. Kortluke O. 1998. *J. Phys. A* 31:9185–98
37. Gottstein G, Shvindlerman LS. 1999. *Grain Boundary Migration in Metals—Thermodynamics, Kinetics, Applications*. Boca Raton, FL: CRC
38. Becker RC. 1991. *Acta Metall. Mater.* 39: 1211–30
39. Becker RC, Panchanadeeswaran S. 1995. *Acta Metall. Mater.* 43:2701–19
40. Humphreys FJ, Hatherly M. 1995. *Recrystallization and Related Annealing Phenomena*. New York: Pergamon

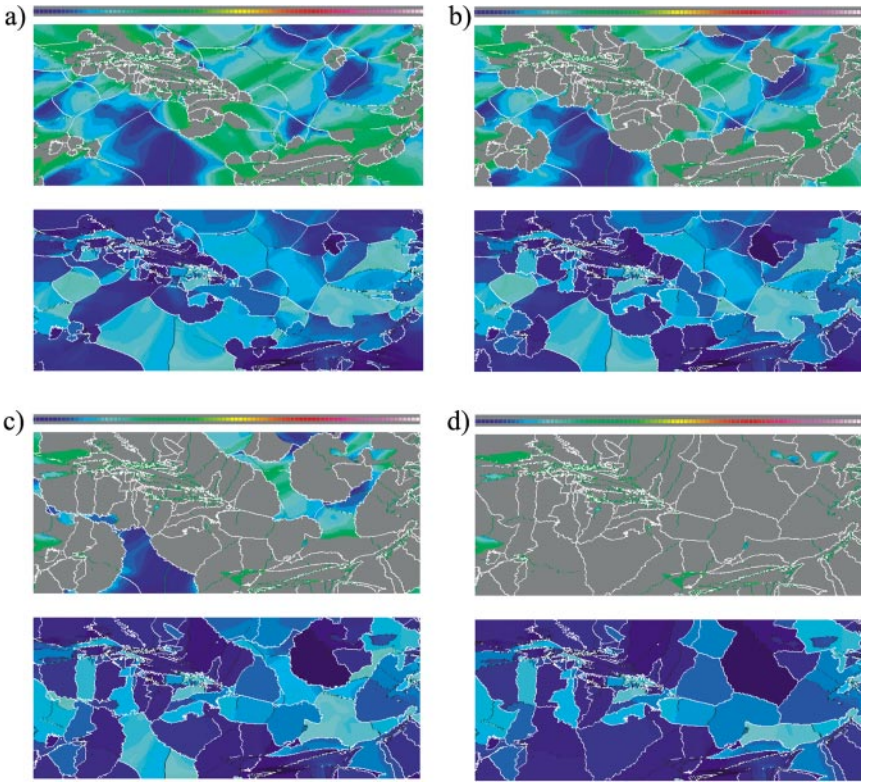

Figure 5 Consecutive stages of a two-dimensional simulation of primary static recrystallization in a deformed aluminum polycrystal on the basis of crystal plasticity finite element starting data. The figure shows the change in dislocation density (*top*) and microtexture (*bottom*) as a function of the annealing time during isothermal recrystallization. The texture is given in terms of the magnitude of the Rodriguez orientation vector using the cube component as reference. The *gray areas* in the upper figures indicate a stored dislocation density of zero, i.e., these areas are recrystallized. The *heavy white lines* indicate grain boundaries with misorientations above 15° irrespective of the rotation axis. The *thin green lines* indicate misorientations between 5° and 15° irrespective of the rotation axis. The simulation parameters: 800 K; thermodynamic instability criterion, site-saturated spontaneous nucleation in cells with at least 50% of the maximum occurring dislocation density (threshold value); kinetic instability criterion for further growth of such spontaneous nuclei, misorientation above 15°; activation energy of the grain boundary mobility, 1.46 eV; pre-exponential factor of the grain boundary mobility, $m_0 = 8.3 \times 10^{-3}$ m^3/(N s; mesh size of the cellular automaton grid (scaling length), $\lambda_m = 61.9$ μm.

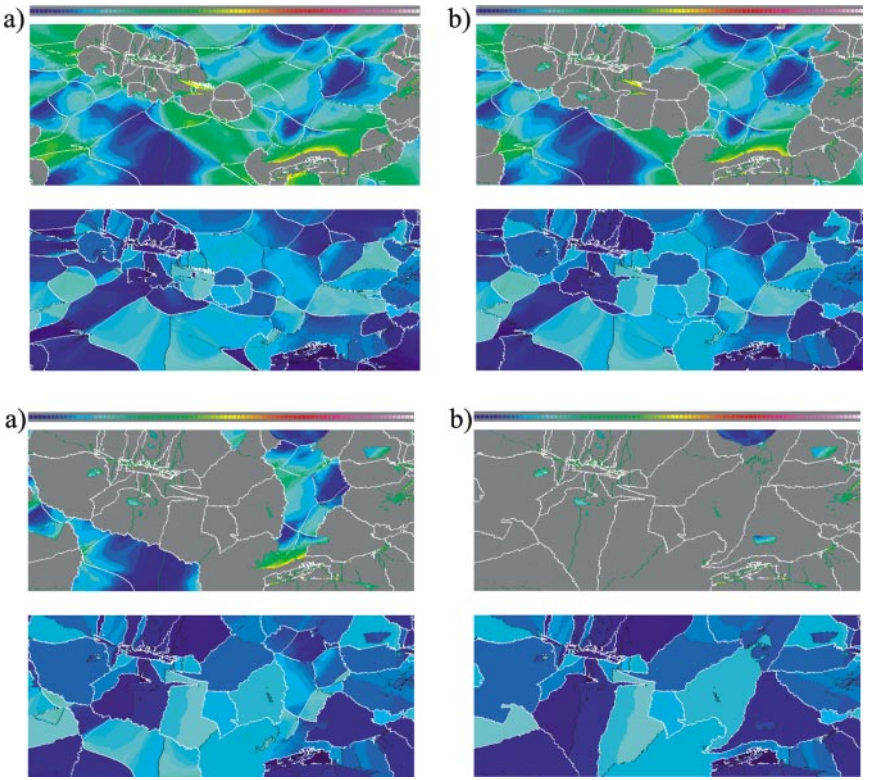

Figure 6 Parameters such as in Figure 5, but site-saturated spontaneous nucleation occurred in all cells with at least 60% of the maximum occurring dislocation density.

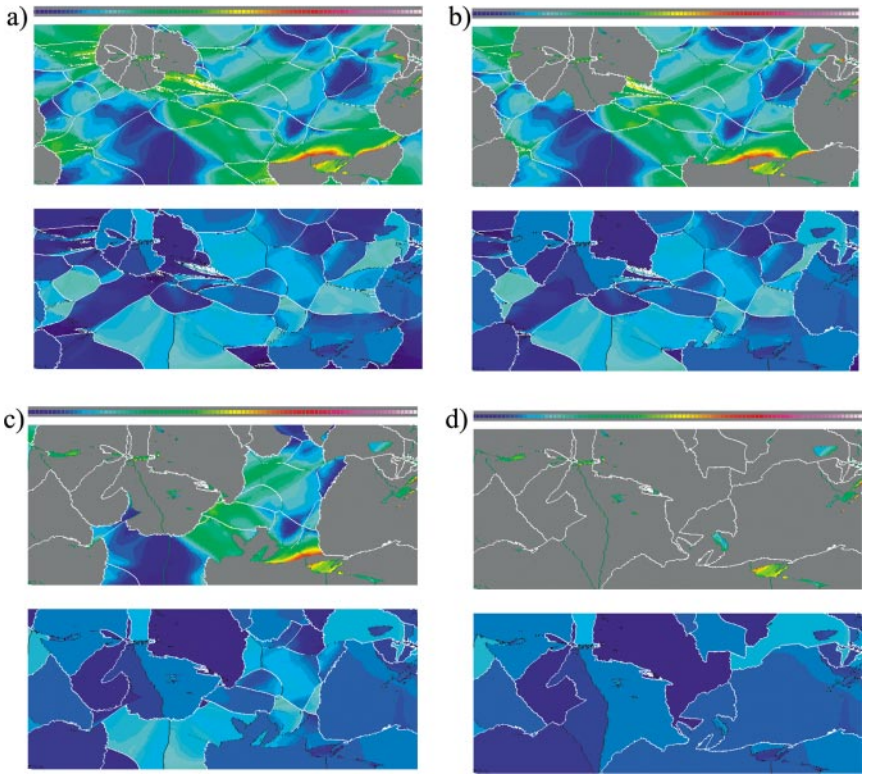

Figure 7 Parameters such as in Figure 5, but site-saturated spontaneous nucleation occurred in all cells with at least 70% of the maximum occurring dislocation density.

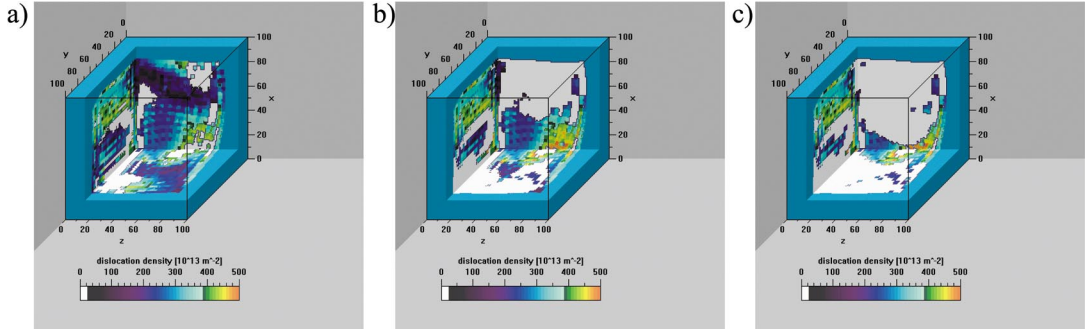

Figure 11 Change in dislocation density during recrystallization (800 K). The color scale indicates the dislocation density of each lattice point in units of 10^{13} m^{-2}. The *white areas* are recrystallized. The surrounding *blue area* indicates the continuum material in which the grain is embedded. (*a*) 9% of the entire sample recrystallized, 32.1 s; (*b*) 19% of the entire sample recrystallized, 45.0 s; (*c*) 29.4% of the entire sample recrystallized, 56.3 s.

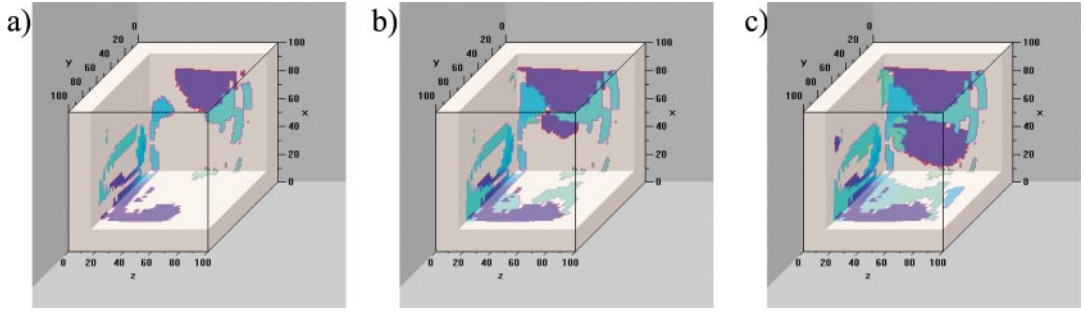

Figure 12 Topology of the evolving nuclei of the microstructure given in Figure 11 without coloring the as-deformed volume. All newly recrystallized grains are colored indicating their crystal orientation. The non-recrystallized material and the continuum surrounding the grain are *white*. Sample recrystallization percents same as in Figure 11.